

國立交通大學
電信工程學系碩士班
碩士論文

室內超寬頻無線電通道頻寬效應之研究



**Effect of Bandwidth on Indoor
UWB Radio Channels**

研究生：沈鳴君
指導教授：唐震寰 博士

室內超寬頻無線電通道頻寬效應之研究

Effect of Bandwidth on Indoor UWB Radio Channels

研究生：沈鳴君

Student : Ming-Jiun Shen

指導教授：唐震寰

Advisor : Dr. Jenn-Hwan Tarng

國立交通大學

電信工程學系碩士班



Submitted to Department of Communication Engineering
College of Electrical and Computer Engineering
National Chiao Tung University
in Partial Fulfillment of the Requirements
for the Degree of
Master of Science
in
Communication Engineering
July 2004
Hsinchu, Taiwan, Republic of China

中華民國九十三年七月

室內超寬頻無線電通道頻寬效應之研究

研究生：沈鳴君

指導教授：唐震寰博士

國立交通大學 電信工程研究所

摘要

本論文主要是研究室內環境超寬頻無線電傳播之頻寬效應，在此論文中，吾人是以隨機節拍-延遲-線模型，描述室內超寬頻通道的特性，在此模型是以兩種參數：功率比值 r 以及衰減常數 ε 來描述平均功率延遲曲線圖，而這些參數可經由在大樓內進行大量的量測之後計算得到，而所量測頻段為 3 GHz 至 5 GHz。由計算結果發現以下之現象：(1) 衰減常數僅稍微與訊號頻寬有關；(2) 功率比值會隨著頻寬增加而變小；(3) 衰減常數會隨著區域散射體愈靠近接收端而變小；(4) 功率比值會隨著區域散射體愈靠近接收端而變大；(5) 在視線內環境，Rician 因子會隨著頻寬增加而變小；(6) 在非視線內環境，Rician 因子會隨著頻寬增加而變大。

Effect of Bandwidth on Indoor UWB Radio Channels

Student : Ming-Jiun Shen

Advisor : Dr. Jenn-Hwan Tarn

Department of Communication Engineering and Institute of
Communication National Chiao Tung University

Abstract

Effects of bandwidth on Ultra-Wideband (UWB) radio propagation in indoor environments are investigated. To characterize the indoor UWB channels, the stochastic tapped-delay-line (STDL) model is employed. With the STDL model, the power delay profile (PDP) can be described by using power ratio r and decay constant ϵ as described. Those parameters can be calculated with a large number of measurement data carried out at an education building. The measured frequencies are ranged from 3 GHz to 5GHz. It is found that (1) The decay constant of the PDP is only slightly dependent on the signal bandwidth; (2) The power ratio of the PDP is decreased when the signal bandwidth is increased; (3) The decay constant is decreased as the local scatterers move closer to receiver; (4) The power ratio is increased as the local scatterers move closer to receiver; (5) The Rician factor is decreased when radio bandwidth is increased of LOS condition; (6) The Rician factor is increased when radio bandwidth is increased of NLOS condition.

誌謝

首先，我要對我的指導教授唐震寰老師致上最誠摯的感謝，感謝老師在我碩士兩年的研究生涯中，給于我最細心與凡心的指導與叮嚀，並帶領我一窺無線通訊領域研究的奧妙。

其次，對於波散射與傳播實驗室的學長與同學們也要致上我深深的謝意，他們所給予我在知識上和精神上的啟示與鼓勵以及在實驗量測中的協助，對完成本篇論文有莫大的助益。

最後，要感謝的是我的家人，由於他們給予我的支持與關懷，使我在人生的過程裡得到最細心的呵護與照顧，讓我在成長與求學的過程中能夠有所依靠。

僅以此篇論文獻給所有關心我的人。



沈鳴君

國立交通大學，新竹市

中華民國九十三年七月

Contents

Contents	VI
Figure Captions	VII
Table Captions	XI
Chapter 1 Introduction	1
Chapter 2 UWB Propagation Characteristic and Modeling	4
2.1 UWB Basic Characteristics	5
2.2 UWB Multipath Model Comparison	9
2.2.1 Stochastic Tapped Delay Line Model (STDLD)	9
2.2.2 Saleh-Valenzuela Model (S-V)	10
2.2.3 Turin's Δ -K Model	12
2.3 Received Envelope Distribution	15
2.3.1 Rayleigh Fading	15
2.3.2 Rician Fading	15
2.3.3 Nakagami Fading	16
Chapter 3 Measurement System and Environment	17
3.1 Measurement System and Setup	18
3.2 Measurement Environment Description	24
3.3 Measurement Result	32
Chapter 4 Effects of Signal Bandwidth and Propagation on UWB Channels	34
4.1 Effect of Bandwidth and Propagation on Instantaneous Power Delay Profile	34
4.2 Effect of Bandwidth and Propagation on Averaged Power Delay Profile (Not including local scattering effects)	58
4.3 Effect of Signal Bandwidth on Amplitude fading	65
Chapter 5 Conclusion	73
Reference	74

Figure Captions

Figure 2-1	Transmitting energy versus radio signals.....	6
Figure 2-2	Power delay profiles of ultra wideband and narrowband communications. UWB systems have very high resolution.	6
Figure 2-2	The average power delay profile versus the excess delay.....	10
Figure 2-3	An illustration of channel impulse response.	12
Figure 2-4	An illustration of exponential decay of mean cluster power and ray power within clusters.	12
Figure 2-5.	Illustration of the Δ - K process.	13
Fig. 3-2	A photo of the frequency domain channel sounding system.....	21
Fig. 3-3	A photo of the wideband antenna.	21
Figure 3-4	(a) Vertical and (b) Horizontal pattern of the transmitted and received antennas.	23
Fig. 3-5	(a) Small-scale variation square grid; (b) The variation of Rician factor for different square grid.	25
Figure 3-6	9 th floor layout of the 4 th Engineering Building. (a) There are 5 measured points in Room 901; (b) There are 6 measured points in Room 911A.	26
Figure 3-6	2 nd floor layout of the 4 th Engineering Building. (c) There are 5 measured points in Room 203; (d) There are 4 measured points in Room 215.	27
Figure 3-6	(e) 3 rd floor layout of the 4 th Engineering Building.	28
Figure 3-6	(f) 7 th floor layout of the 4 th Engineering Building.	29
Figure 3-7	Power delay profiles measured at 64 locations separated by $\lambda/2$ on indoor. (a)The measured PDP at no.1 of LOS situation; (b) The measured PDP at no.2 of NLOS situatio.	33
Figure 4-1	The normalized instantaneous PDP of subpoint no.110 in Room 901 for different bandwidth. (a) The bandwidth is 2 GHz with power ratio $r=0.016$, decay constant $\varepsilon =14.73$ (ns); (b) The bandwidth is 1.5 GHz with $r=0.019$, $\varepsilon=16.09$ (ns); (c) The bandwidth is 1 GHz with $r=0.029$, $\varepsilon=15.49$ (ns); (d) The bandwidth is 500 MHz with $r=0.041$, $\varepsilon=17.33$ (ns).....	39
Figure 4-2	The normalized instantaneous PDP of subpoint no.124 in Room 901 for different bandwidth. (a) The bandwidth is 2 GHz with $r=0.016$, $\varepsilon=14.75$ (ns); (b) The bandwidth is 1.5 GHz with $r=0.019$, $\varepsilon=17.62$ (ns); (c) The bandwidth is 1 GHz with $r=0.021$, $\varepsilon=15.97$ (ns); (d) The bandwidth is 500 MHz with	

$r=0.031, \epsilon=19.74(\text{ns})$	41
Figure 4-3 The normalized instantaneous PDP of subpoint no.2430 in Room 303 for different bandwidth. (a) The bandwidth is 2 GHz with $r=0.17, \epsilon=23.94(\text{ns})$; (b) The bandwidth is 1.5 GHz with $r=0.173, \epsilon=25.7(\text{ns})$; (c) The bandwidth is 1 GHz with $r=0.172, \epsilon=25.33(\text{ns})$; (d) The bandwidth is 500 MHz with $r=0.263, \epsilon=21.58(\text{ns})$	43
Figure 4-4 The normalized instantaneous PDP of subpoint no.2450 in Room 303 for different bandwidth. (a) The bandwidth is 2 GHz with $r=0.101, \epsilon=28.82(\text{ns})$; (b) The bandwidth is 1.5 GHz with $r=0.101, \epsilon=28.61(\text{ns})$; (c) The bandwidth is 1 GHz with $r=0.101, \epsilon=26.76(\text{ns})$; (d) The bandwidth is 500 MHz with $r=0.185, \epsilon=22.82(\text{ns})$	45
Figure 4-5 The histogram of the power ratio (in dB scale) can be fitted well by a normal distribution. (a) The bandwidth is 2 GHz with $\mu_r = -16.44$ dB and $\sigma_r = 1.55$ dB; (b) The bandwidth is 1 GHz with $\mu_r = -13.66$ dB and $\sigma_r = 1.78$ dB; (c) The bandwidth is 500 MHz with $\mu_r = -11.6$ dB and $\sigma_r = 2.13$ dB.....	47
Figure 4-6 The histogram of the logarithmic decay constant can be fitted well by a normal distribution. (a) The bandwidth is 2 GHz with $\mu_\epsilon = 11.48$ dB and $\sigma_\epsilon = 0.19$ dB; (b) The bandwidth is 1 GHz with $\mu_\epsilon = 11.58$ dB and $\sigma_\epsilon = 0.31$ dB; (c) The bandwidth is 500 MHz with $\mu_\epsilon = 11.87$ dB and $\sigma_\epsilon = 0.52$ dB.....	48
Figure 4-7. Power ratio r versus signal bandwidth at different measurement subpoints for the LOS 0-4m situation.....	49
Figure 4-8. Decay constant ϵ versus signal bandwidth at different measurement subpoints for the LOS 0-4m situation.....	49
Figure 4-9. Power ratio r versus signal bandwidth at different measurement subpoints for the LOS 4-10m situation.....	50
Figure 4-10. Decay constant ϵ versus signal bandwidth at different measurement subpoints for the LOS 4-10m situation.....	50
Figure 4-11. Power ratio r versus signal bandwidth at different measurement subpoints for the NLOS 0-4m situation.....	51
Figure 4-12. Decay constant ϵ versus signal bandwidth at different measurement subpoints for the NLOS 0-4m situation.....	51
Figure 4-13. Power ratio r versus signal bandwidth at different measurement subpoints for the NLOS 4-20m situation.....	52
Figure 4-14. Decay constant ϵ versus signal bandwidth at different	

measurement subpoints for the NLOS 4-20m situation.....	52
Figure 4-15 (a) There are near local scatterers distribution around the receiver within a radius of 20cm in a laboratory. (b) There is slightly far local scatterers distribution around the receiver within a radius of 45cm in the laboratory.	53
Figure 4-16 The effect multipath number versus the delay bin for different local scatterer distribution around the receiver. (a) There is no local scatterer distribution around the receiver; (b) There is farer scatterer distribution around the receiver; (c) There is nearer scatterer distribution around the receiver.	54
Figure 4-17 The power ratio histograms of different local scatterers distribution around the receiver conditions. (a) $\mu_r = -19.84$ and $\sigma_r = 1.57$ of no local scatterers situation; (b) $\mu_r = -18.92$ and $\sigma_r = 1.414$ of farer local scatterers situation; (c) $\mu_r = -18.15$ and $\sigma_r = 1.6$ of nearer local scatterer situation.	56
Figure 4-18 The decay constant histograms of different local scatterers distribution around the receiver conditions. (a) $\mu_\epsilon = 11.33$ and $\sigma_\epsilon = 0.2$ of no local scatterer situation; (b) $\mu_\epsilon = 11.11$ and $\sigma_\epsilon = 0.18$ of farer local scatterers situation; (c) $\mu_\epsilon = 11.09$ and $\sigma_\epsilon = 0.19$ of nearer local scatterers situation.....	57
Figure 4-19 The normalized average PDP of point no.24 in Room 302 for different bandwidth. (a) The bandwidth is 2 GHz with $r=0.165, \epsilon=26.38(\text{ns})$; (b) The bandwidth is 500 MHz with $r=0.292, \epsilon=25.7(\text{ns})$	60
Figure 4-20 The normalized average PDP of point no.15 in Room 203 for different bandwidth. (a) The bandwidth is 2 GHz with $r=0.012, \epsilon=19.4(\text{ns})$; (b) The bandwidth is 500 MHz with $r=0.068, \epsilon=17(\text{ns})$	61
Figure 4-21 The power ratio versus the distance between Tx and Rx.....	62
Figure 4-22 The decay constant versus the distance between Tx and Rx....	62
Figure 4-23 The histogram of the power ratio (in dB scale) can be fitted well by a normal distribution with $\mu_r = -13.81$ dB and $\sigma_r = 4.25$ dB.....	63
Figure 4-24 The histogram of the logarithmic decay constant can be fitted well by a normal distribution with $\mu_\epsilon = 12.07$ dB and $\sigma_\epsilon = 1.45$ dB. .	63
Figure 4-25. Power ratio r versus signal bandwidth at different measurement points for the LOS 0-4m situation.	64
Figure 4-26. Decay constant ϵ versus signal bandwidth at different measurement points for the LOS 0-4m situation.	64

Figure 4-27(a) PDF of measured and fitted signal amplitudes of the 38 th bin in Room 303 for NLOS environment. The bandwidth is 2GHz.	67
Figure 4-27(b) PDF of measured and fitted signal amplitudes of the 65 th bin in Room 303 for NLOS environment. The bandwidth is 2GHz.	67
Figure 4-28(a) PDF of measured and computed signal amplitudes of the first bin at point no.2 follows a Rician distribution with $K= 8.7$	68
Figure 4-28(b) PDF of measured and calculated signal amplitudes of the first bin at point no.16 follows a Rician distribution with $K=26.4$	68
Figure 4-28(c) PDF of measured and computed signal amplitudes of the first bin at point no.21 follows a Rician distribution with $K=16.4$	69
Figure 4-28(d) PDF of measured and computed signal amplitudes of the first bin at point no.41 follows a Rician distribution with $K= 17.2$	69
Figure 4-29 Rician factor K versus signal bandwidth at different measurement points of the LOS 0-4m situation.	70
Figure 4-30 Rician factor K versus signal bandwidth at different measurement points of the NLOS 0-4m situation.....	70
Figure 4-31 Rician factor K versus signal bandwidth at different measurement points of the LOS 4-10m situation.	71
Figure 4-32 Rician factor K versus signal bandwidth at different measurement points of the NLOS 4-20m situation.....	71
Figure 4-33 The Rician factor versus the distance between Tx and Rx.	72

Table Captions

Table 1-1 Several result on UWB channel model have been explored.....	3
Table 2-1 UWB compared to existing data communications standards.	8
Table 3-1 The main parameters in the measurement.	20
Table 3-2 The different channel scenarios.....	30



Chapter 1

Introduction

In recent years, ultra-wideband (UWB) communications has received great interest from both the research community and industry. The potential strength of the UWB radio technique lies in its use of extremely wide transmission bandwidths, which results in desirable capabilities including accurate position location and ranging, lack of significant fading, high multiple access capability, covert communications, and possible easier material penetration. UWB is an old technology with a new lease on life. Long used by the U.S. military, In February 2001, the American Federal Communications Commission (FCC) issued a report and order that allows the transmission of UWB signals if certain power restrictions are fulfilled.

Wireless communication plays an important role in our daily life. With lower price and more applications, wireless communication is getting popularized. Folks can easily afford to build a local-area network (LAN) at home and use the mobile computing devices without any cable limits. In the future, people will be eager to retire the miscellaneous cables and wires, and use wireless technologies to enjoy their home electric appliances.

Accurate performance prediction of such systems in a realistic environment necessitates the knowledge of UWB multipath channel characteristics, especially the statistical distribution of small-scale fluctuations. It is because that channel capacity is a function of the signal to interference ratio [1].

Currently, IEEE 802.15 study group SG3a is developing a high rate physical (PHY) for wireless personal area network (WPAN). UWB may be selected for this PHY due to its unique suitability for this application. For the varied WPAN

applications, different radio bandwidth is needed to meet the data rate and quality of service requirements [2]. According to the FCC regulations of UWB radio technology and systems [3], the radio bandwidth that affects the resolvable multipath number may vary in a wide range from several hundred MHz to a few GHz. Several contributions on UWB channel model have been showed in Table 1-1.

However, few researches focused on the studies of the effect of radio bandwidth on propagation channel model so far. In this article, the stochastic tapped-delay-line (STDL) model is used, which describes the indoor UWB channels with the parameters such as delay constant and power ratio of the averaged power-delay profile (PDP). The effect of radio bandwidth on these two parameters is analyzed by measurement results. The amplitude distribution of small-scale fading was estimated the effect of radio bandwidth on the multipath phenomenon.

This article is organized as follows. In chapter 2, we will describe radio propagation characteristics and some popular indoor channel models for UWB channel. In the same chapter, several amplitude statistics of small-scale fading will be discussed. In chapter 3, is the UWB channels measurement. We will describe the measurement system and environment. In chapter 4, from our measurement and analysis results, the Rican factor and those parameters of STDL model will be calculated. The effect of radio bandwidth on small scale fading and those parameters will be analyzed. A brief conclusion is provided in Chapter 5.

Ref. No.	Measurement Environment	Measurement Result
[6]	In an office building	The PDP can be modeled by a single exponential decay. The energy statistics follows a Gamma distribution The fading of each bin is uncorrelated
[14]	In a home environment	The S-V model and lognormal amplitude distribution can fit the PDP of the measurement data
[15]	In an office/laboratory building	S-V model which demonstrated the clustering phenomenon

Table 1-1 Several result on UWB channel model have been explored



Chapter 2

UWB Propagation Characteristic and Modeling

Wireless propagation channels have been investigated for more than 50 years, and a large number of channel models are available in the literature. The signal that has propagated through a wireless channel consists of multiple replicas (echoes) of the originally transmitted signal; this phenomenon is known as multipath propagation. The different multipath components (MPCs) are characterized by different delays and attenuations. Thus, at the receiver, all the MPCs can interfere (constructively or destructively). If there is a large number of MPCs, the complex amplitude has a complex Gaussian distribution, which results in a Rayleigh or Rician distribution of the amplitudes.

UWB systems have very large bandwidth. Thus, the different delays of the multipath components influence the system performance, and have to be modeled. The power delay profile of the channel describes how much power arrives within a certain delay interval. For system analysis, the delay axis is typically divided into bins whose size is comparable to the inverse of the system bandwidth. If enough MPCs fall within such a delay bin, there is still interference between the MPCs, and the amplitude statistics within each delay bin is Rayleigh or Rice. However, UWB systems have very high resolution in the time domain and only a small number of multipath components fall into each bin of the delay profile, the small scale distributions of the path gains may not follow the traditional amplitude statistics. In this chapter we will describe UWB characteristics and three indoor channel models. At last, we will describe several amplitude statistics of small-scale fading.

2.1 UWB Basic Characteristics

The FCC has defined that UWB transmissions fall within the frequencies of 3.1 to 10.6 GHz, with a minimum spectral width of 500 MHz, or 25 percent of the center frequency (3.5 to 4.5 GHz for a center frequency of 4 GHz). By dividing the power of the signal across a range of frequencies, the affect upon any frequency is below the acceptable noise floor for unintentional emitters that FCC Part 15 rules define. Table 2-1 showed the UWB compared to existing data communications standards.

An UWB signal is generally defined to be a radio signal with fractional bandwidth greater than 0.25 or bandwidth more than 500MHz, where fractional bandwidth (FBW) is defined as

$$FBW=2*(f_H-f_L)/(f_H+f_L) \quad (2.1)$$

where f_H is the upper frequency of the -10 dB emission point and f_L is the lower frequency of the -10 dB emission point. The center frequency of the transmission was defined as the average of the upper and lower -10 dB points, i.e., $(f_H + f_L)/2$. The Commission proposed to base its modified definition of an UWB device on -10 dB bandwidth, rather than the -20 dB bandwidth, because under the Part 15 limits, UWB devices operate so close to the noise floor that in many cases it may not be possible to measure the -20 dB bandwidth.

UWB systems can use very low transmit power without interfering with existing communication systems. However, lower power levels typically limits the signals to shorter ranges. Narrowband communications pack transmitting energy into a small fractional bandwidth. Ultra wideband communications spread transmitting energy across a wide spectrum frequency, such that the energy in any frequency band is below the noise flow. This is illustrated in Figure 2-1 below.

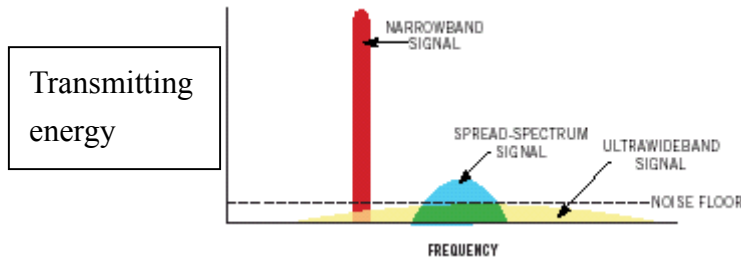


Figure 2-1 Transmitting energy versus radio signals.

Within the power limit allowed under current FCC regulations, UWB can carry huge amounts of data over a short distance at very low power, while also having the ability to carry signals through doors and other obstacles that tend to reflect signals at more limited bandwidths and a higher power. At higher power levels, UWB signals can travel to significantly greater ranges.

The ultra-short signal in UWB systems creates dramatic gains in path resolution when compared to narrowband and wideband communication systems. For UWB signals with GHz bandwidths, the multipath resolution is on the order of a nanosecond or less, i.e., down to path length differentials on the order of 0.3m or less. The higher path resolution of UWB systems leads to a smaller number of paths in each bin than that of narrowband or wideband systems. This is illustrated in Figure 2-2 below.

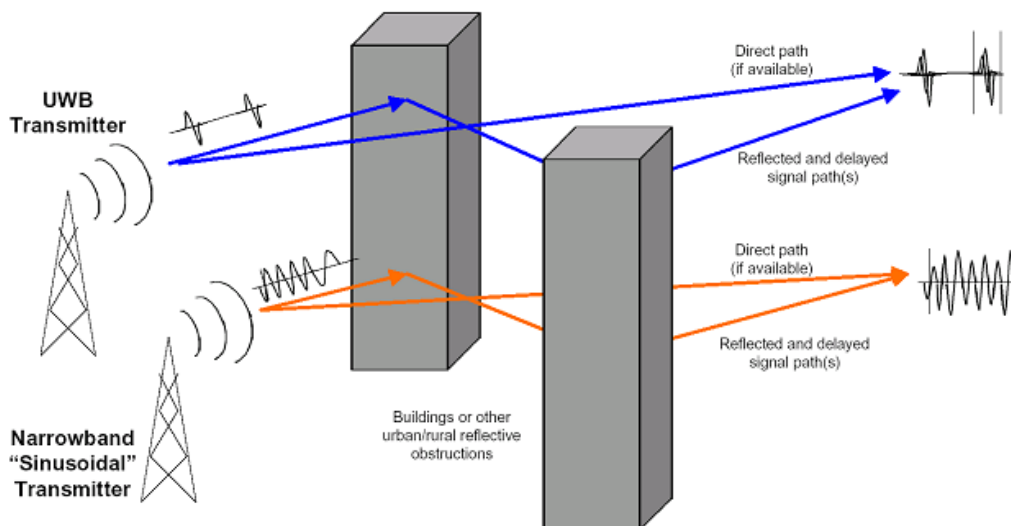


Figure 2-2 Power delay profiles of ultra wideband and narrowband communications. UWB systems have very high resolution.

The potential strength of the UWB-radio technique lies in its use of extremely wide

transmission bandwidths, resulting in the following desirable capabilities including:

- Accurate position location and ranging, and lack of significant multipath fading due to fine delay resolution.
- Multiple access due to wide transmission bandwidth.
- Covert communications due to low transmission power operation.



	Zigbee	Bluetooth	802.15.3	UWB	802.11b	802.11a	802.11g
IEEE Task Group	802.15.4	802.15.1	802.15.3	802.15.3a	802.11b	802.11a	802.11g
Frequency band	2.4GHz 900Mhz	2.4 GHz	2.4GHz	3.1-10.6GHz	2.4 GHz	5 GHz	2.4 GHz
Data rate	40 to 240 Kbps	Up to 1 Mbit/s	Up to 55 Mbit/s	>100 Mbit/s	Up to 22 Mbit/s	Up to 54 Mbit/s	> 22 Mbit/s
Range	20 meters	10-20 meters	Up to 10 meters	10-30 meters	100 meters	100 meters	100 meters
QoS/MAC	In progress	No video support. Peer-to-peer and ad hoc netwrkg.	Guaranteed time slots. Ad hoc netwrkg. Power mgmnt.	TBD Guaranteed time slots for video, ad hoc netwrkg. Will use 802.15.3 MAC.	Non-guaranteed QoS, no video support, no ad hoc netwrkg—New MAC standards such as 802.11d and .11h expect to include video and multimedia support.		
PHY	DSSS-- BPSK O-QPSK	FSK	QPSK 16.32.64 QAM	Multi-band OFDM	CCK	OFDM	8-PSK or OFDM and CCK
Spatial Capacity/m²	Unknown	30 kbps	Unknown	>1000 kbps	1 kbps	55-83 kbps	

Table 2-1 UWB compared to existing data communications standards.

Legend:

CC = Complementary Code Keying

OFDM= Orthogonal Frequency Division Multiplexing

QAM= Quadrature Amplitude Modulation

QPSK= Quadrature PSK

FSK= Frequency Shift Keying

PSK= Phase Key Shifting

2.2 UWB Multipath Model Comparison

Although UWB systems can be described by frequency-domain or time-domain models, our work focus on evaluating discrete time models. This model is based upon the following channel impulse response model [19]:

$$h(t) = \sum_{l=0}^{L-1} \alpha_l \delta(t - \tau_l) \quad (2.2)$$

where α_l is the amplitude fading factor on path l (could be complex), τ_l is the random delay of path l , L is the number of multipath components, and $\delta(t)$ is the Dirac delta function.

In practice, the rays of the received signal arrive in clusters. The formation of the clusters is related to the building superstructure (e.g., large metalized external or internal walls and doors). The rays within a cluster are formed by multiple reflections from objects in the vicinities of the transmitter and the receiver (e.g., room walls, furnishings, and people). There are three main indoor channel models can demonstrated the realistic multipath phenomenon :the tap-delay line model[20], the Saleh-Valenzuela (S-V) model [4], and the Δ -K model described in [5], as well as several novel modifications to these approaches that better matched the measurement characteristics. The following sections describe different multipath channel models.

2.2.1 Stochastic Tapped Delay Line Model (STDL)

The STDL model characterizes the shape of the PDP of the UWB indoor channel in terms of path power and delays of a subsequent discrete taps with equal time spacing, i.e., by the pairs $\{P_k, \tau_k\}$ with $\tau_k = (k-1)\Delta$, where Δ is the tap spacing which is inversely proportional to the radio bandwidth of the considered system. Therefore, the power of each tap, P_k , results from the square of the sum of the complex fields of multipath components (MPCs) arriving within $\Delta\tau$ of the corresponding bin varies rapidly [4]. The power delay profile is shown below in Figure 2-2.

It is found that the average power of the subsequent taps, \bar{P}_k , decay

exponentially (linearly on a decibel scale) with delay starting from the second bin, and may be expressed as

$$\bar{P}(\tau) = \sum_{k=1}^N \bar{P}_k \delta(\tau - \tau_k) = \bar{P}_1 \delta(\tau - \tau_1) + \sum_{k=2}^N \bar{P}_2 \exp\left(-\frac{(\tau_k - \tau_2)}{\varepsilon}\right) \delta(\tau - \tau_k) \quad (2.3)$$

$$= \bar{P}_1 \left\{ \delta(\tau - \tau_1) + \sum_{k=2}^N r \exp\left(-\frac{(\tau_k - \tau_2)}{\varepsilon}\right) \delta(\tau - \tau_k) \right\} \quad (2.4)$$

where N is the total number of bins in the observation window, $r = \bar{P}_2 / \bar{P}_1$ is the ratio of the average power of the second tap to the first tap, and ε is the exponentially power decay constant. It is noted that, \bar{P}_k are normalized to the power of the first tap, and τ_k are translated to the delay of the first tap.

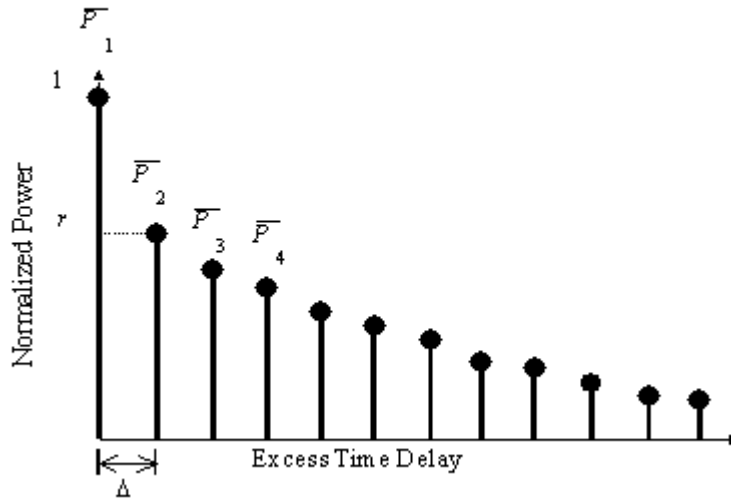


Figure 2-2 The average power delay profile versus the excess delay.

2.2.2 Saleh-Valenzuela Model (S-V)

The major difference between Saleh-Valenzuela model [4] and STDL model is that Saleh-Valenzuela model doesn't assume the arrival of paths on each sampling time interval. Instead, two Poisson models are employed in the modeling of the arrival

time. The first Poisson model is for the first path of each path cluster and the second Poisson model is for the paths (or rays) within each cluster. Following the terminology in [8], we define

T_l = the arrival time of the first path of the l -th cluster;

$\tau_{k,l}$ = the delay of the k -th path within the l -th cluster relative to the first path arrival time, T_l ;

Λ = cluster arrival rate;

λ = ray arrival rate, i.e., the arrival rate of path within each cluster.

By definition, we have $\tau_{0l} = T_l$. The distribution of cluster arrival time and the ray arrival time are given by

$$\begin{aligned} p(T_l | T_{l-1}) &= \Lambda \exp[-\Lambda(T_l - T_{l-1})], \quad l > 0 \\ p(\tau_{k,l} | \tau_{(k-1),l}) &= \lambda \exp[-\lambda(\tau_{k,l} - \tau_{(k-1),l})], \quad k > 0 \end{aligned} \quad (2.5)$$

The magnitude of the k -th path within the l -th cluster is denoted by β_{kl} . It is Rayleigh distributed with a mean given by

$$\overline{\beta_{kl}^2} = \overline{\beta^2(0,0)} \exp(-T_l / \Gamma) \exp(-\tau_{kl} / \lambda), \quad (2.6)$$

where $\overline{\beta^2(0,0)}$ is the average power of the first arrival of the first cluster.

Illustrations of channel impulse responses are shown below in Figure 2-3 and the double exponential decay model in Figure 2-4.

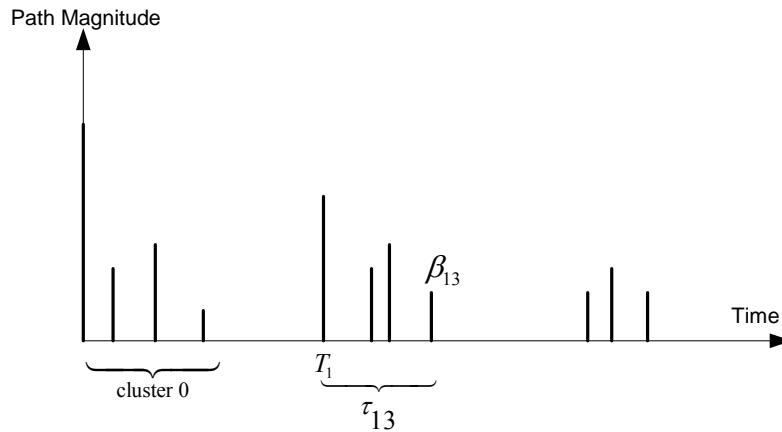


Figure 2-3 An illustration of channel impulse response.

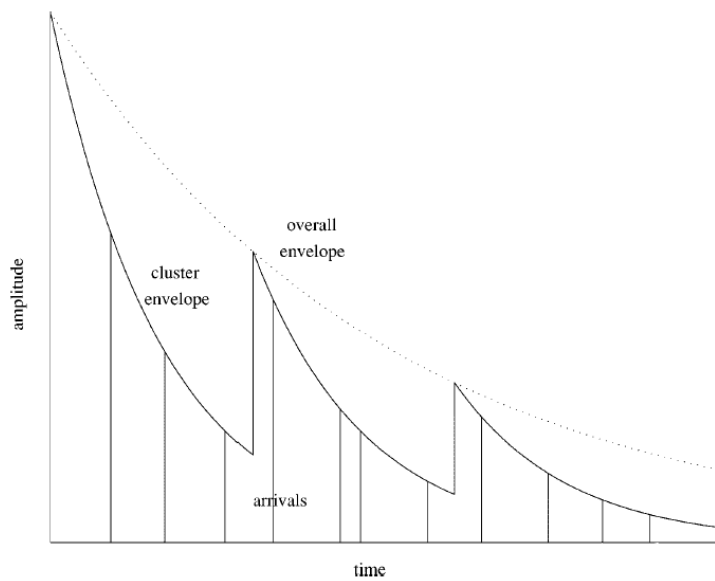


Figure 2-4 An illustration of exponential decay of mean cluster power and ray power within clusters.

2.2.3 Turin's Δ -K Model

Turin's Δ -K model [10] proposes a modified Poisson process to take into account the possibility that multipath may arrive in-group. In this model, time axis is partitioned into bins with width Δ which is equal to the time resolution of the transceiver, the arrival rate of multipath is a function of whether or not an arrival occurred in the previous bin, and is a function of empirically based measurements of the probability of path occurrences at different delays. It can be stated as the branching process of Figure 2-5: when a path occurs in bin i , the path arrival rate of

the next bin λ_{i+1} is increased by a factor K . For $K > 1$, the process exhibits a clustering property and large K leads a large clustering phenomenon. For $K=1$, this process reverts to a standard Poisson process. It is noted that the clustering phenomenon or K value is dependent on the propagation environment.

As shown in Figure 2-5, there exists the following relation between the empirical path occurrences rate P_i , and the path arrival rate λ_i .

$$\lambda_i = \frac{P_i}{(K-1)P_{i-1} + 1} \quad (i \neq 1) \quad (2.7)$$

where $\lambda_1 = P_1$.

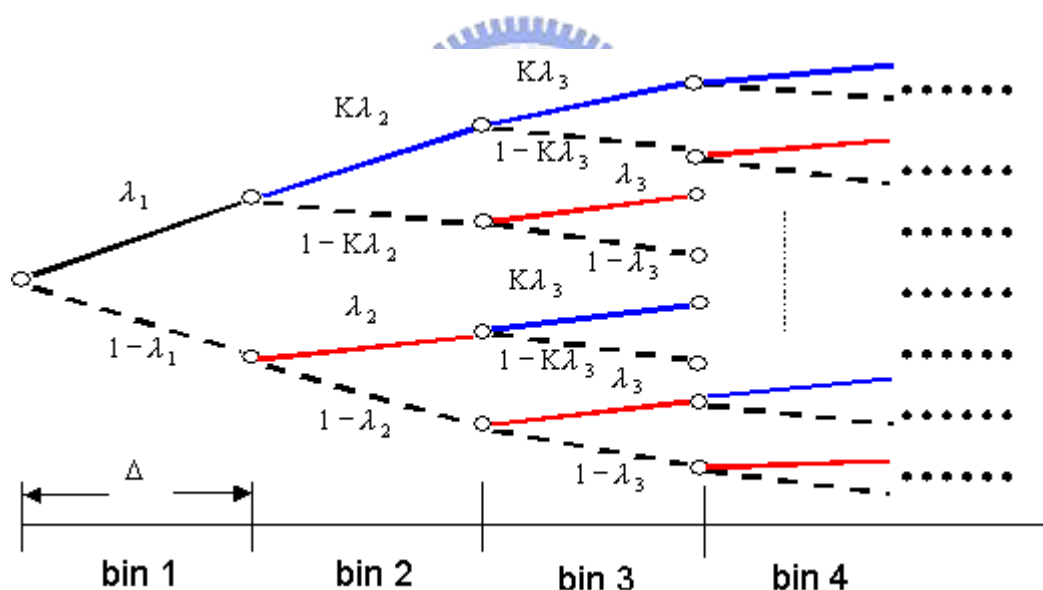


Figure 2-5. Illustration of the Δ - K process.

The impulse response of bin i is denoted as α_i , and the path amplitude $|\alpha_i|$ is lognormal distributed with an exponentially decaying multipath intensity profile (MIP).

$$E[|\alpha_i|^2] = \Omega_0 e^{-T_i/\tau} \quad (2.8)$$

where T_i is the excess delay of bin i and Ω_0 is the mean power of the first path of the first cluster.

This model can also capture the multipath clustering phenomenon, similar to the S-V model.



2.3 Received Envelope Distribution

The small-scale effects are manifested in the changes of the PDP caused by small changes of the receiver position, while the environment around the receiver does not change significantly. The statistics of small scale signal fading on individual multipath components can provide insight into jitter and equalizer requirements.

Most common distributions found in literature, used to describe rapid fading variations, are the Rayleigh, Rice, Nakagami, and Lognormal distributions [11]. Several amplitude distribution of the multipath components have been described in below.

2.3.1 Rayleigh Fading

When the composite received signal consists of a large number of plane waves, the received envelope has a Rayleigh distribution, i.e.

$$p_z(x) = \frac{x}{\sigma^2} \exp\left\{-\frac{x^2}{2\sigma^2}\right\} \quad (2.9)$$

For a Rayleigh distributed envelope, the average power is $\Omega_p = 2\sigma^2$, so that

$$p_z(x) = \frac{2x}{\Omega_p} \exp\left\{-\frac{x^2}{\Omega_p}\right\} \quad (2.10)$$

Rayleigh fading usually applies to any scenario where there is no LOS path between the transmitter and receiver antennas.

2.3.2 Rician Fading

For a multipath-fading channel containing a LOS component, the complex envelope has a Rician distribution, i.e.

$$p_z(x) = \frac{x}{\sigma^2} \exp\left\{-\frac{x^2 + s^2}{2\sigma^2}\right\} I_0\left(\frac{xs}{\sigma^2}\right) \quad (2.11)$$

The Rice distribution is often characterized by the K -factor that is defined as the ratio of the power of the direct path component s^2 and the random one

$2\sigma^2, K = s^2 / 2\sigma^2$ ($K \geq 0$). When $K=0$ the channel exhibits Rayleigh fading, and when $K = \infty$ the channel does not exhibit fading. For a Rician distributed envelope, the average power $\Omega_p = s^2 + 2\sigma^2$, so that

$$p_z(x) = \frac{2x(K+1)}{\Omega_p} \exp\left\{-K - \frac{(K+1)x^2}{\Omega_p}\right\} I_0\left(2x\sqrt{\frac{K(K+1)}{\Omega_p}}\right) \quad (2.12)$$

2.3.3 Nakagami Fading

The Nakagami distribution was introduced by Nakagami in the early 1940's to characterize rapid fading in long distance HF channels [12]. The Nakagami distribution was selected to fit empirical data, and is known to provide a closer match to some experimental data than either the Rayleigh, or Ricean distributions [13]. In essence, the Nakagami distribution describes the received envelope, i.e.

$$p_z(x) = \frac{2m^m x^{2m-1} (K+1)}{\Gamma(m)\Omega_p^m} \exp\left\{-\frac{mx^2}{\Omega_p}\right\} \quad m \geq \frac{1}{2} \quad (2.13)$$

The Nakagami distribution is often used to model multipath fading for the following reasons. First, the Nakagami distribution can model fading conditions that are either more or less severe than Rayleigh fading. When $m=1$, the Nakagami distribution becomes the Rayleigh distribution, when $m=1/2$ it becomes a one-sided Gaussian distribution. Second, the Rice distribution (which does have physical significance) can be closely approximated by using the relation $m = \frac{(K+1)^2}{(2K+1)}$, between the Rice factor K and Nakagami parameter m [12].

Chapter 3

Measurement System and Environment

In a typical indoor environment, due to reflection, refraction and scattering of radio waves by structures inside a building, the transmitted signal most often reaches the receiver by more than one path, resulting in a phenomenon known as multipath fading. In UWB pulse transmission, the effect is to produce a series of delayed and attenuated pulses (echoes) for each transmitted pulse.

The main objective of a channel sounding is to model the UWB channel correctly. Consequently, if the multipath is well characterized, transmitter and receiver can be designed in order to decrease the consequences of these phenomena.

In order to obtain the channel characteristics in different environments, the UWB channel measurement methods are proposed for analyzing each composition of multipath response. We also classified the propagation scenarios into four categories base on measurement report [7]:

1. LOS (Line-of-Sight) scenario, the scope of distance between transmitter and receiver is 0-4m.
2. LOS scenario, the scope of distance between transmitter and receiver is 4-10m.
3. NLOS (Non-Line-of Sight) scenario, the scope of distance between transmitter and receiver is 0-4m.
4. NLOS scenario, the scope of distance between transmitter and receiver is 4-20m.

3.1 Measurement System and Setup

In order to obtain the channel characteristics, the UWB channel measurement is performed to analyze the MPCs. A typical frequency domain channel sounder is shown in Fig. 3-1. A vector network analyzer contains a synthesized frequency sweeper and an S-parameter test set. At Port 1 the S-parameter test set transmits a known signal level for each frequency step and detects the received complex response of the channel, $S_{21}(f)$, at port 2.

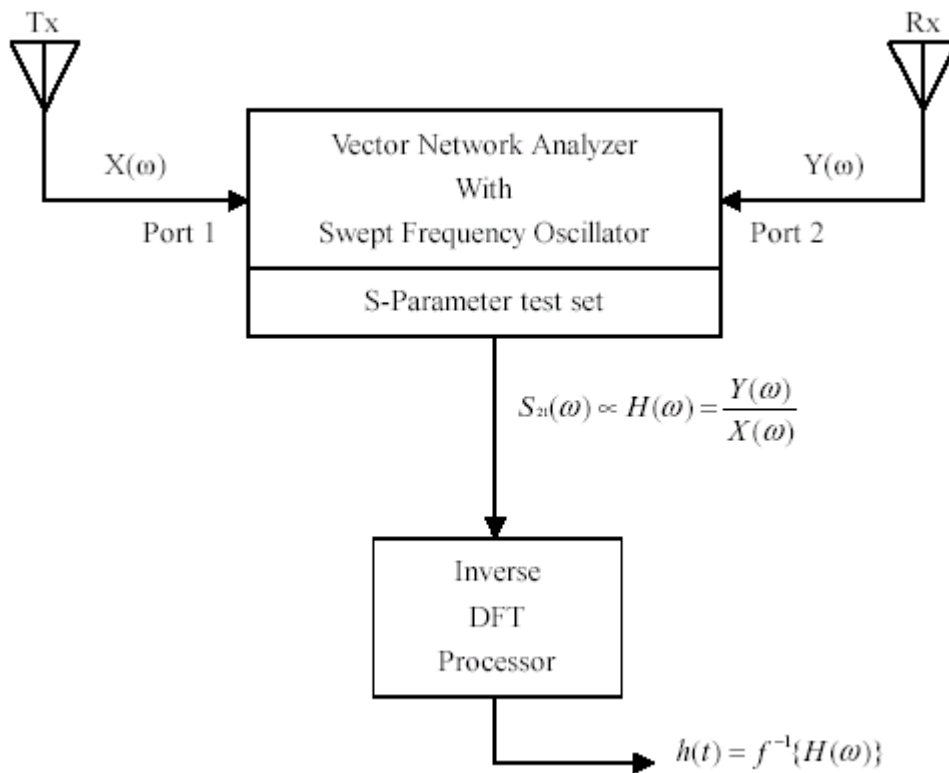


Figure 3-1 Frequency domain channel response measurement system [9].

In our study is performed in frequency domain through a Vector Network Analyser whose specifications are detailed further. This method consists in exciting the channel with tones over a wide range of frequencies. The attenuation and phase shift of each frequency component caused by the propagation medium is measured. Moreover, the exact time-domain response is also obtained by taking the inverse

Fourier transform. Each measurement is performed in time and frequency domain thanks to the Vector Network Analyzer. This device will be commanded through the LAN network for exporting the S21 parameters representing the linear attenuation factor in domains, frequency and time. For UWB application, the swept frequency band is from 3GHz to 5GHz (2GHz of frequency span). With 2.5MHz steps, corresponding to 801 points, we would be able to detect multipath with a time delay up to 400ns

An Agilent 8719ET Vector Network Analyzer (VNA) is exploited to measure the channel response between two ends. The transmitted signal is sent from the VNA to the transmitting antenna through a low-loss 10-m coaxial cable. For our measurement campaign, we used a pair of omni-directional wideband antennas by Electro-Metrics (EM-6865), which frequency range is 2-18 GHz and antenna gain is 0dBi. The signal from the receiving antenna through a preamplifier (with a gain of 30 dB) via a low-loss 30-m coaxial cable, then returned to port2 of the VNA. Besides the network analyzer, the time-domain channel response can be obtained by taking the inverse Fourier transform (IFFT) of the frequency-domain channel response. Table 3-1 lists the main parameters in the measurement.

During the measurement, both the Rx and Tx antennas are at a height 1.5m above the ground. The measurement system is shown in Figure 3-2 and Figure 3-3. The radiation pattern is described in Figure 3-4.

Parameter	Value
Frequency band	3GHz to 5GHz
Bandwidth (frequency span)	2GHz
Number of points over the band	801
Transmitted power	10dBm
Preamplifier gain	30dB
Antenna gain	0dBi

Table 3-1 The main parameters in the measurement.

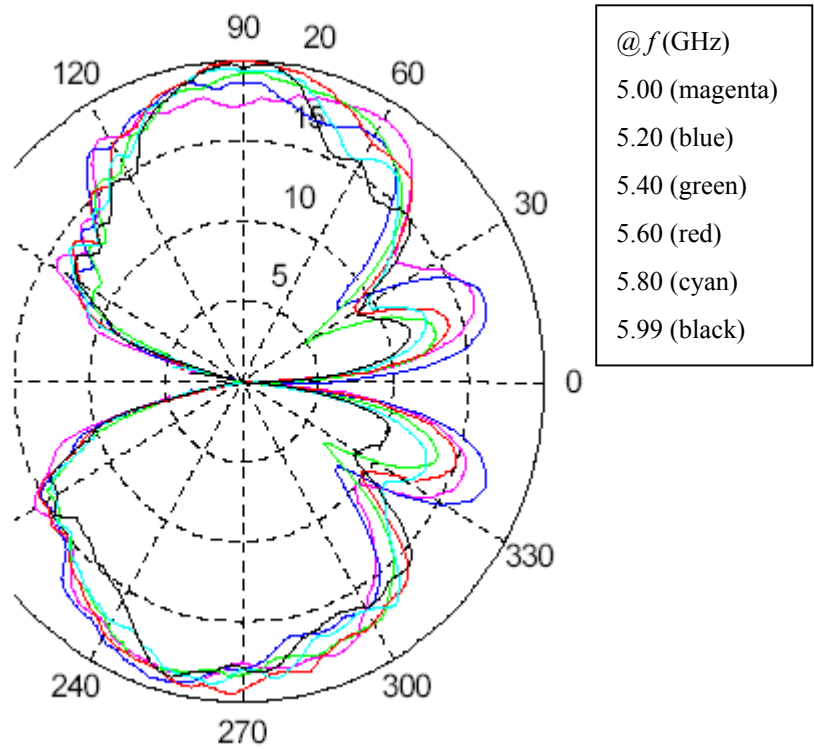
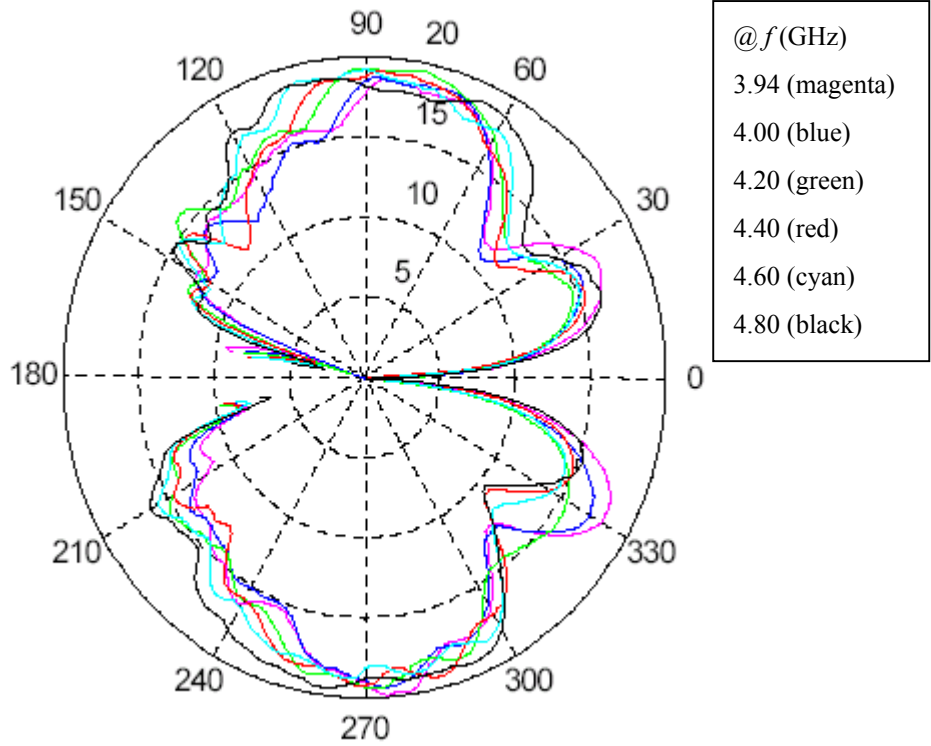




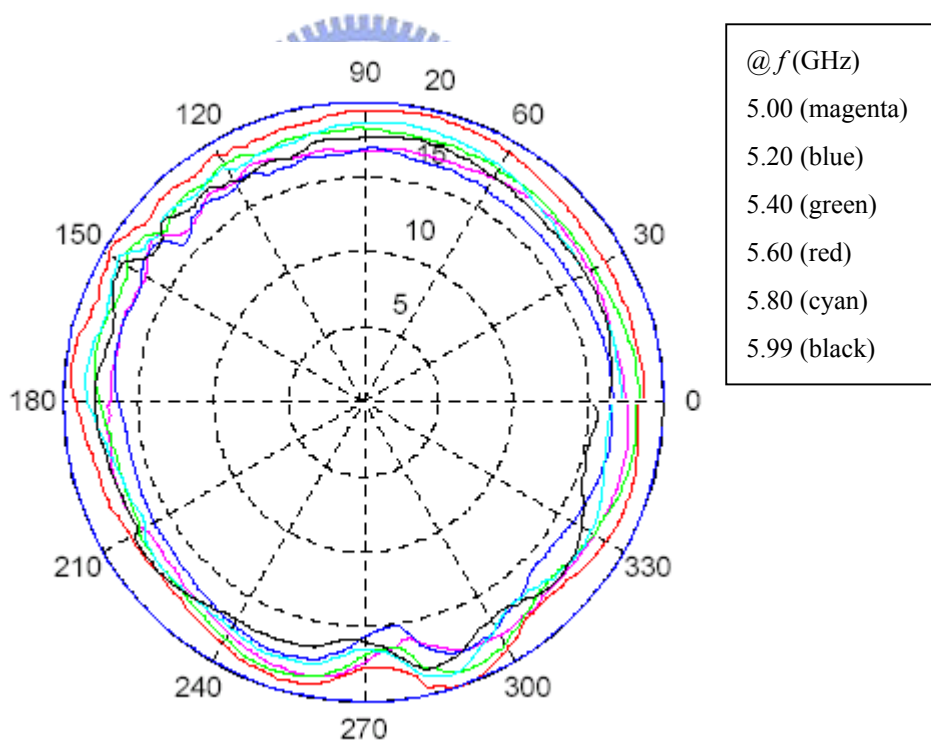
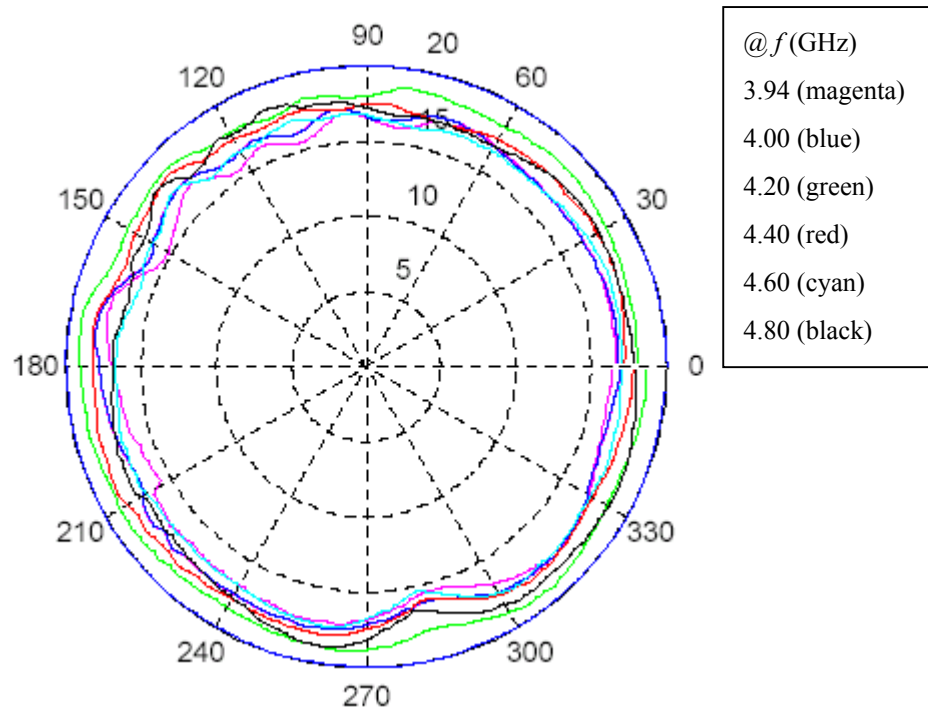
Fig. 3-2 A photo of the frequency domain channel sounding system.



Fig. 3-3 A photo of the wideband antenna.



(a)



(b)

Figure 3-4 (a) Vertical and (b) Horizontal pattern of the transmitted and received antennas.

3.2 Measurement Environment Description

The measurement was performed in 2nd floor, 3rd floor, 7th floor, and 9th floor of the 4th Engineering Building at the National Chiao-Tung University, Hsinchu, Taiwan. The floor layouts of these measurement sites are shown in Fig. 3-6. In order to minimize the grid number, channel frequency responses measurements were sampled at 441 measurement subpoints, arranged in a 21×21 square grid. The spacing between two neighboring subpoints is 1.875cm. Rician factor was be statistics and calculated for different square grid (corresponding to the center of 21×21square grid). The Rician factor values become unstable as grid number smaller than 6. In order to obtain large number of measurement samples, we selected 8×8 square grid. The result is described in figure 3-5.

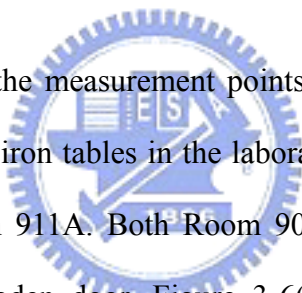
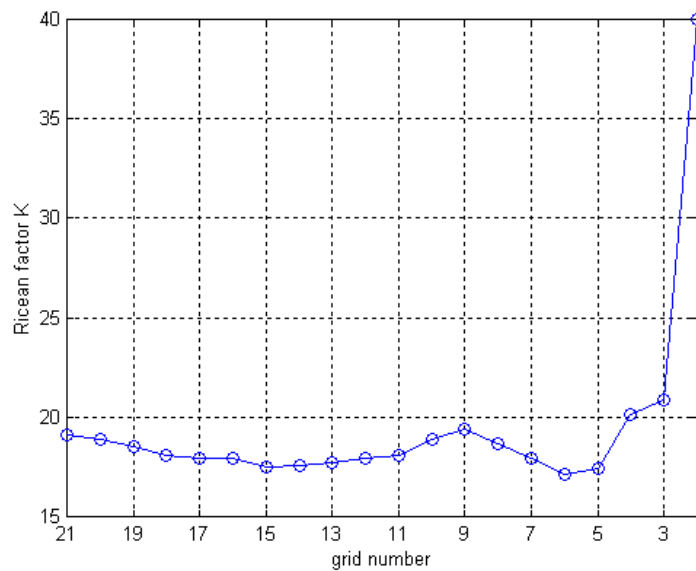
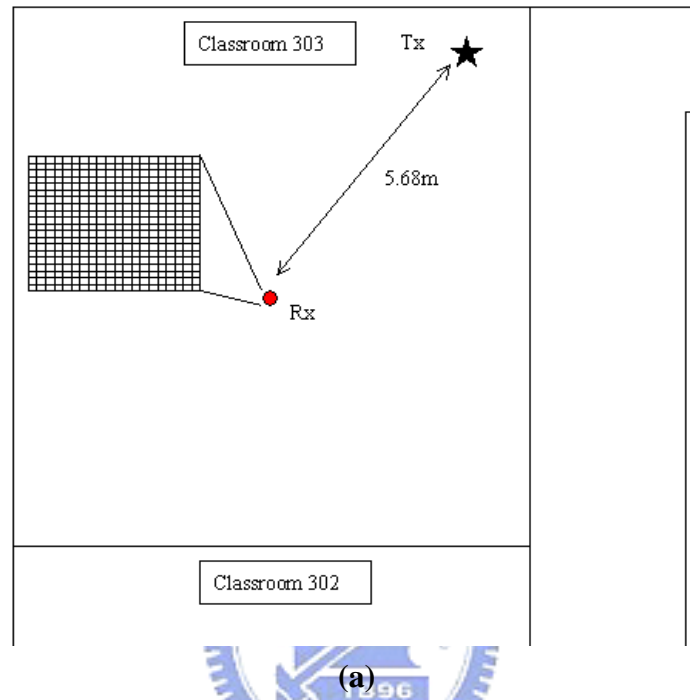


Figure 3-6(a) illustrates the measurement points in Room 901; there are many measurement equipments and iron tables in the laboratory. In figure 3-6(b), there are six measured points in Room 911A. Both Room 901 and 911A are enclosed with gypsum-board walls and wooden door. Figure 3-6(c) illustrates the measurement points in Room 203; there are many wooden chairs in the classrooms. In figure 3-6(d), there are four measured points in Room 215. Both Room 203 and 214 are lightly cluttered with wooden chairs. In Figure 3-6(e), the Room 303, 302, and 301 were under NLOS condition with Tx at hallway. In Figure 3-6(f), there are ten iron tables in the Room 713, and there are five computers on each table. Thus obstructed LOS always exists in this measurement environment. In each receiver location, channel frequency responses measurements were made at 64 measurement points, arranged in a fixed-height, 8×8 square grid with 3.75cm spacing, covering 26.25cm×26.25cm. A total of 2688 different channel frequency responses were recorded. One side of the grid is always parallel to wall of the room. The propagation scenarios into four

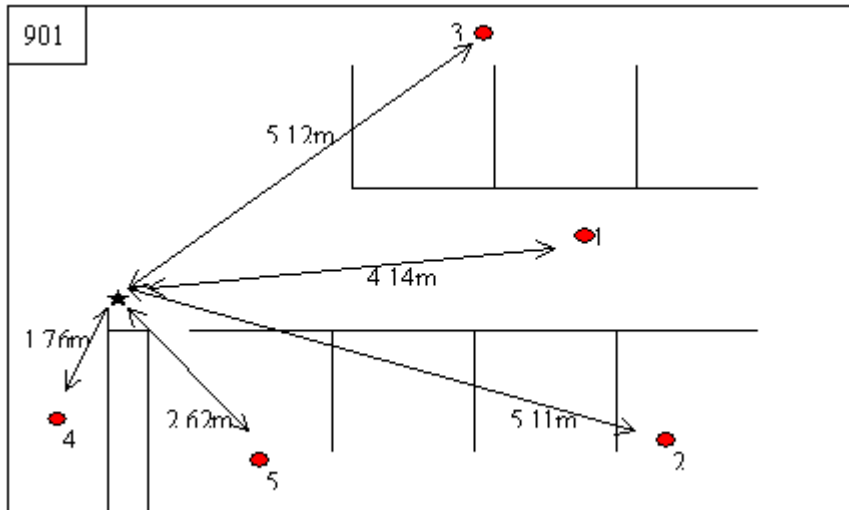
categories are described in Table 3-2.

The frequency response data have been exploited to analyze the UWB channel characteristics. We observe the frequency response between 3GHz to 5GHz with 801 sweep points.

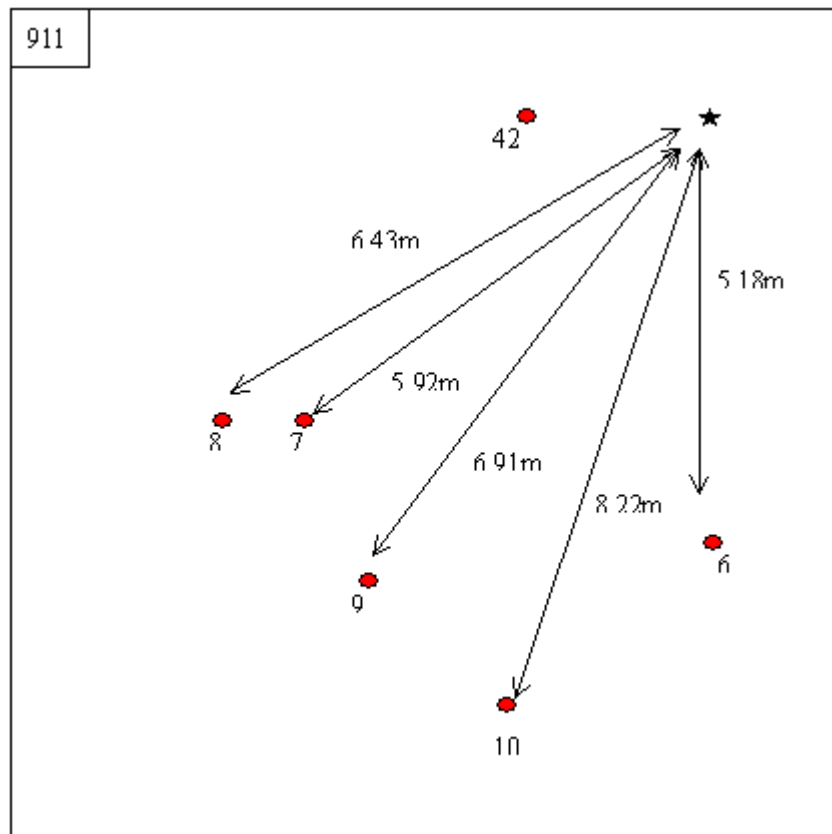


(b)

Fig. 3-5 (a) Small-scale variation square grid; (b) The variation of Rician factor for different square grid.

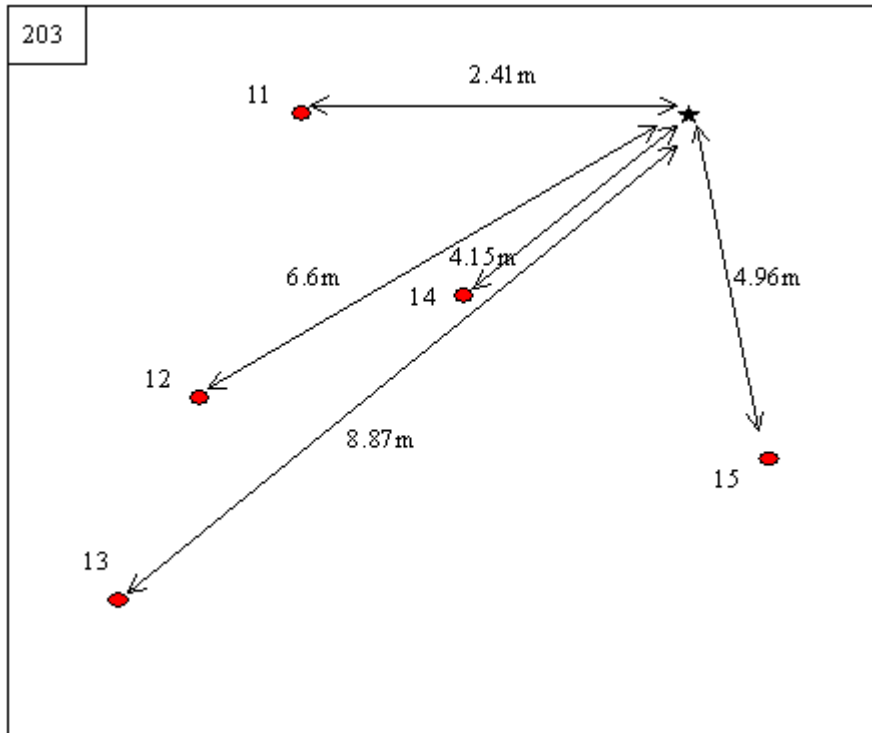


(a)

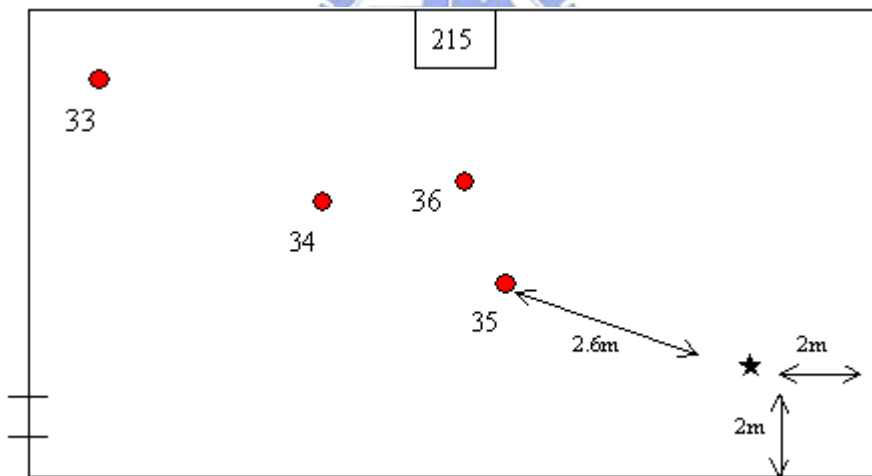


(b)

Figure 3-6 9th floor layout of the 4th Engineering Building. (a) There are 5 measured points in Room 901; (b) There are 6 measured points in Room 911A.



(c)



(d)

Figure 3-6 2nd floor layout of the 4th Engineering Building. (c) There are 5 measured points in Room 203; (d) There are 4 measured points in Room 215.

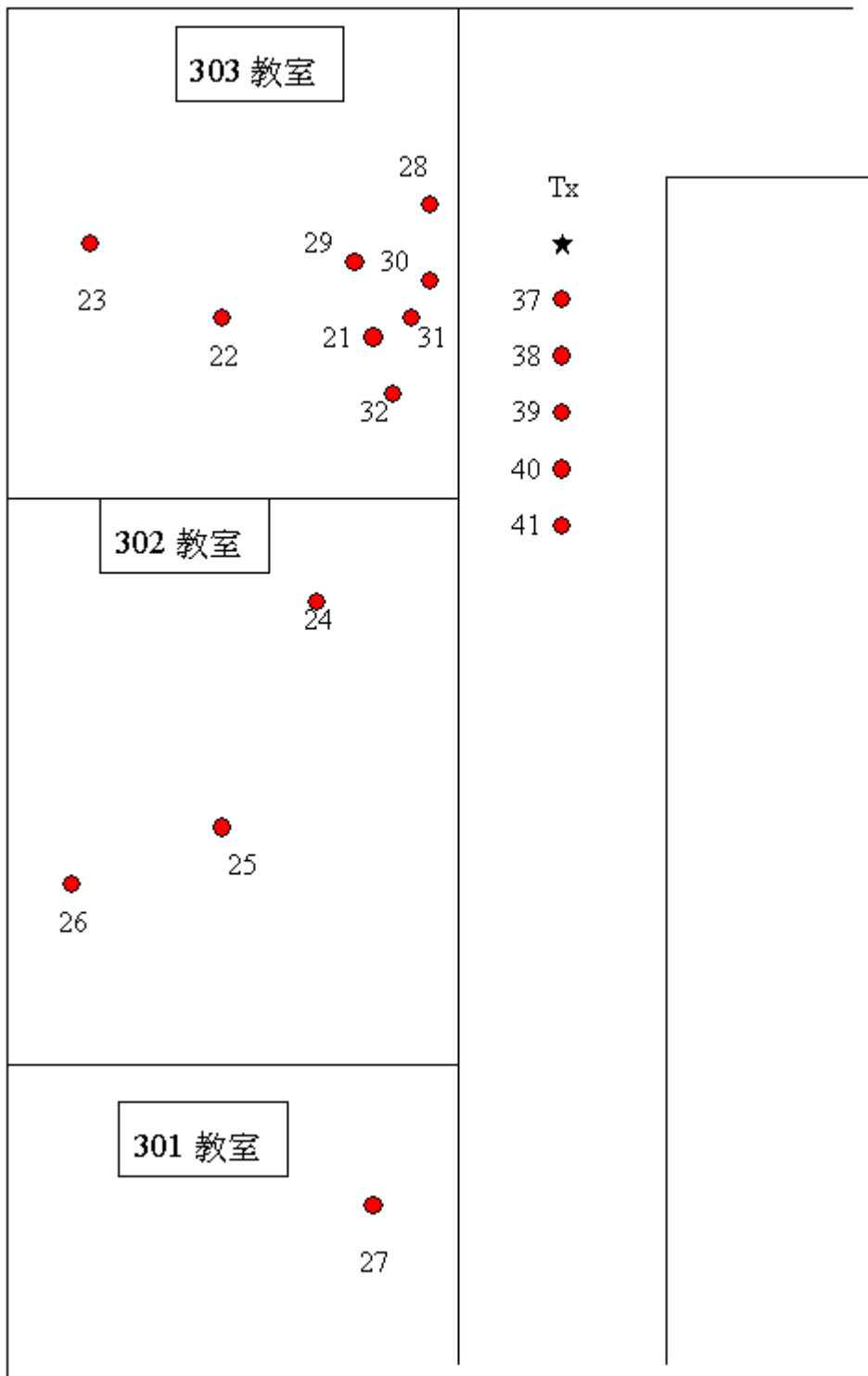


Figure3-6 (e) 3rd floor layout of the 4th Engineering Building.

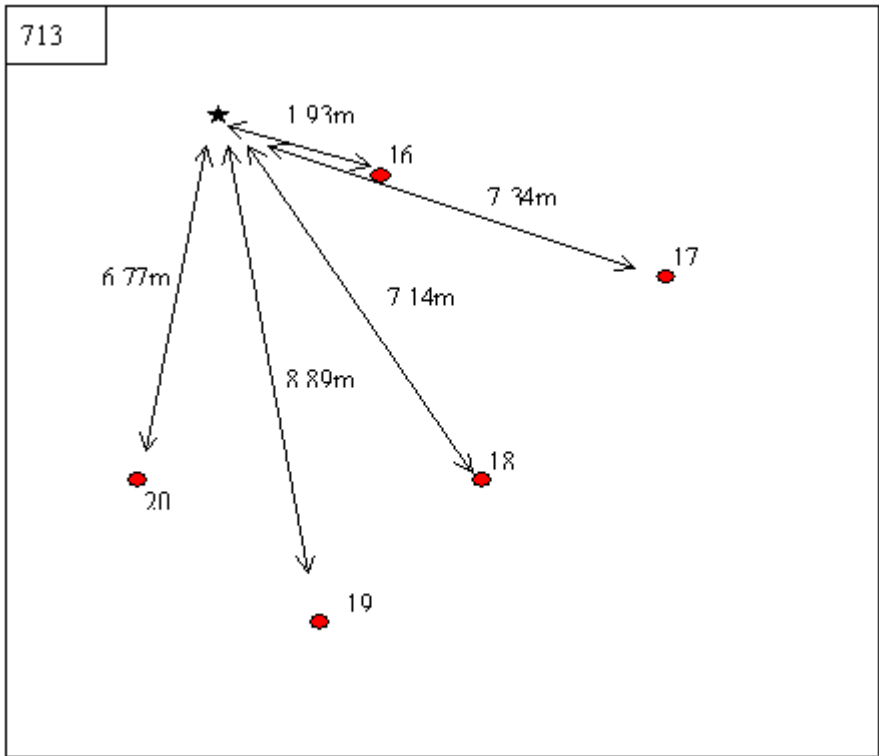
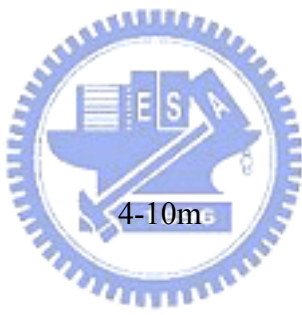


Figure 3-6 (f) 7th floor layout of the 4th Engineering Building.



Table 3-2 The different channel scenarios.

Environment	Distance (Tx-Rx)	Point
LOS	0-4m	4
		5
		11
		16
		34
		35
		36
		37
		38
		42
		1
		6
		7
		8
		12
		13
		14
		15
		17
		18
		19
20		
33		
39		
40		
41		
NLOS	0-4m	21
		28
		29
		30
		31
		32
	4-20m	2
		3
		9

		10
		22
		23
		24
		25
		26
		27



3.3 Measurement Result

A total of 42 measured points in the 4th Engineering Building were chosen for measurement data. At each measurement point, the receiver was located at 64 different subpoints separated by one half wavelength λ ($\lambda = 7.5$ cm). At each subpoint the power delay profile was recorded with the help of a portable computer for subsequent processing. Power delay profiles obtained from the measured frequency-domain channel responses to time-domain by taking the inverse Fourier transform (IFFT). A series of typical power delay profile for the 64 receiver locations at a LOS site and at a NLOS site are shown in Figures 3-7(a), (b).

Figure 3-7(a) illustrates that the power delay profile has a large initial pulse, followed by delayed pulses of small amplitude. Even though LOS conditions exist, the main received pulse is composed of two or more ray arrivals, as evidenced by spatial fading as the receiver position is moved. It appears that the fading is due to interference between the direct and reflected rays.

The power delay profiles in Figure 3-7(b) for a NLOS site exhibit many individually identifiable peaks whose amplitudes vary rapidly with the location of the receiver.

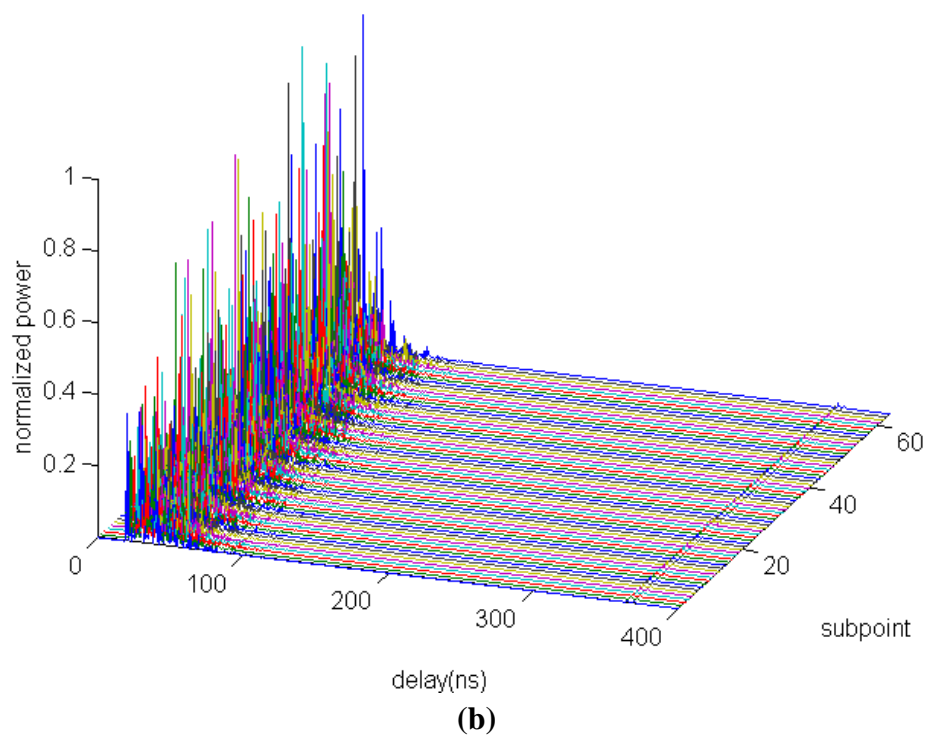
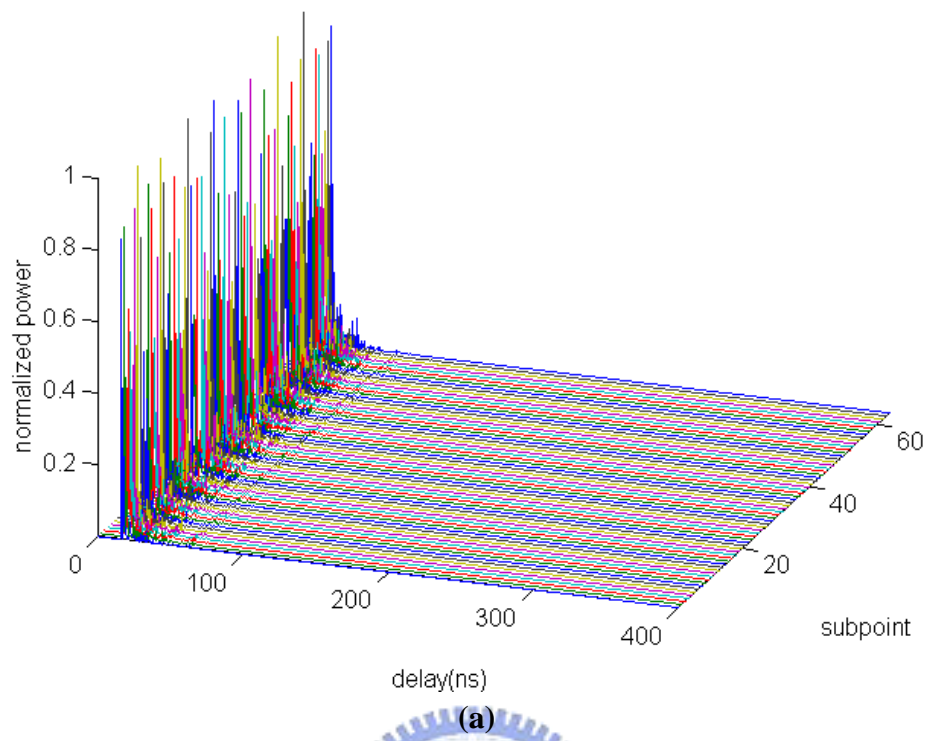


Figure 3-7 Power delay profiles measured at 64 locations separated by $\lambda/2$ on indoor. (a)The measured PDP at no.1 of LOS situation; (b) The measured PDP at no.2 of NLOS situatio.

Chapter 4

Effects of Signal Bandwidth and Propagation on UWB Channels

In this chapter, effects of signal bandwidth and propagation on indoor UWB channels are investigated through the analysis of UWB measurement. On one hand the parameters of the STDL model will be investigated to see how it changes as the signal bandwidth varies. With the STDL model, the power ratio and decay constant of the sampled power delay profiles will be extracted from the measurement data, which can quantify the channel characteristics. It is found that they are dependent on signal bandwidth and local scatterer distribution around the receiver and the transmitter. On the other hand, amplitude fading statistics has been explored. Due to the extreme wide signal bandwidth, UWB systems achieve very high multipath resolution and only few multipath components exist within each resolvable delay bin, and the amplitude fading statistics for NLOS (Non Light-of-Sight) may no longer follow Rayleigh distribution. We had observed this phenomenon from the measured data and found that the received amplitude can be described well by Nakagami distribution. For LOS situation, the received amplitude of the first bin can be described well by Rician distribution.

4.1 Effect of Bandwidth and Propagation on Instantaneous Power Delay Profile

At each subpoint instantaneous PDP was sampled and there are 64 samples of each measured point. Every PDP was normalized by its peak power. With the STDL model, the PDP can be described by using power ratio r and decay constant ε as

described in Section 2.2.1.

Figures 4-1 (a), (b), (c) and (d) illustrate the normalized instantaneous PDPs of subpoint no.110 measured in Room 901 with signal bandwidths 2 GHz, 1.5 GHz, 1 GHz and 500 MHz, respectively. Here, the power ratio r is increased as the bandwidth decreases. From Equation (2.4), the power of each bin, P_j^F , with bandwidth F , can be expressed as

$$\begin{cases} P_1^F = 1 \\ P_j^F = r^F \times \exp\left[-\frac{(j-2) \times \Delta^F}{\varepsilon^F}\right], \quad j \geq 2 \end{cases} \quad (4.1)$$

When bandwidth is decreased to half, $f=F/2$,

$$\begin{cases} P_1^f = P_1^F + P_2^F = 1 + r^F \\ P_i^f = P_{2i-1}^F + P_{2i}^F = r^F \times \left\{ \exp\left[-\frac{(2i-3) \times \Delta^F}{\varepsilon^F}\right] + \exp\left[-\frac{(2i-2) \times \Delta^F}{\varepsilon^F}\right] \right\} \\ = r^F \times \left[\exp\left(-\frac{\Delta^F}{\varepsilon^F}\right) + \exp\left(-\frac{2 \times \Delta^F}{\varepsilon^F}\right) \right] \times \exp\left(-\frac{(i-2) \times 2 \times \Delta^F}{\varepsilon^F}\right), \quad i \geq 2 \end{cases} \quad (4.2)$$

the power of second bin can be expressed as

$$P_2^f = P_3^F + P_4^F = r^F \times \left\{ \exp\left[-\frac{\Delta^F}{\varepsilon^F}\right] + \exp\left[-\frac{2 \times \Delta^F}{\varepsilon^F}\right] \right\} \quad (4.3)$$

then the power ratio with bandwidth f can be expressed as

$$\begin{aligned} r^f &= \frac{r^F}{1 + r^F} \times \left[\exp\left(-\frac{\Delta^F}{\varepsilon^F}\right) + \exp\left(-\frac{2 \times \Delta^F}{\varepsilon^F}\right) \right] \\ &\approx \frac{2 \times r^F}{1 + r^F} \end{aligned} \quad (4.4)$$

However, the decay constant ε is independent of the signal bandwidth. When bandwidth is decreased to half, the power of each bin, P_i^f , with bandwidth $f=F/2$, can

be expressed as

$$\begin{cases} P_1^f = 1 \\ P_i^f = r^f \times \exp\left[-\frac{(i-2) \times \Delta^f}{\varepsilon^f}\right], \end{cases} \quad i \geq 2 \quad (4.5)$$

Comparing Equations (4.2) and (4.5), it is found that the decay constant is not dependent on the bandwidth since ε^f and ε^F are equal ($\Delta^f = 2 \times \Delta^F$).

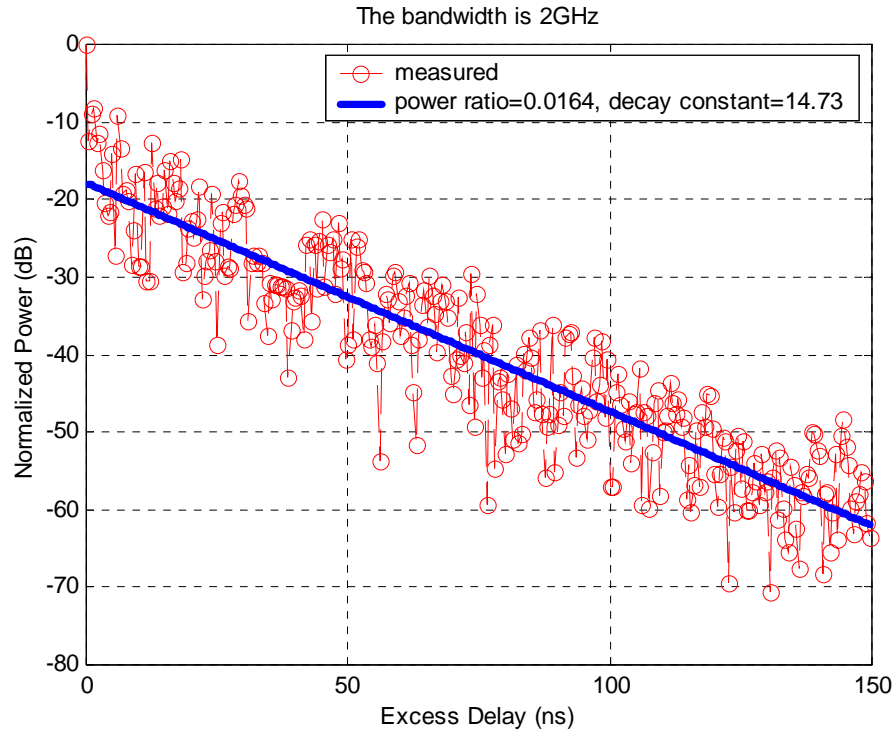
Figures 4-2, 4-3 and 4-4 shows the normalized instantaneous PDPs measured at subpoints no.124, 2430 and 2450, respectively. The first subpoint is in LOS situation and the other two subpoints are in Room 303 of NLOS situation. In each figure, PDPs for signal bandwidths of 2 GHz, 1.5 GHz, 1 GHz and 500 MHz are also illustrated. From these figures, the trend of the power ratio or the decay constant versus signal bandwidth is the same as that in figure 4-1. However, due to local scattering effect, PDPs of the subpoints belong to the same point such as subpoints 110 with 124 and subpoints 2430 and 2450 are quite different. For further investigation, 64 sampled PDPs of each point were collected to calculate the corresponding power ratio and decay constant. Figures 4-5 (a), (b), and (c) illustrate power ratio histograms of point No.1 with signal bandwidths 2 GHz, 1 GHz and 500 MHz, respectively. It is found that these histograms can be well-fitted by a lognormal distribution. Figures 4-6 (a), (b), and (c) illustrate decay constant histograms of point No.1 with signal bandwidths 2 GHz, 1 GHz and 500 MHz, respectively. The decay constant histogram can also be well described by a lognormal distribution.

Figure 4-7 illustrates the power ratio versus signal bandwidth for the LOS 0-4m situation. It is found that the power ratio r is increased when the bandwidth is decreased. Figure 4-8 illustrates the decay constant versus signal bandwidth for the LOS 0-4m situation. It is found that the decay constant is only slightly dependent on the signal bandwidth. Similar results are observed for situations of LOS 4-10 m,

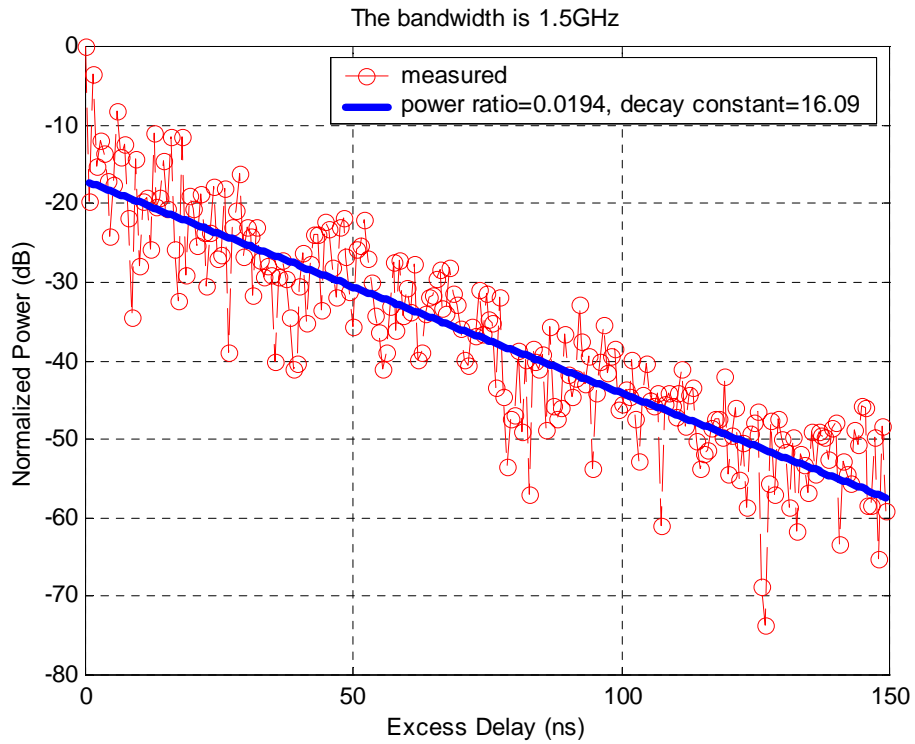
NLOS 0-4 m and NLOS 4-20m.

In addition, we consider local scatterer effect on instantaneous PDP. Figure 4-15(a) illustrates that there are local scatterers distributed closed to the receiver within a radius of 20cm in a laboratory. Figure 4-15(b) illustrates there are slightly far local scatterers distributed around the receiver within a radius of 45cm in the laboratory.

Figure 4-16(a) describes no local scatterer near the receiver. There are less multipath components within the second bin. It leads to the power ratio decrease. Figures 4-16(b) and (c) describes farer scatterer and nearer scatterer distribution around the receiver, respectively. There are more multipath components within the second bin from those scatterers, the multipath components lead to the larger power ratio and smaller decay constant. Figures 4-17 illustrate power ratio histograms of different local scatterers distribution around the receiver conditions. The power ratio is increased as the local scatterers move closer to receiver. Figures 4-18 illustrate decay constant histograms of different local scatterers distribution around the receiver conditions. The decay constant is decreased as the local scatterers move closer to receiver.



(a)



(b)

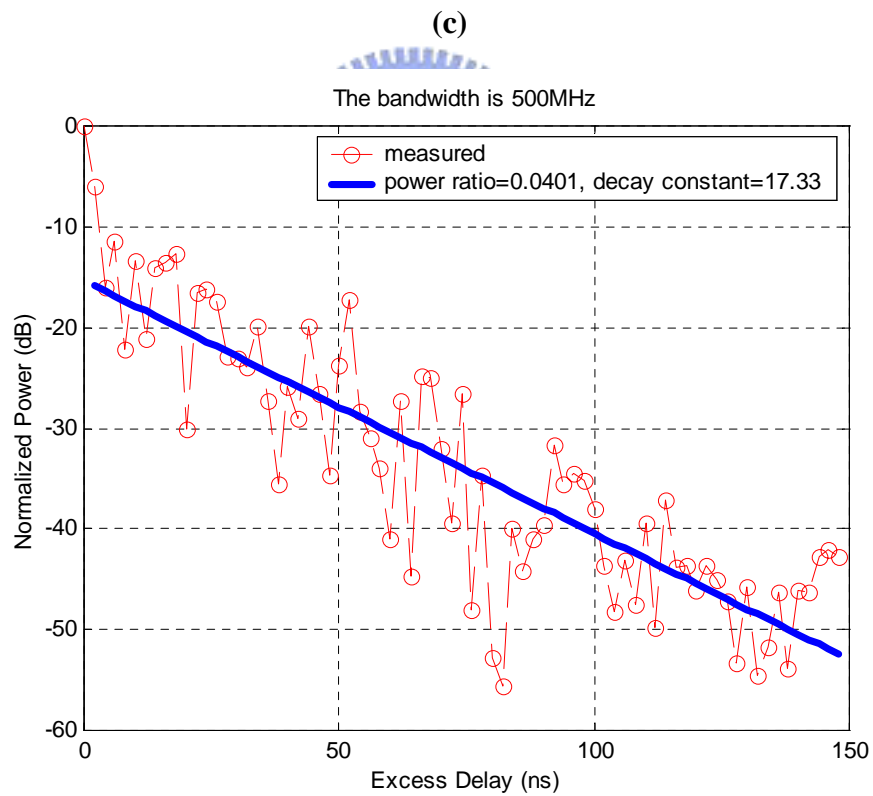
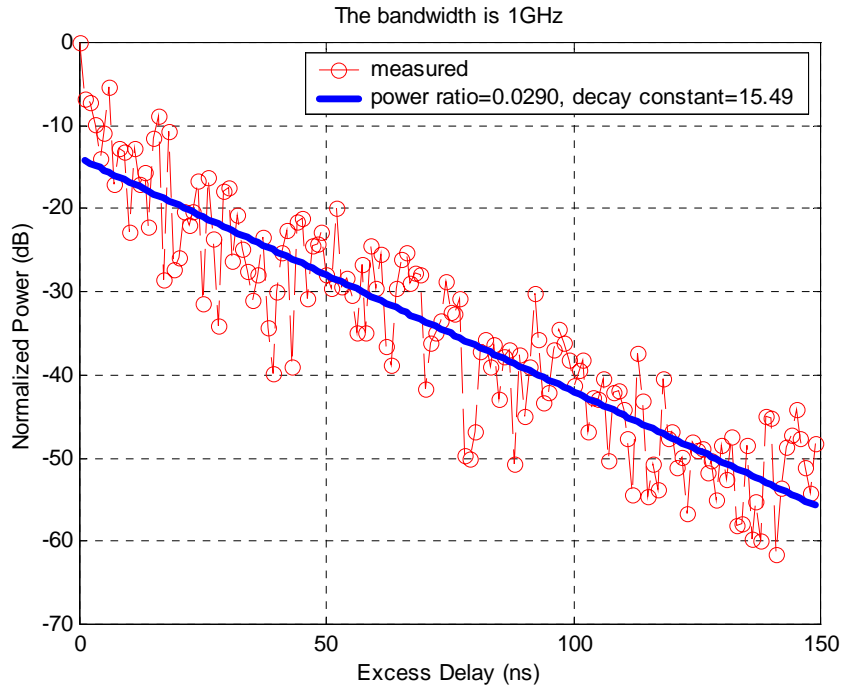
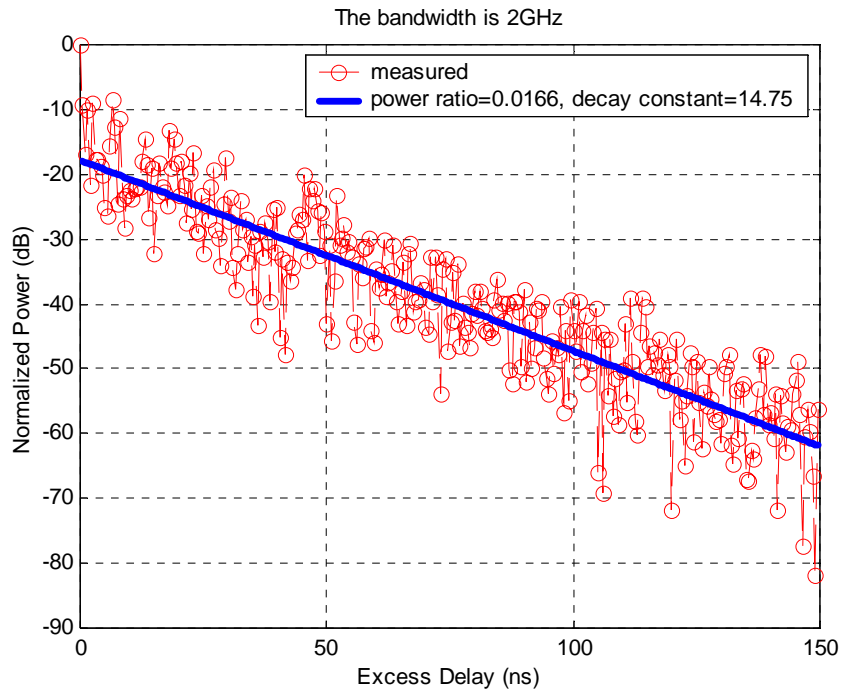
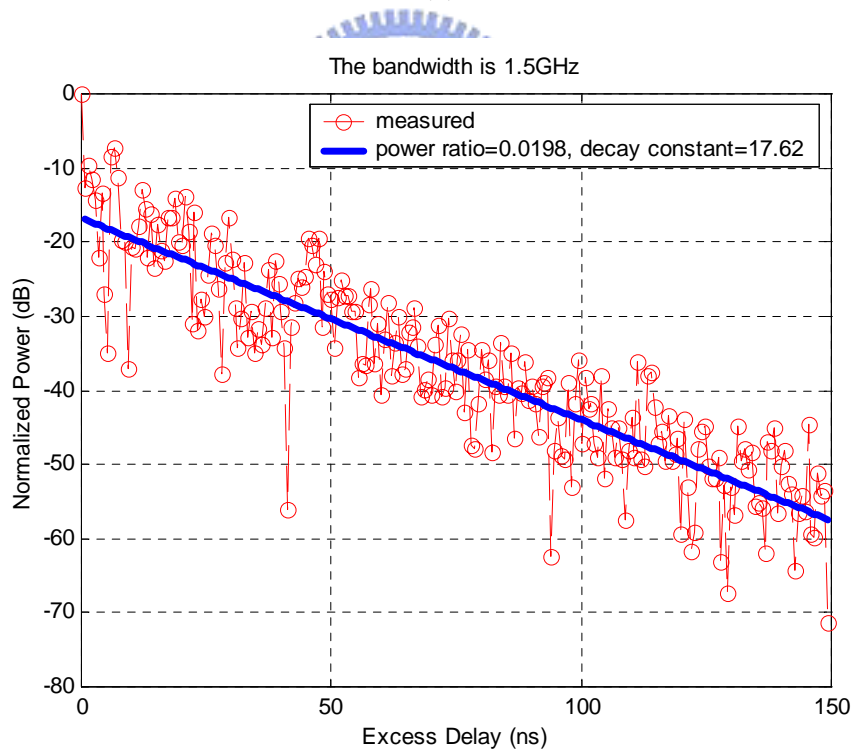


Figure 4-1 The normalized instantaneous PDP of subpoint no.110 in Room 901 for different bandwidth. (a) The bandwidth is 2 GHz with power ratio $r=0.016$, decay constant $\varepsilon =14.73$ (ns); (b) The bandwidth is 1.5 GHz with $r=0.019$, $\varepsilon =16.09$ (ns); (c) The bandwidth is 1 GHz with $r=0.029$, $\varepsilon =15.49$ (ns); (d) The bandwidth is 500 MHz with $r=0.041$, $\varepsilon =17.33$ (ns).



(a)



(b)

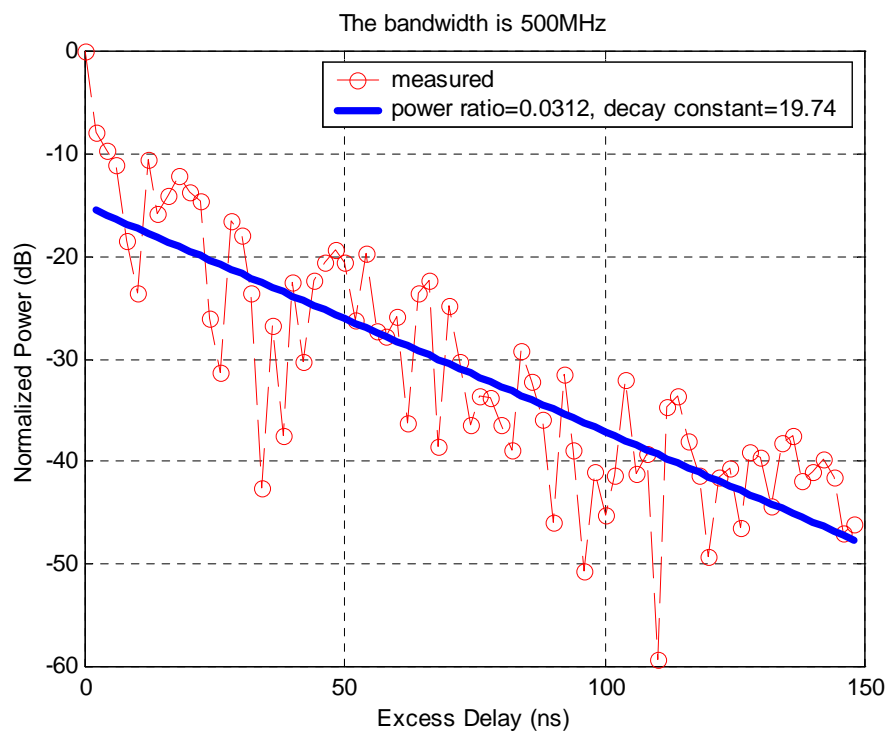
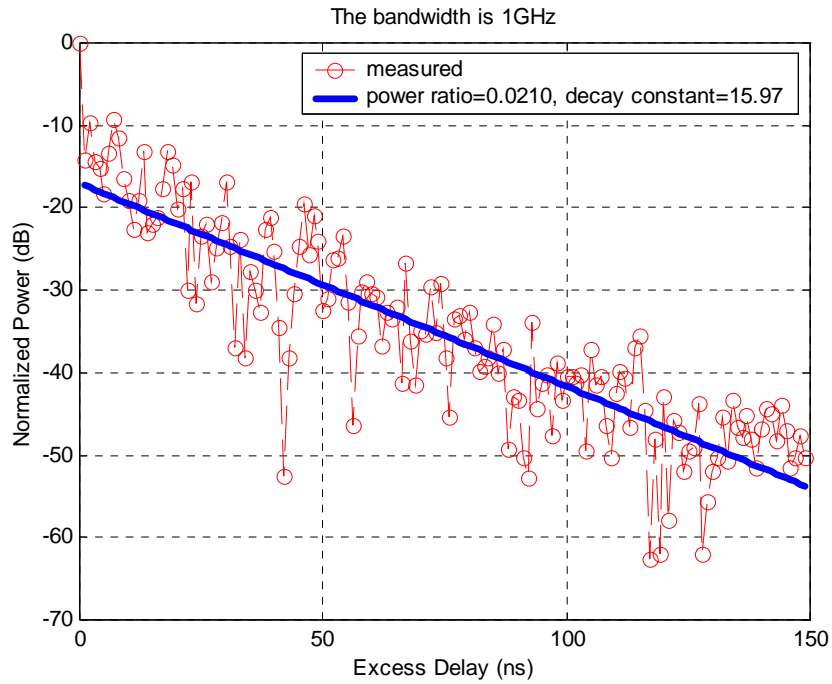
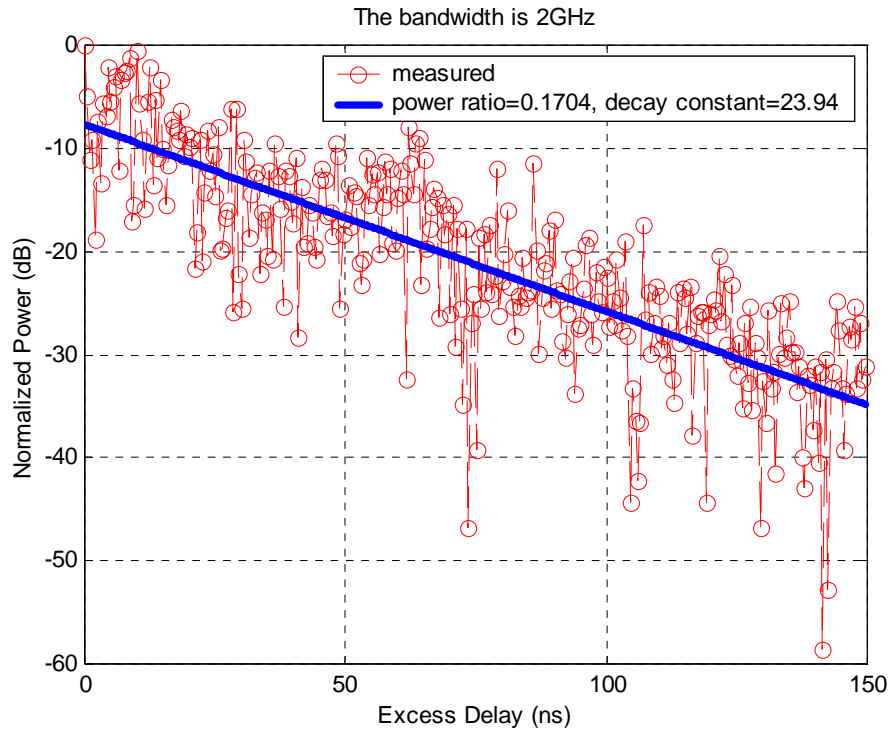
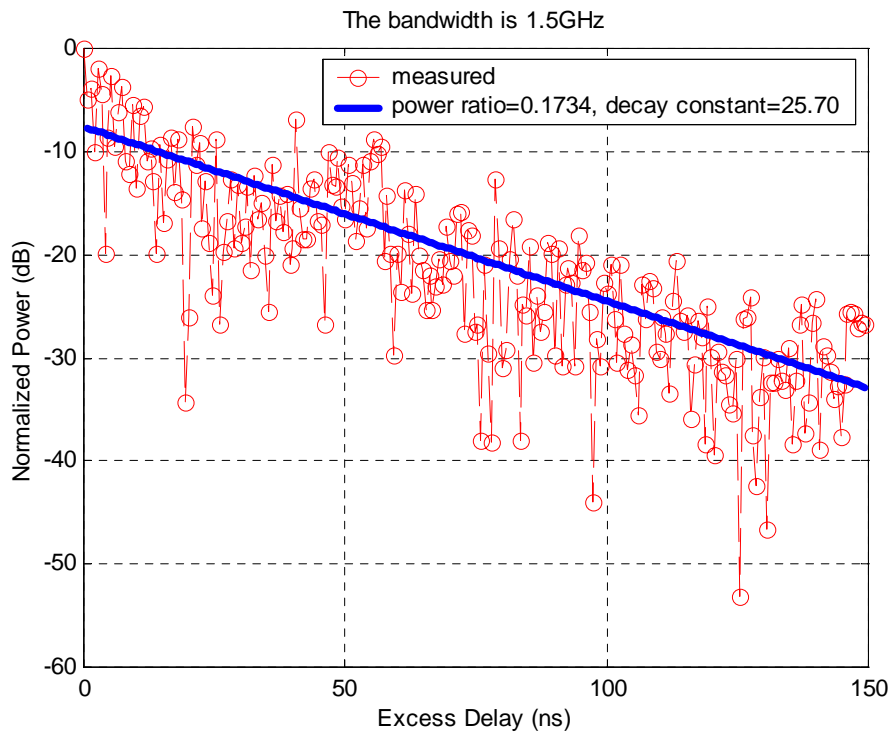


Figure 4-2 The normalized instantaneous PDP of subpoint no.124 in Room 901 for different bandwidth. (a) The bandwidth is 2 GHz with $r=0.016$, $\varepsilon =14.75(\text{ns})$; (b) The bandwidth is 1.5 GHz with $r=0.019$, $\varepsilon =17.62(\text{ns})$; (c) The bandwidth is 1 GHz with $r=0.021$, $\varepsilon =15.97(\text{ns})$; (d) The bandwidth is 500 MHz with $r=0.031$, $\varepsilon =19.74(\text{ns})$.



(a)



(b)

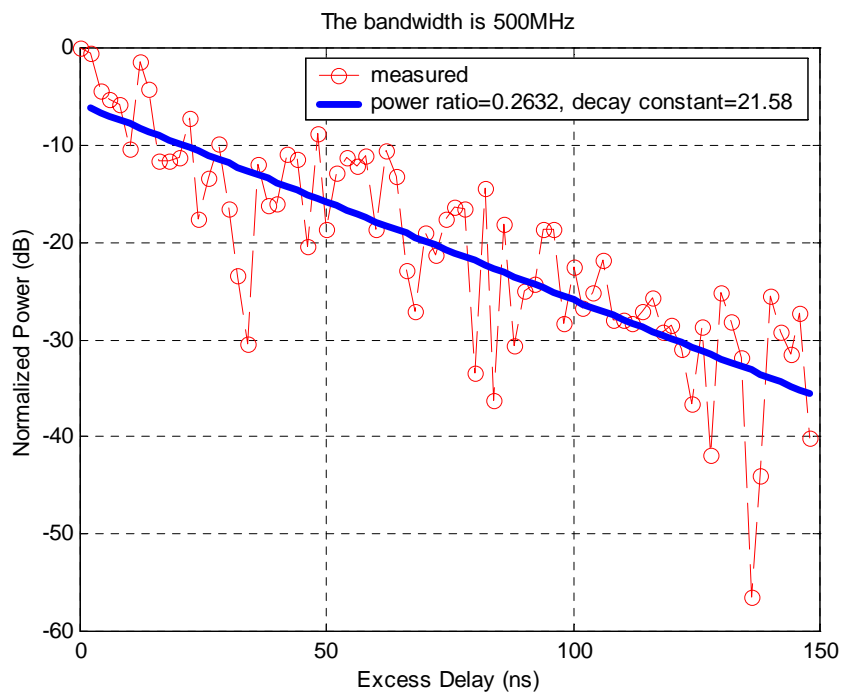
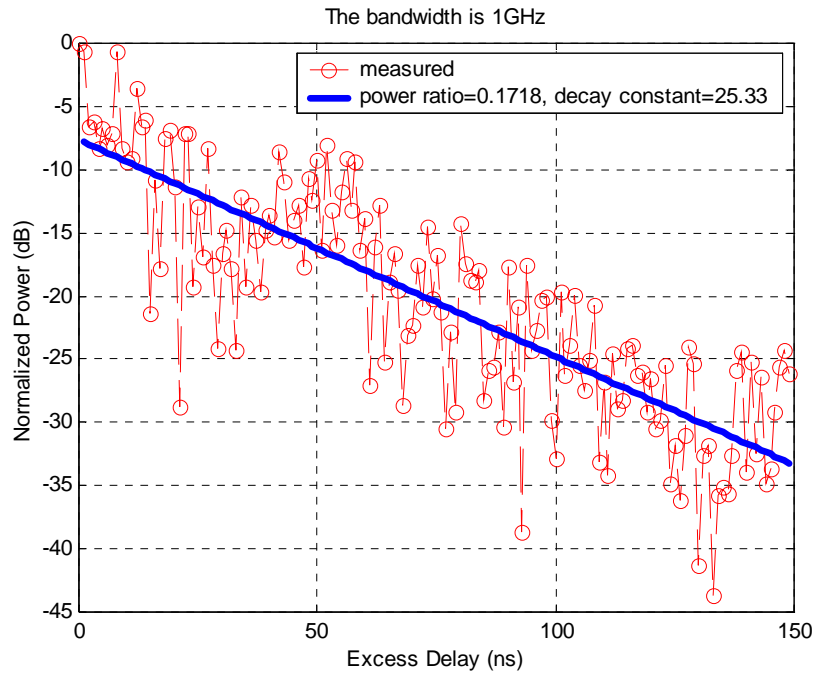
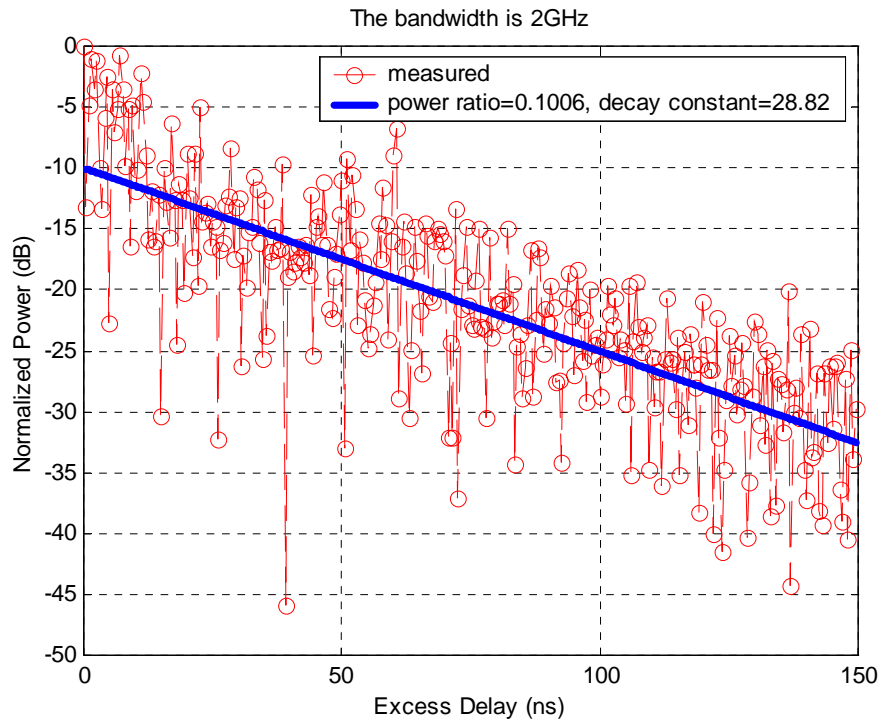
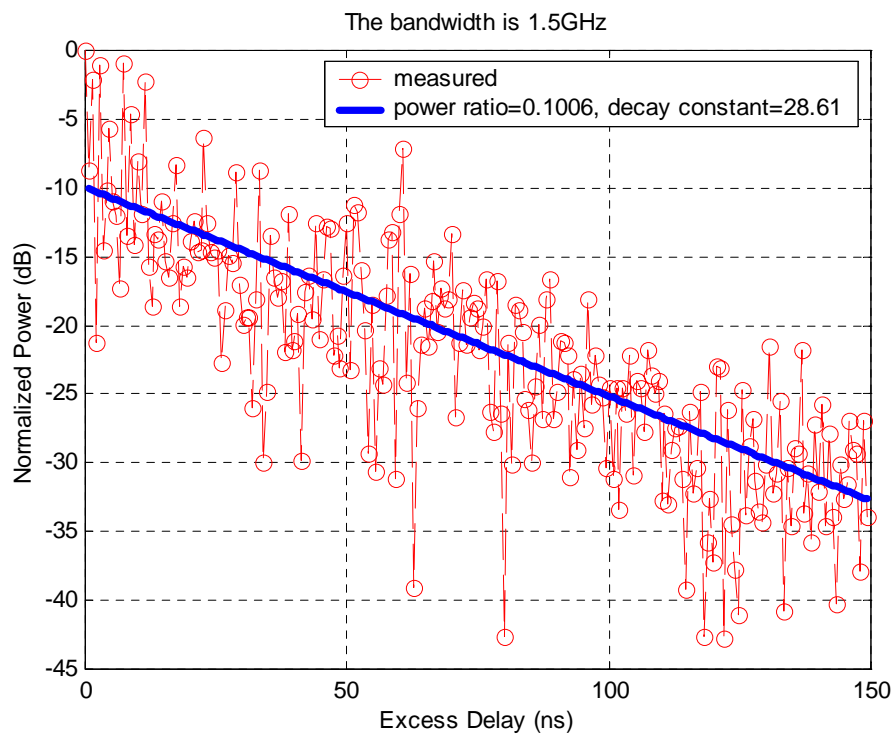


Figure 4-3 The normalized instantaneous PDP of subpoint no.2430 in Room 303 for different bandwidth. (a) The bandwidth is 2 GHz with $r=0.17$, $\varepsilon =23.94(\text{ns})$; (b) The bandwidth is 1.5 GHz with $r=0.173$, $\varepsilon =25.7(\text{ns})$; (c) The bandwidth is 1 GHz with $r=0.172$, $\varepsilon =25.33(\text{ns})$; (d) The bandwidth is 500 MHz with $r=0.263$, $\varepsilon =21.58(\text{ns})$.



(a)



(b)

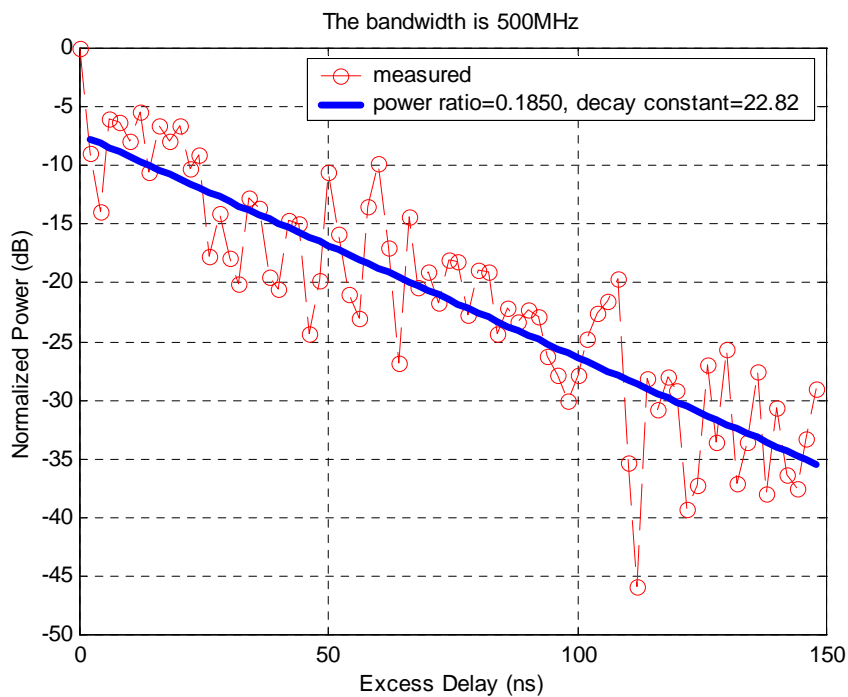
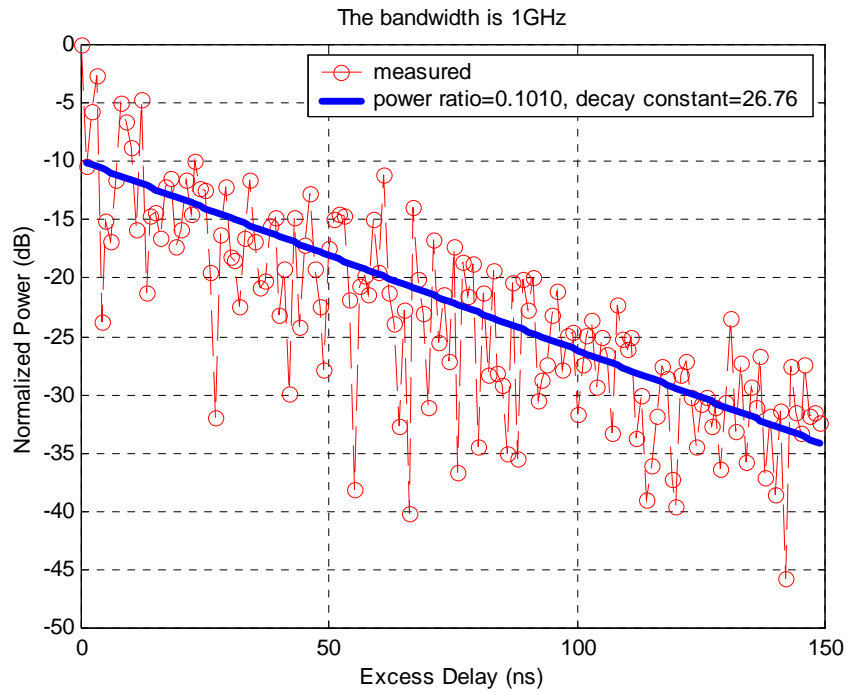
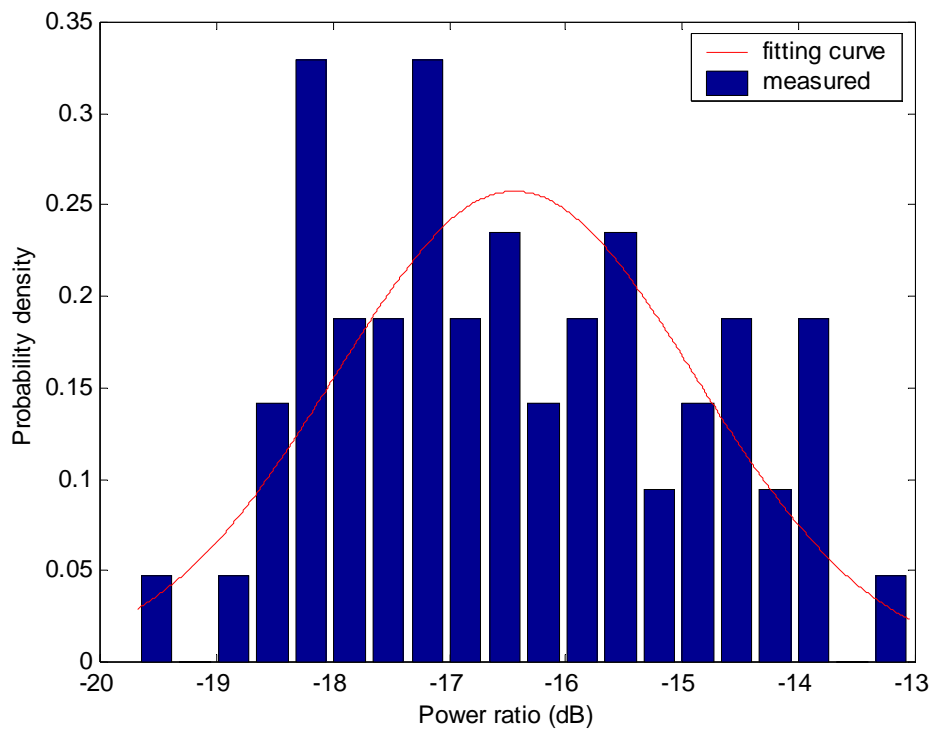
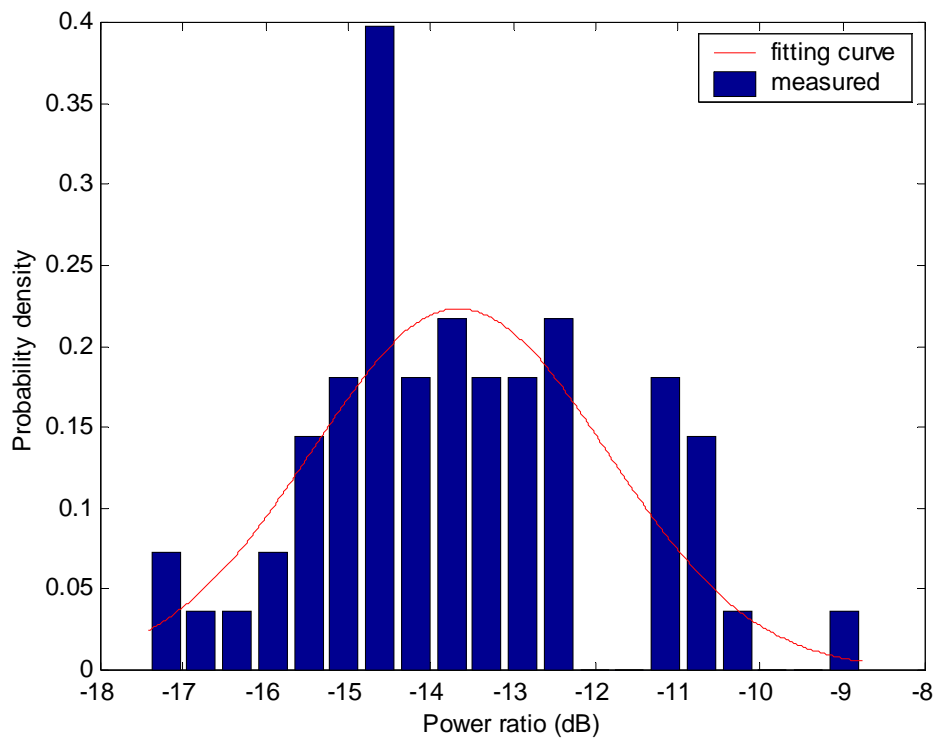


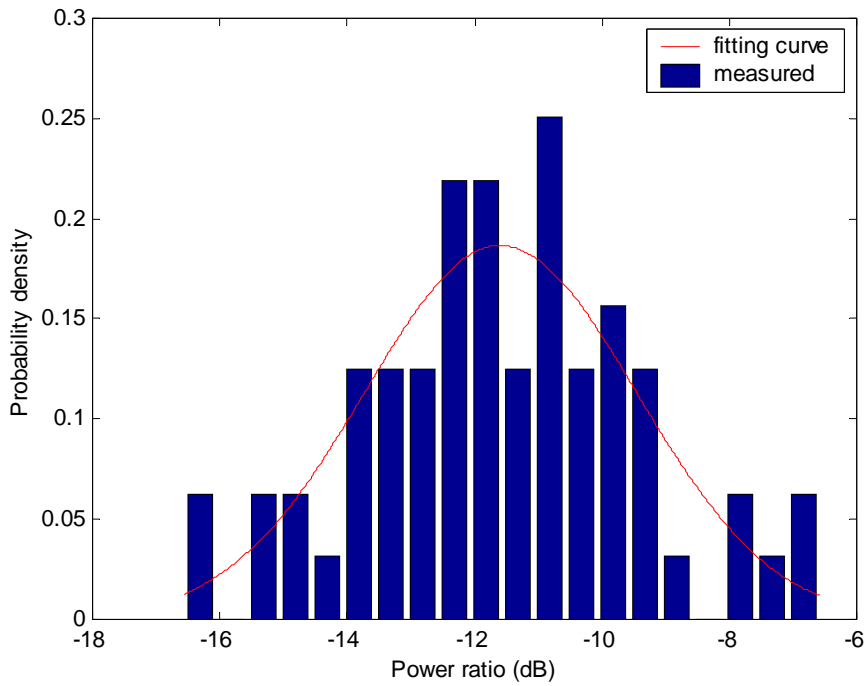
Figure 4-4 The normalized instantaneous PDP of subpoint no.2450 in Room 303 for different bandwidth. (a) The bandwidth is 2 GHz with $r=0.101$, $\varepsilon =28.82(\text{ns})$; (b) The bandwidth is 1.5 GHz with $r=0.101$, $\varepsilon =28.61(\text{ns})$; (c) The bandwidth is 1 GHz with $r=0.101$, $\varepsilon =26.76(\text{ns})$; (d) The bandwidth is 500 MHz with $r=0.185$, $\varepsilon =22.82(\text{ns})$.



(a)

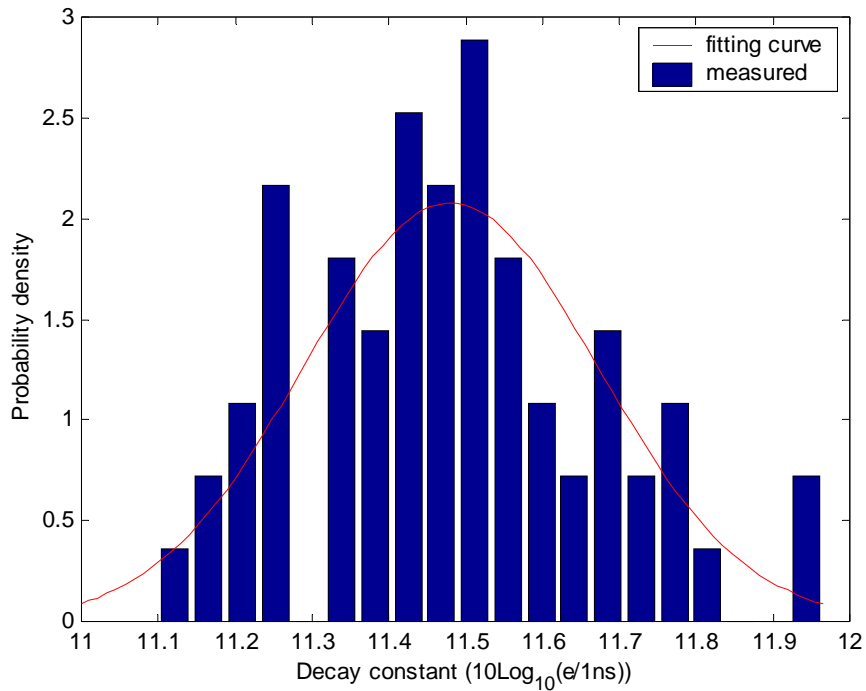


(b)

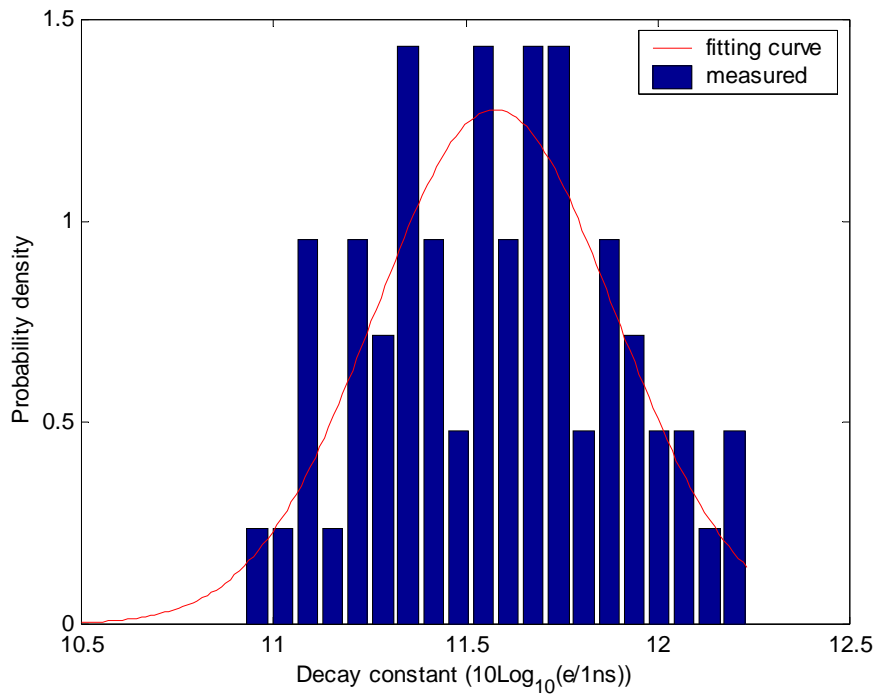


(c)

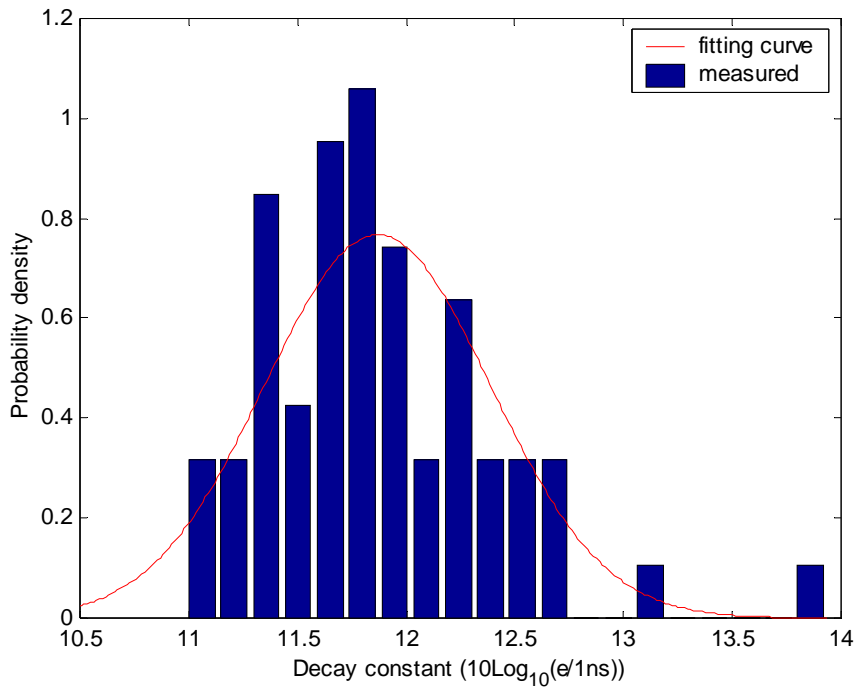
Figure 4-5 The histogram of the power ratio (in dB scale) can be fitted well by a normal distribution. (a) The bandwidth is 2 GHz with $\mu_r = -16.44$ dB and $\sigma_r = 1.55$ dB; (b) The bandwidth is 1 GHz with $\mu_r = -13.66$ dB and $\sigma_r = 1.78$ dB; (c) The bandwidth is 500 MHz with $\mu_r = -11.6$ dB and $\sigma_r = 2.13$ dB.



(a)



(b)



(c)

Figure 4-6 The histogram of the logarithmic decay constant can be fitted well by a normal distribution. (a)The bandwidth is 2 GHz with $\mu_{\epsilon} = 11.48$ dB and $\sigma_{\epsilon} = 0.19$ dB; (b)The bandwidth is 1 GHz with $\mu_{\epsilon} = 11.58$ dB and $\sigma_{\epsilon} = 0.31$ dB; (c) The bandwidth is 500 MHz with $\mu_{\epsilon} = 11.87$ dB and $\sigma_{\epsilon} = 0.52$ dB.

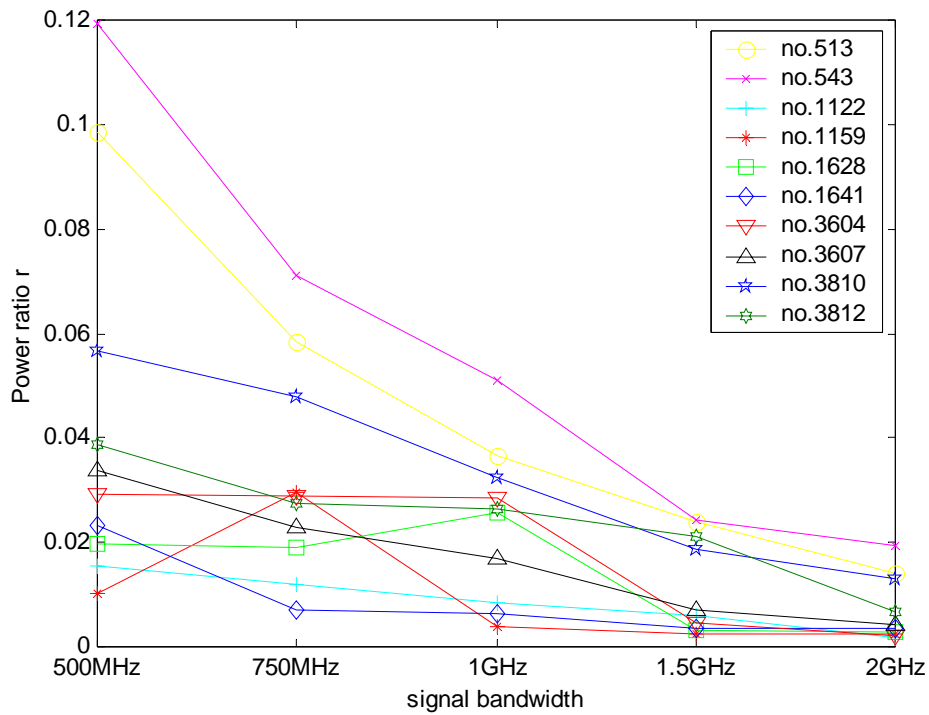


Figure 4-7. Power ratio r versus signal bandwidth at different measurement subpoints for the LOS 0-4m situation.

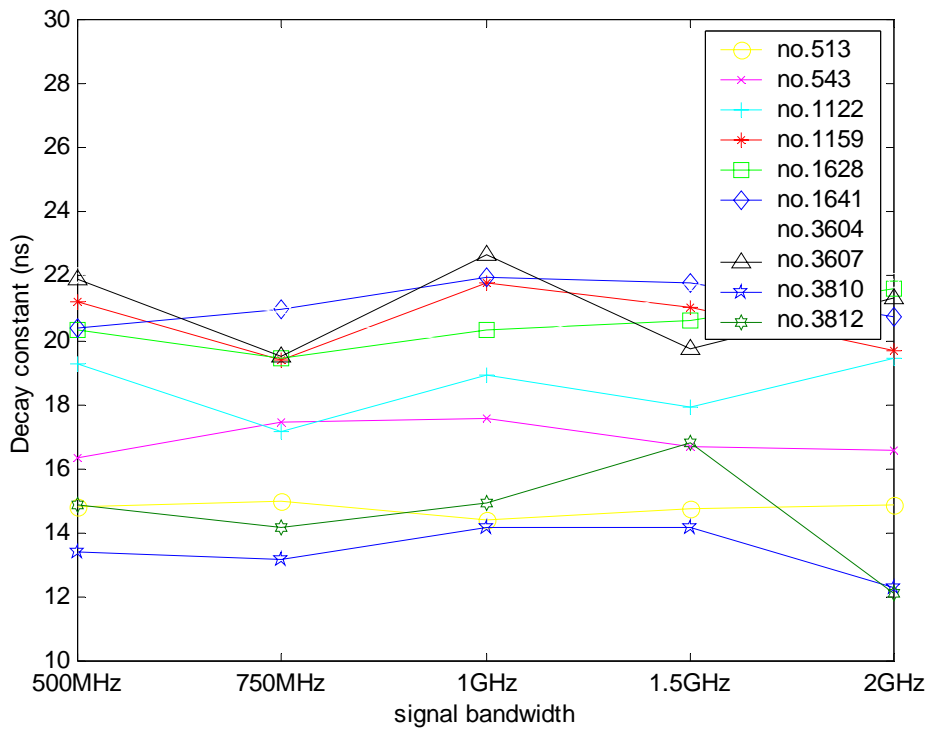


Figure 4-8. Decay constant ϵ versus signal bandwidth at different measurement subpoints for the LOS 0-4m situation.

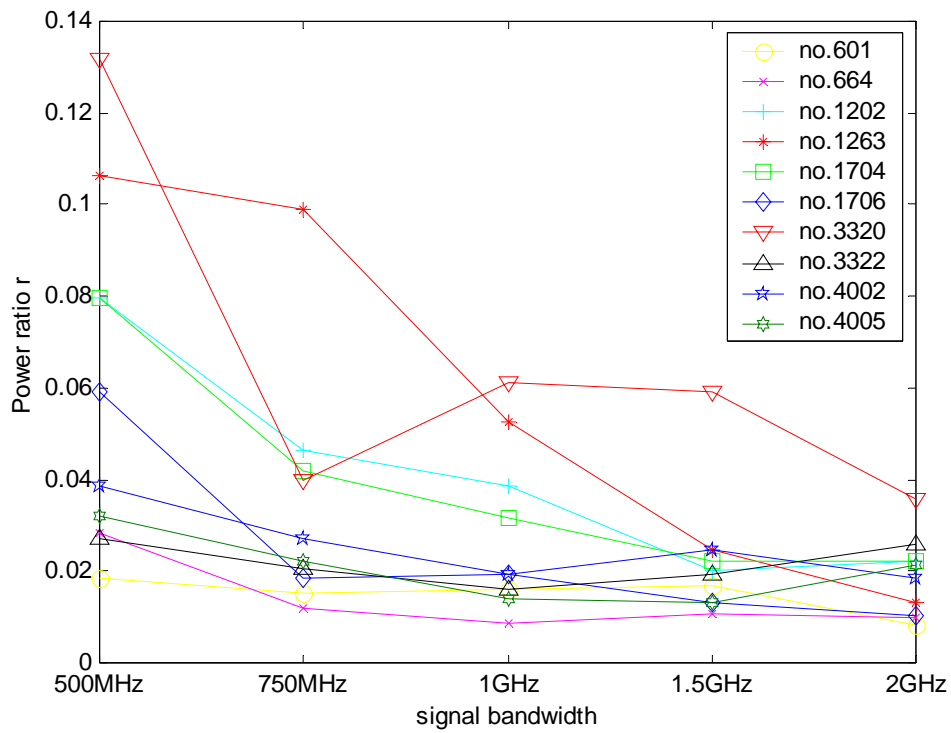


Figure 4-9. Power ratio r versus signal bandwidth at different measurement subpoints for the LOS 4-10m situation.

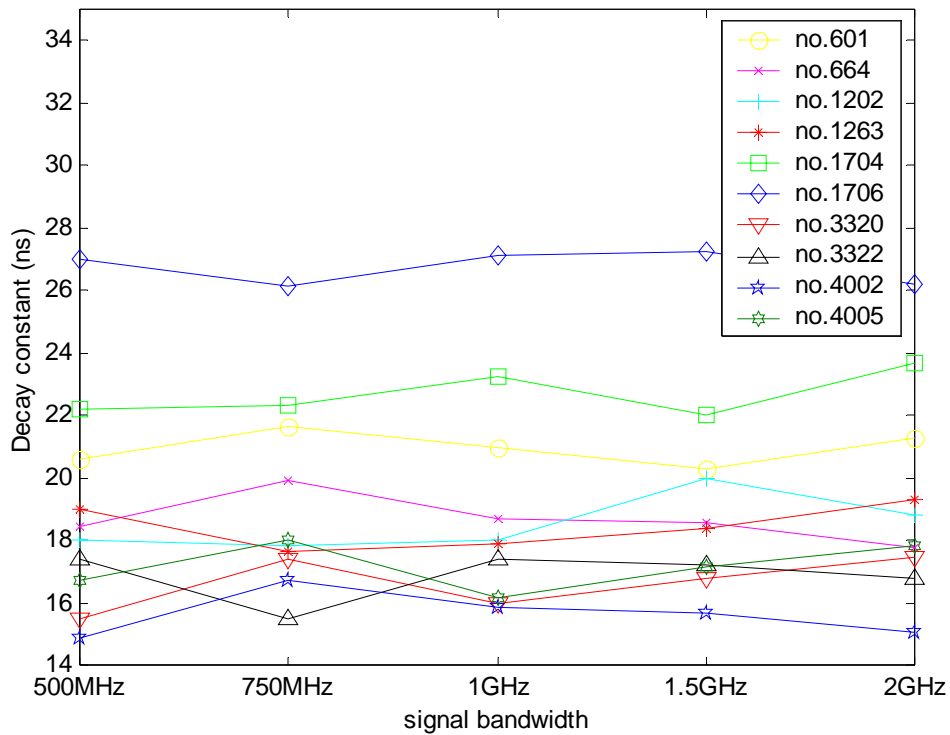


Figure 4-10. Decay constant ϵ versus signal bandwidth at different measurement subpoints for the LOS 4-10m situation.

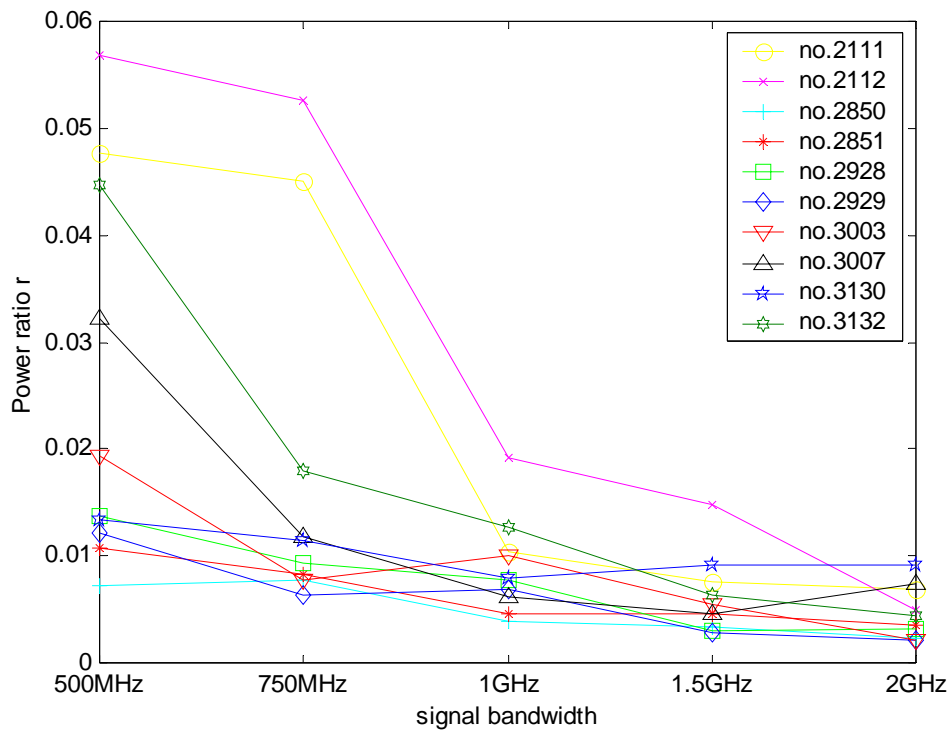


Figure 4-11. Power ratio r versus signal bandwidth at different measurement subpoints for the NLOS 0-4m situation.

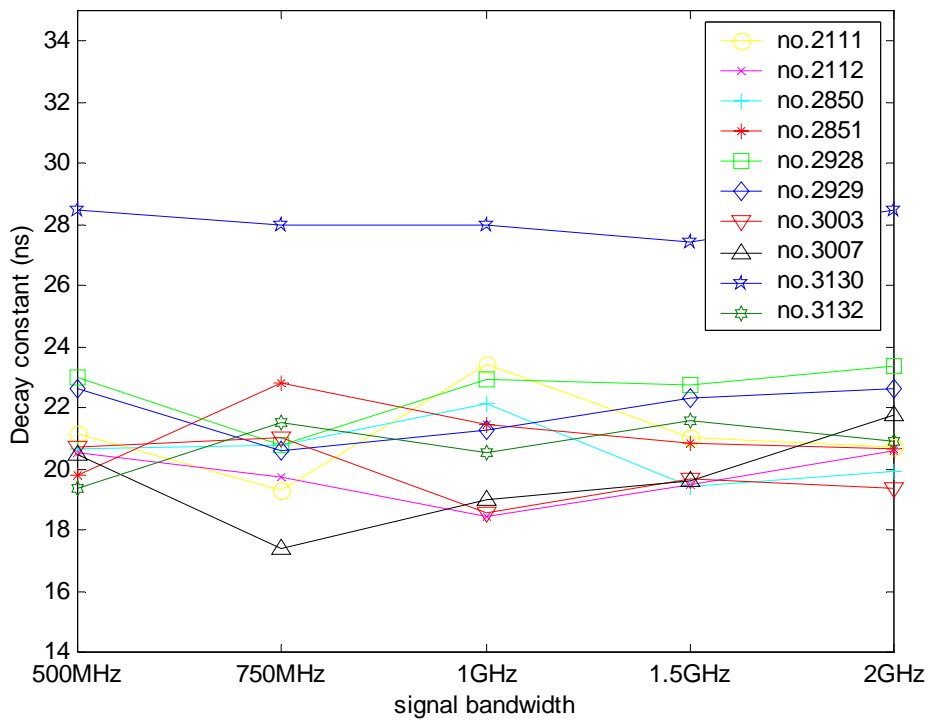


Figure 4-12. Decay constant ϵ versus signal bandwidth at different measurement subpoints for the NLOS 0-4m situation.

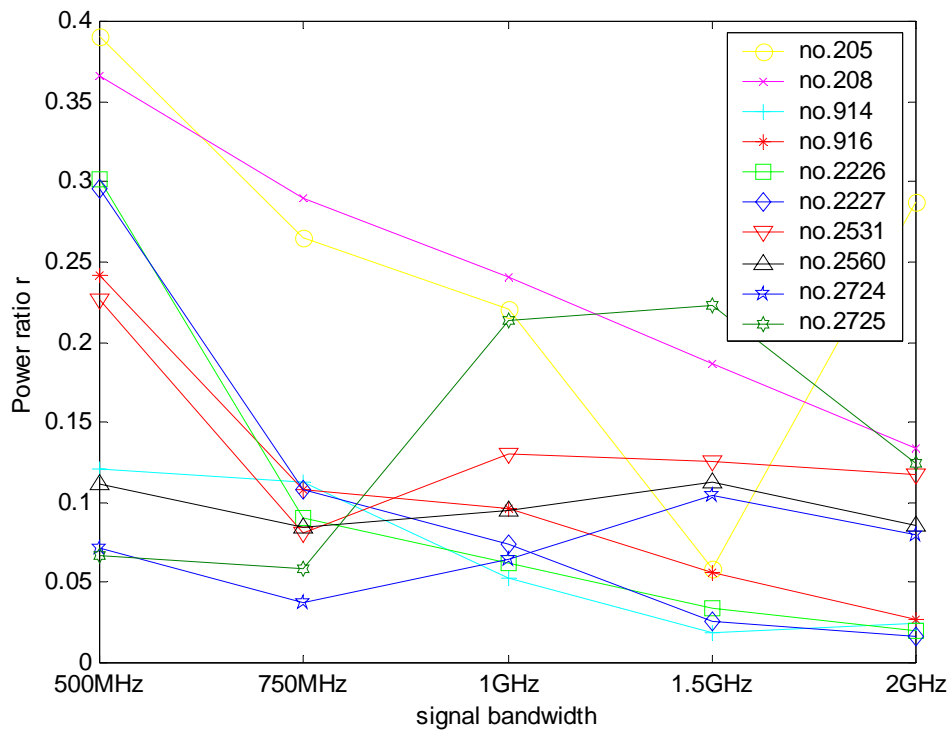


Figure 4-13. Power ratio r versus signal bandwidth at different measurement subpoints for the NLOS 4-20m situation.

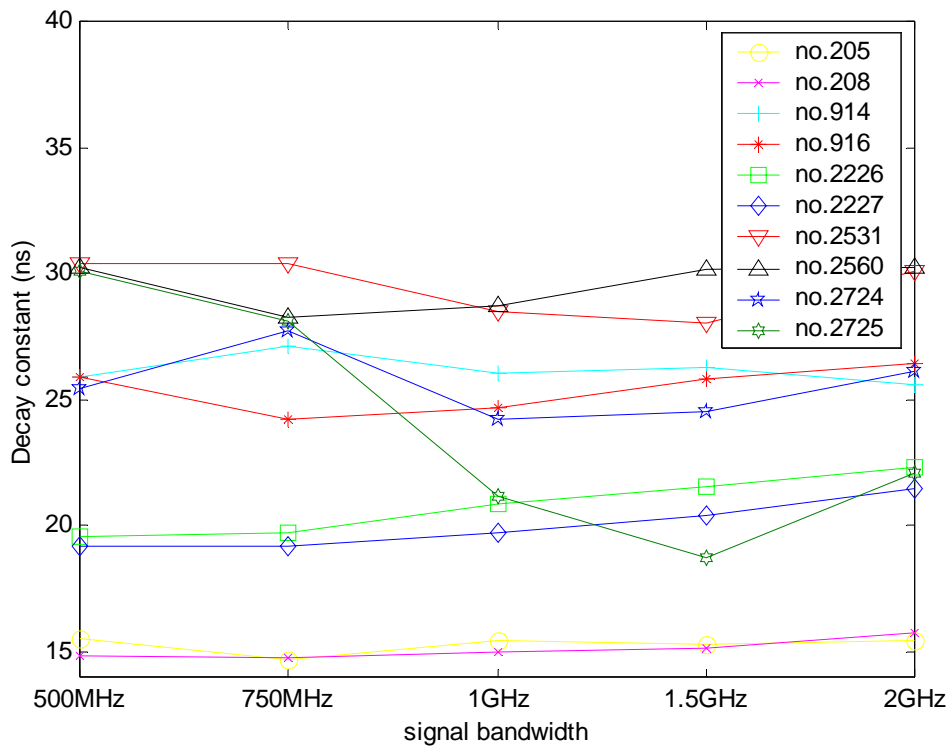
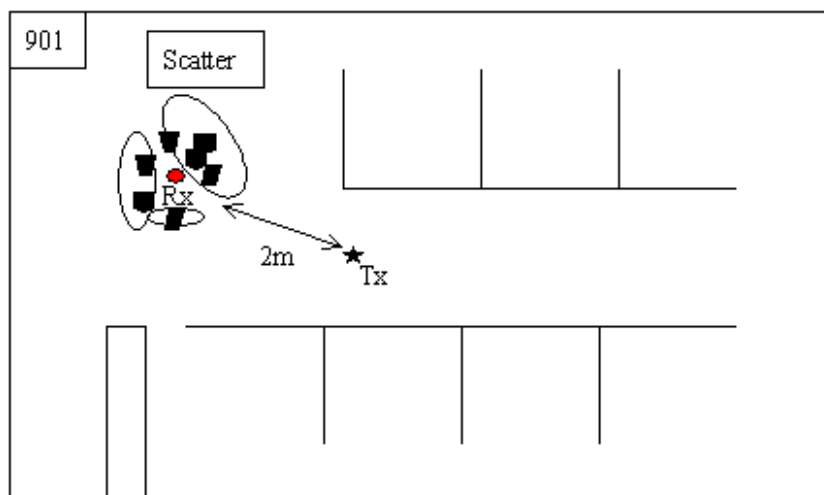
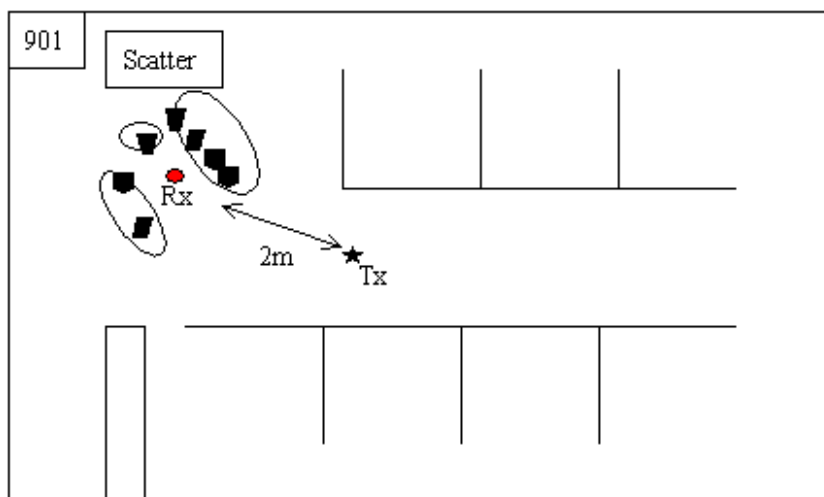


Figure 4-14. Decay constant ϵ versus signal bandwidth at different measurement subpoints for the NLOS 4-20m situation.

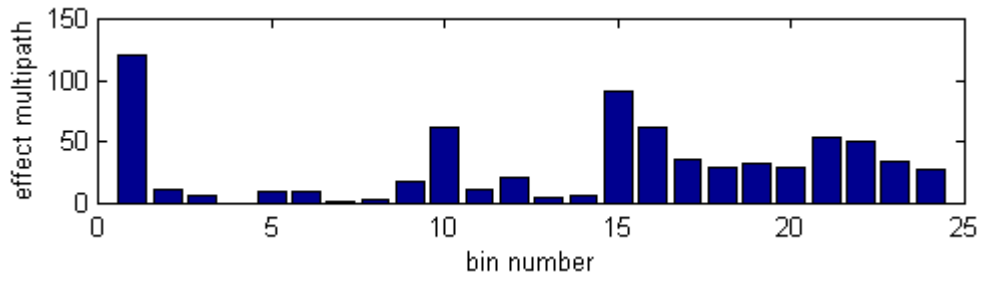


(a)

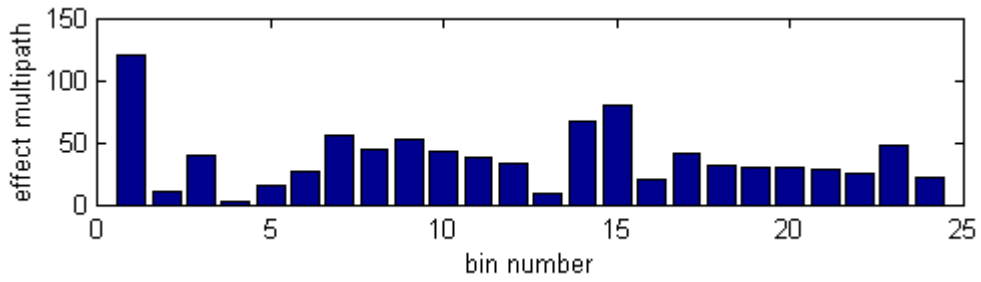


(b)

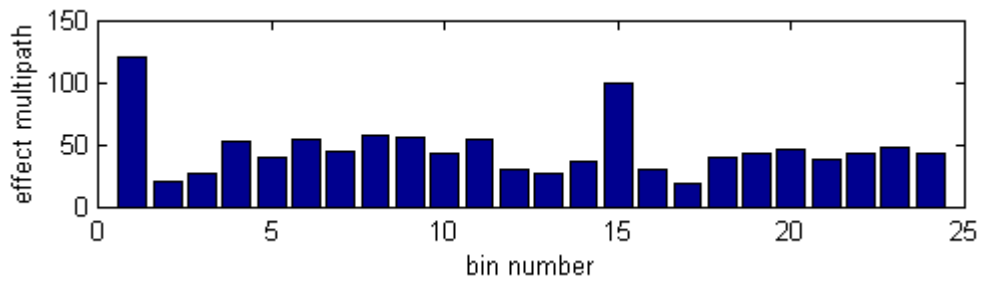
Figure 4-15 (a) There are near local scatterers distribution around the receiver within a radius of 20cm in a laboratory. (b) There is slightly far local scatterers distribution around the receiver within a radius of 45cm in the laboratory.



(a)

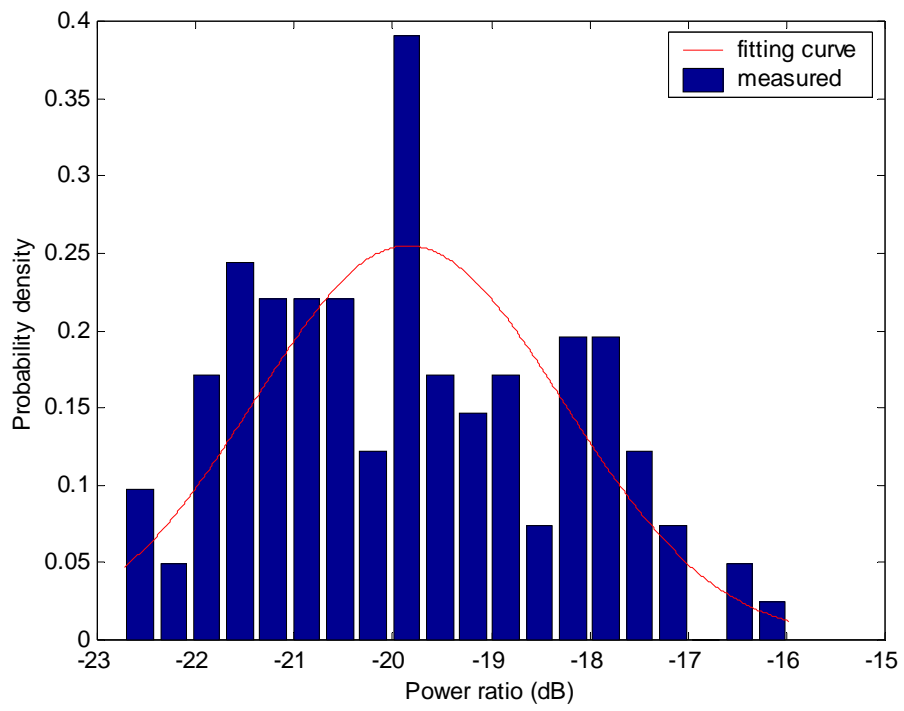


(b)

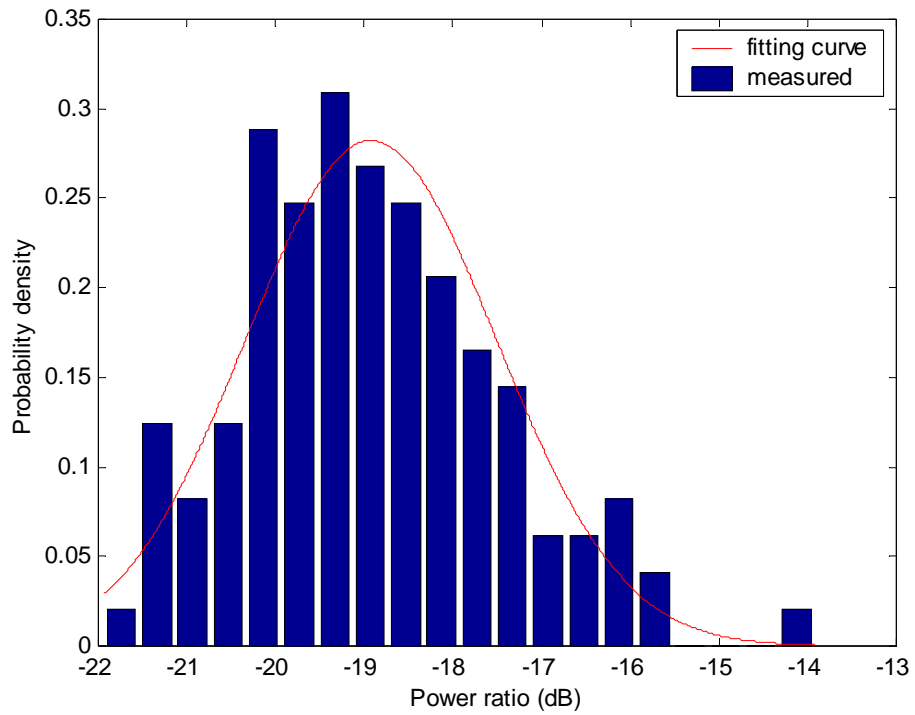


(c)

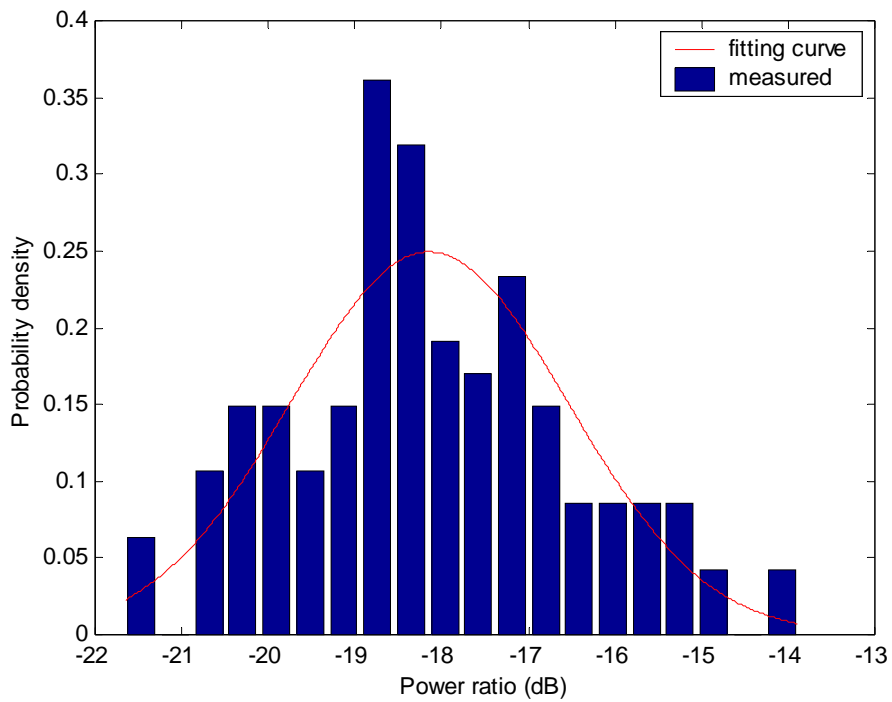
Figure 4-16 The effect multipath number versus the delay bin for different local scatterer distribution around the receiver. (a) There is no local scatterer distribution around the receiver; (b) There is farer scatterer distribution around the receiver; (c) There is nearer scatterer distribution around the receiver.



(a)

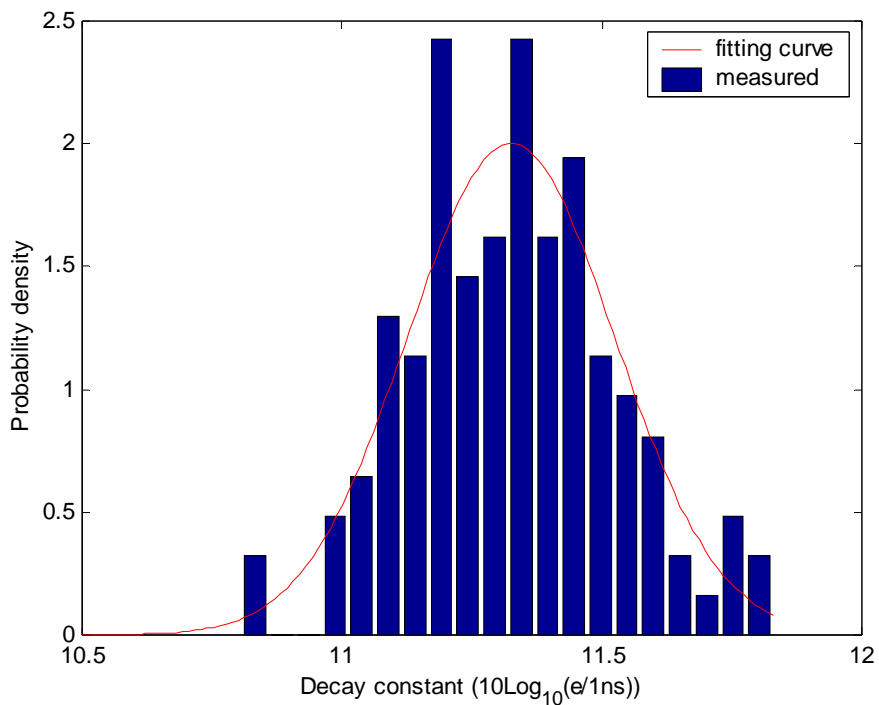


(b)

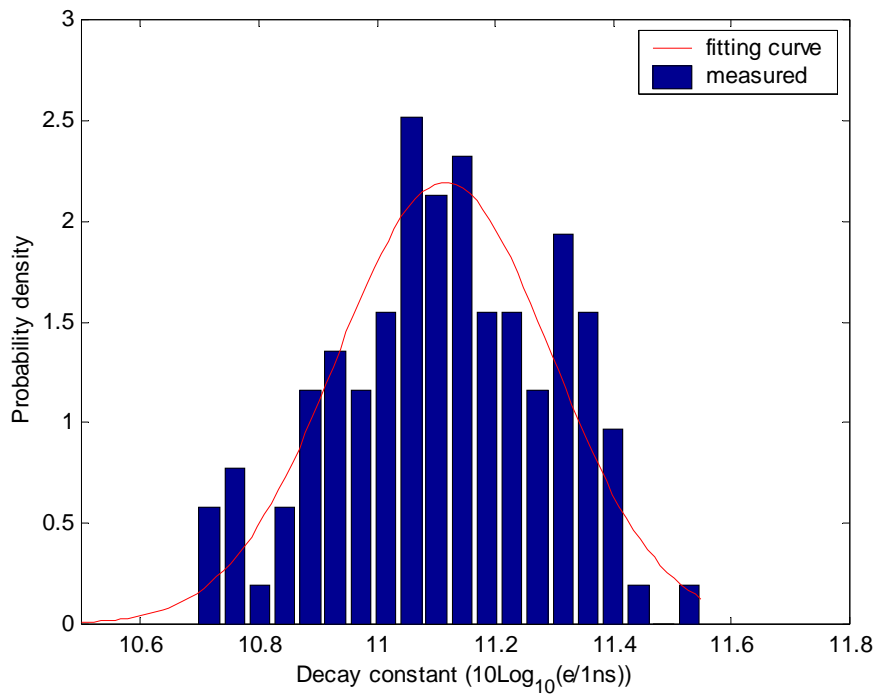


(c)

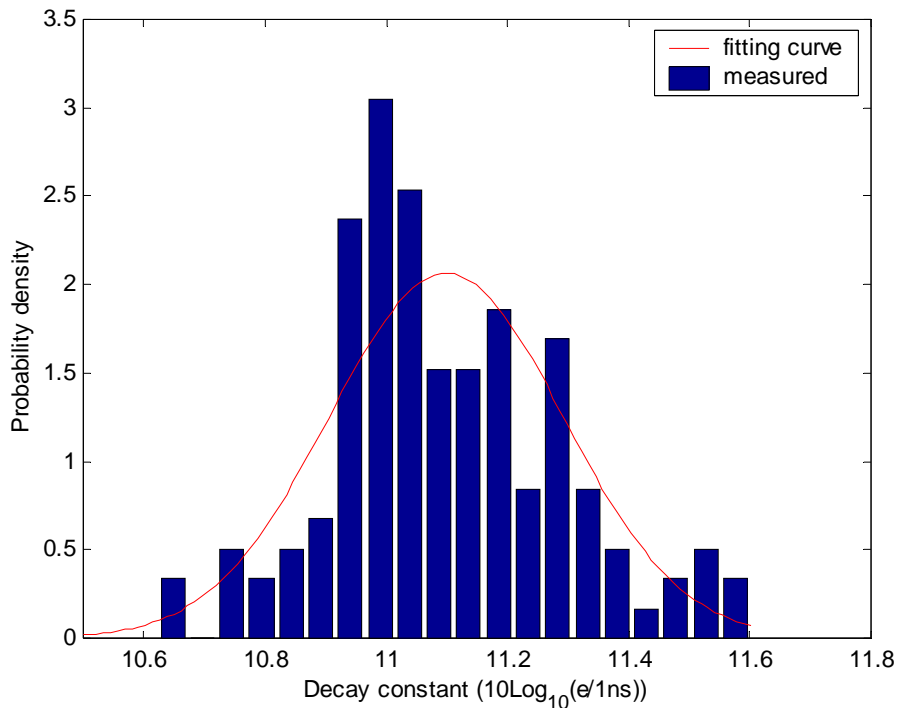
Figure 4-17 The power ratio histograms of different local scatterers distribution around the receiver conditions. (a) $\mu_r = -19.84$ and $\sigma_r = 1.57$ of no local scatterers situation; (b) $\mu_r = -18.92$ and $\sigma_r = 1.414$ of farer local scatterers situation; (c) $\mu_r = -18.15$ and $\sigma_r = 1.6$ of nearer local scatterer situation.



(a)



(b)



(c)

Figure 4-18 The decay constant histograms of different local scatterers distribution around the receiver conditions. (a) $\mu_{\epsilon} = 11.33$ and $\sigma_{\epsilon} = 0.2$ of no local scatterer situation; (b) $\mu_{\epsilon} = 11.11$ and $\sigma_{\epsilon} = 0.18$ of farer local scatterers situation; (c) $\mu_{\epsilon} = 11.09$ and $\sigma_{\epsilon} = 0.19$ of nearer local scatterers situation.

4.2 Effect of Bandwidth and Propagation on Averaged Power Delay Profile (Not including local scattering effects)

At each measurement point PDPs of the 64 subpoints were sampled and each PDP was normalized by its peak power. Then, these 64 normalized PDPs were collected and averaged to yield an averaged PDP for the measurement point. With the STDL model, the averaged PDP can also be described with power ratio r and decay constant ε .

Figures 4-19, and 4-20 illustrate the normalized averaged PDPs of point no.24 and no.15, respectively. The first point is in Room 302 of NLOS situation and the other point is in Room 203 of LOS situation.

As shown in the figures, the normalized power in LOS environment decreases faster than that in NLOS environment, which is reasonable since profiles measured in the Room 203 contain less multipath components.

In figure 4-21, the power ratio of each measured point is drawn as a function of Tx-Rx distance both LOS and NLOS conditions. When propagation distance is increased, there is more multipath fall within the second bin. Therefore, the power ratio r is increased when propagation is increased. In figure 4-22, the decay constant of each measured point is drawn as a function of Tx-Rx distance both LOS and NLOS conditions. It seems that the decay constant in the both conditions is independent of the Tx-Rx distance.

The power ratio and decay constant can be calculated for each measured point. With the result of total 42 measured points, the histogram of the power ratio can be fitted well by a lognormal distribution (in linear scale) or a normal distribution (in dB scale) with mean $\mu_r = -13.81$ dB and standard deviation $\sigma_r = 4.25$ dB, and the fitting curve is shown in figure 4-23. In the figure 4-24, it is also found that the histogram of

the logarithmic decay constant can be described by a normal distribution with $\mu_\epsilon = 12.07$ dB and $\sigma_\epsilon = 1.45$ dB.

Figure 4-25 illustrates the power ratio versus signal bandwidth for the LOS 0-4m situation. It is found that the power ratio r is increased when the bandwidth is decreased. Figure 4-26 illustrates the decay constant versus signal bandwidth for the LOS 0-4m situation. It is found that the decay constant is only slightly dependent on the signal bandwidth.



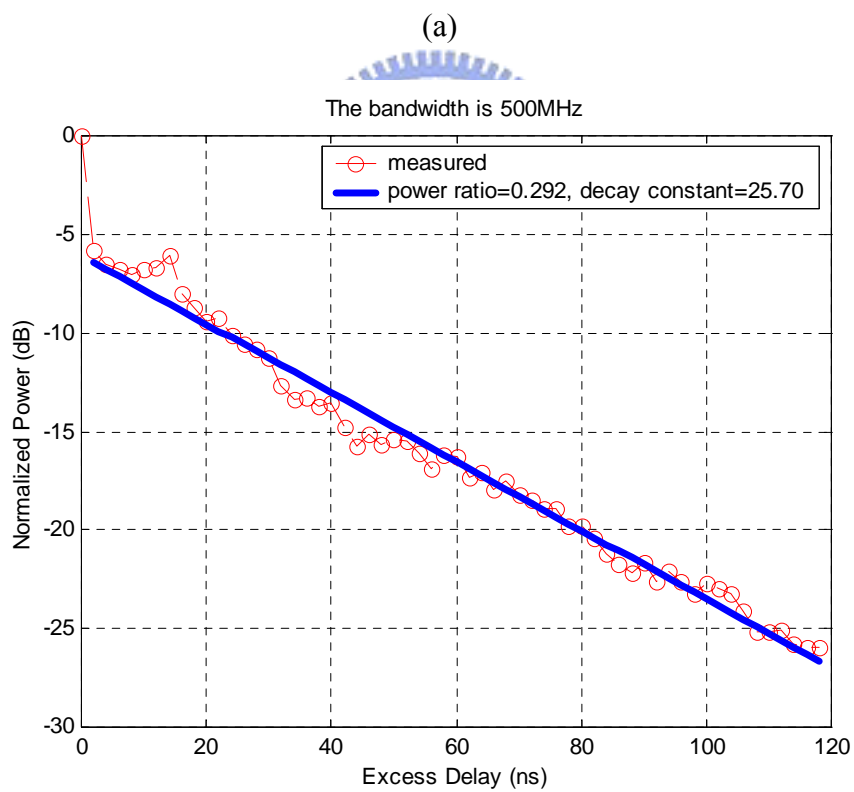
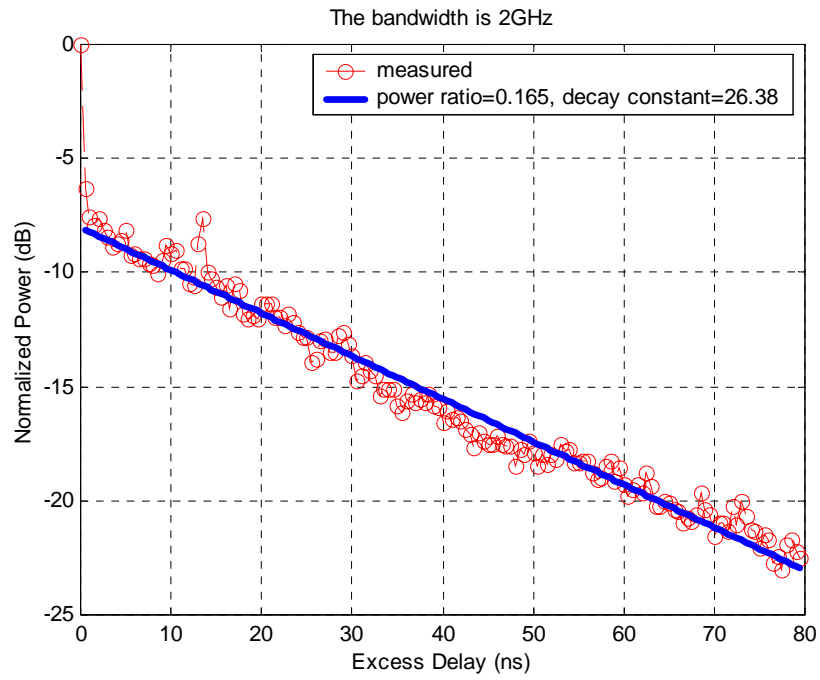


Figure 4-19 The normalized average PDP of point no.24 in Room 302 for different bandwidth. (a) The bandwidth is 2 GHz with $r=0.165$, $\epsilon =26.38(\text{ns})$; (b) The bandwidth is 500 MHz with $r=0.292$, $\epsilon =25.7(\text{ns})$.

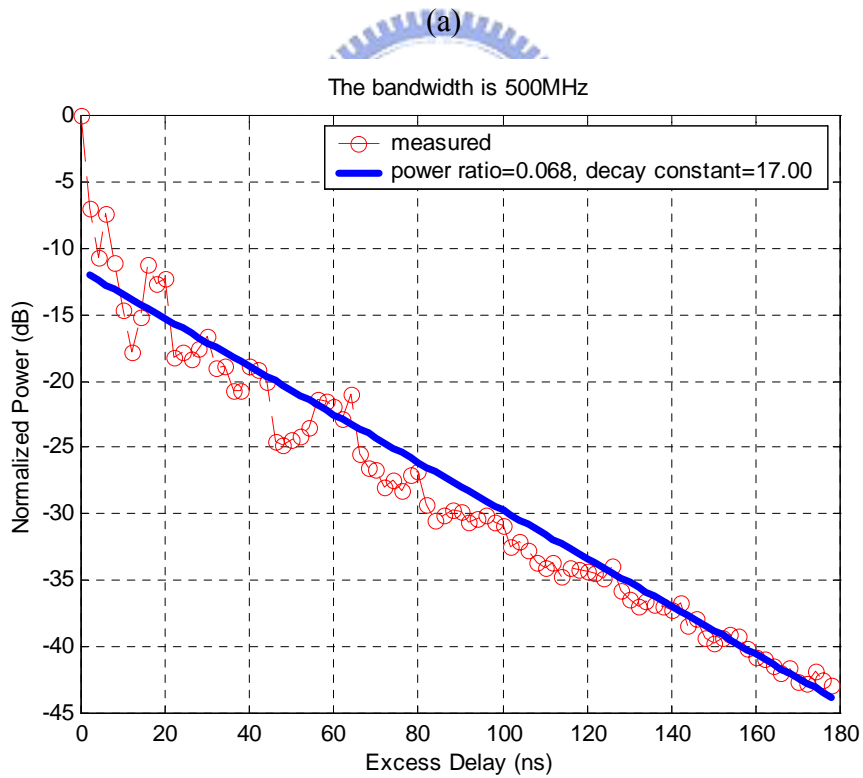
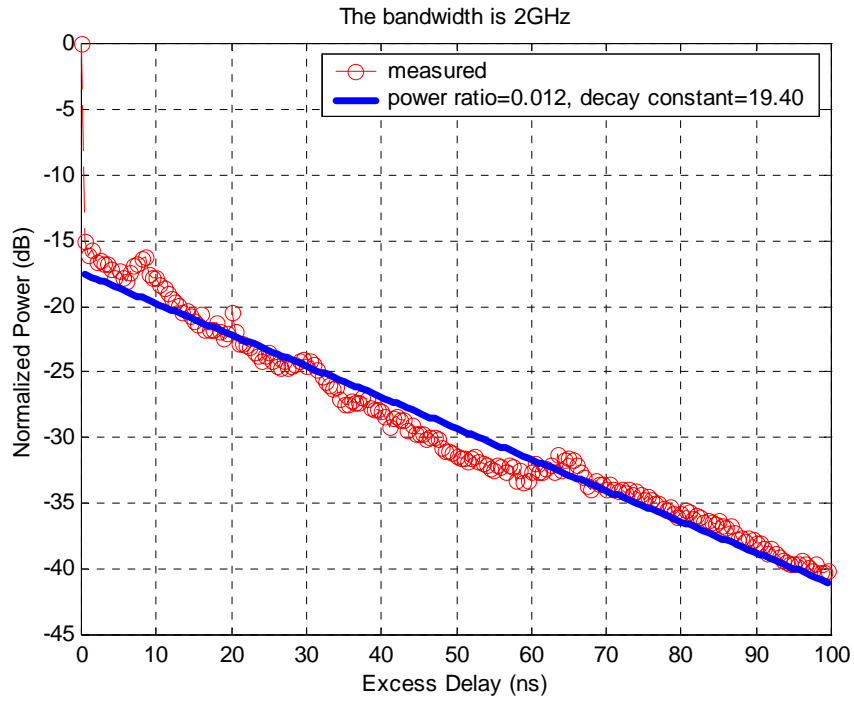


Figure 4-20 The normalized average PDP of point no.15 in Room 203 for different bandwidth. (a) The bandwidth is 2 GHz with $r=0.012$, $\varepsilon = 19.4(\text{ns})$; (b) The bandwidth is 500 MHz with $r=0.068$, $\varepsilon = 17(\text{ns})$.

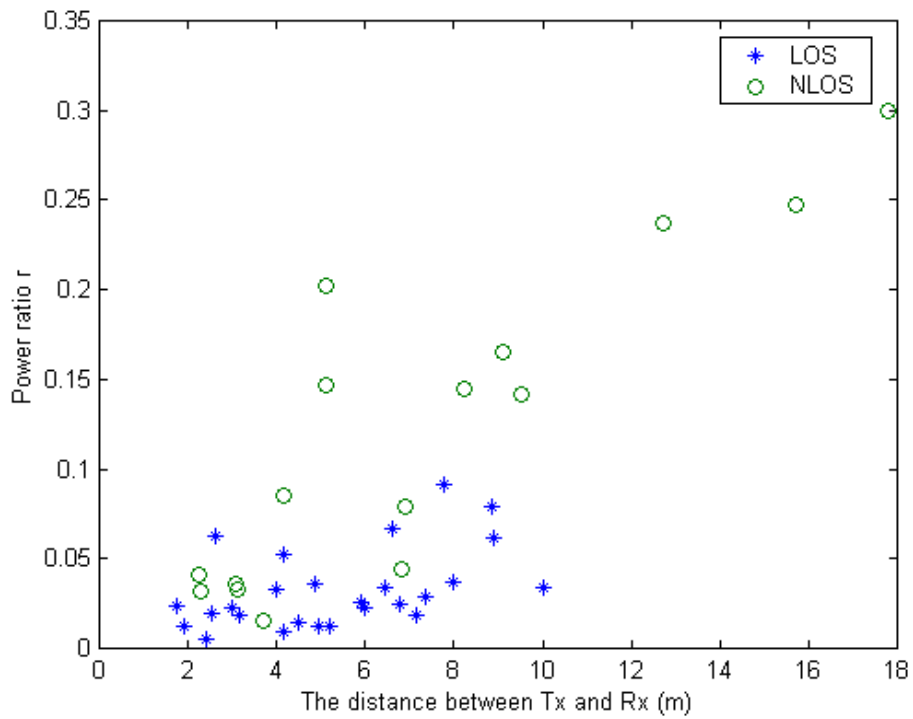
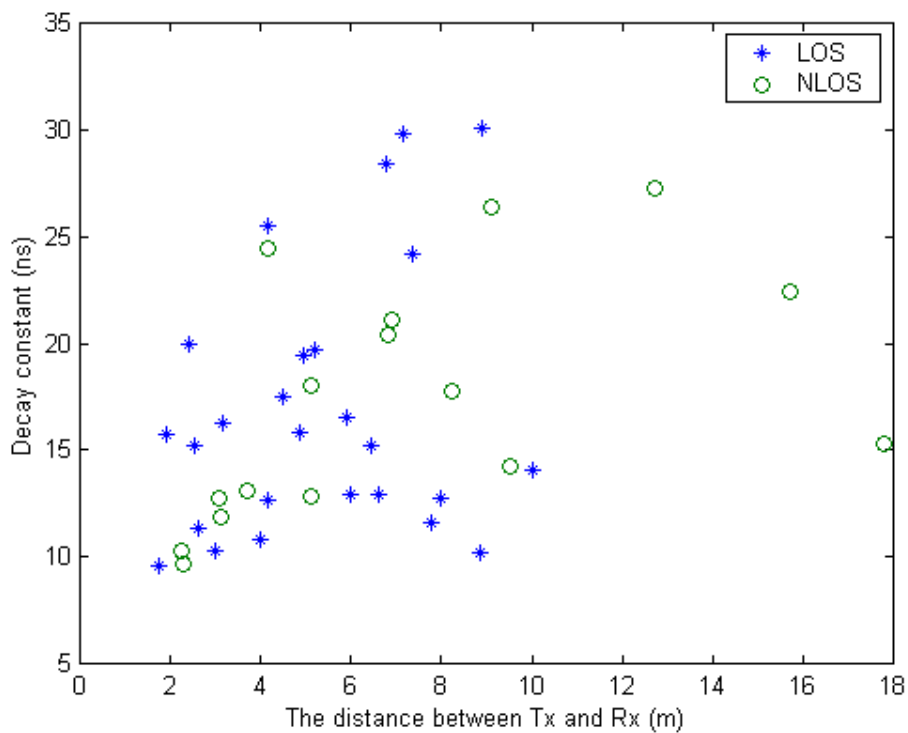


Figure 4-21 The power ratio versus the distance between Tx and Rx.



(b)

Figure 4-22 The decay constant versus the distance between Tx and Rx.

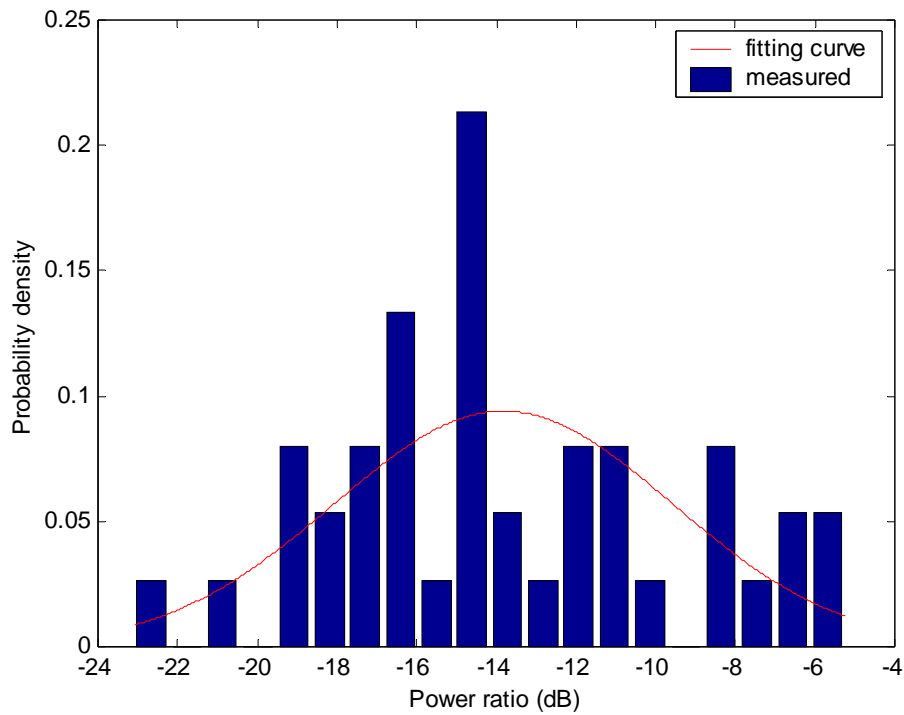


Figure 4-23 The histogram of the power ratio (in dB scale) can be fitted well by a normal distribution with $\mu_{\tau}=-13.81$ dB and $\sigma_{\tau}=4.25$ dB.

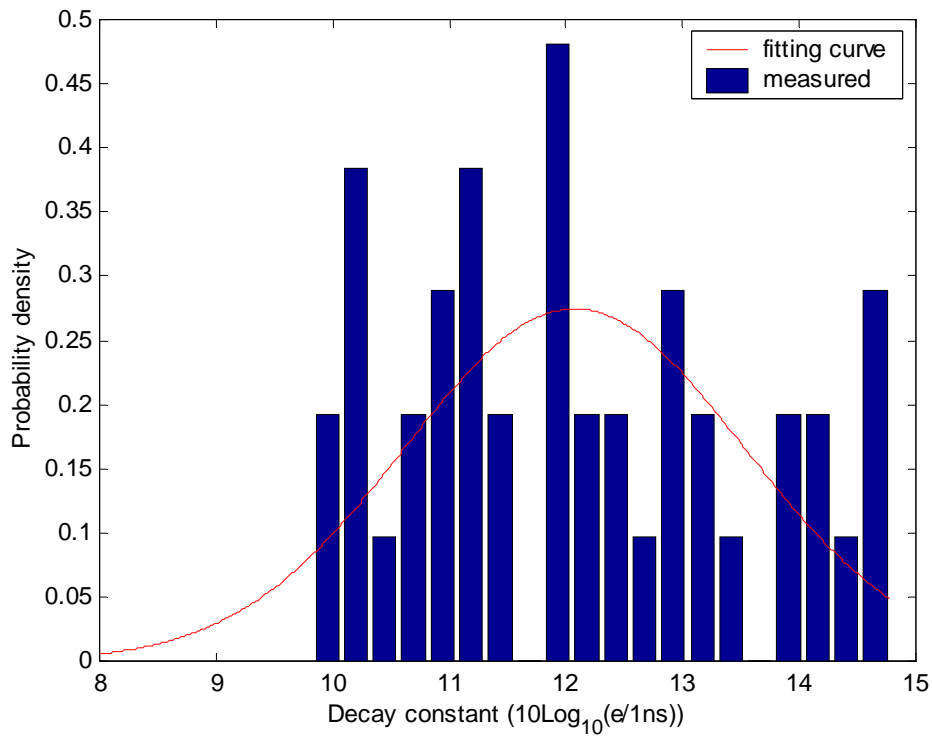


Figure 4-24 The histogram of the logarithmic decay constant can be fitted well by a normal distribution with $\mu_{\epsilon}=12.07$ dB and $\sigma_{\epsilon}=1.45$ dB.

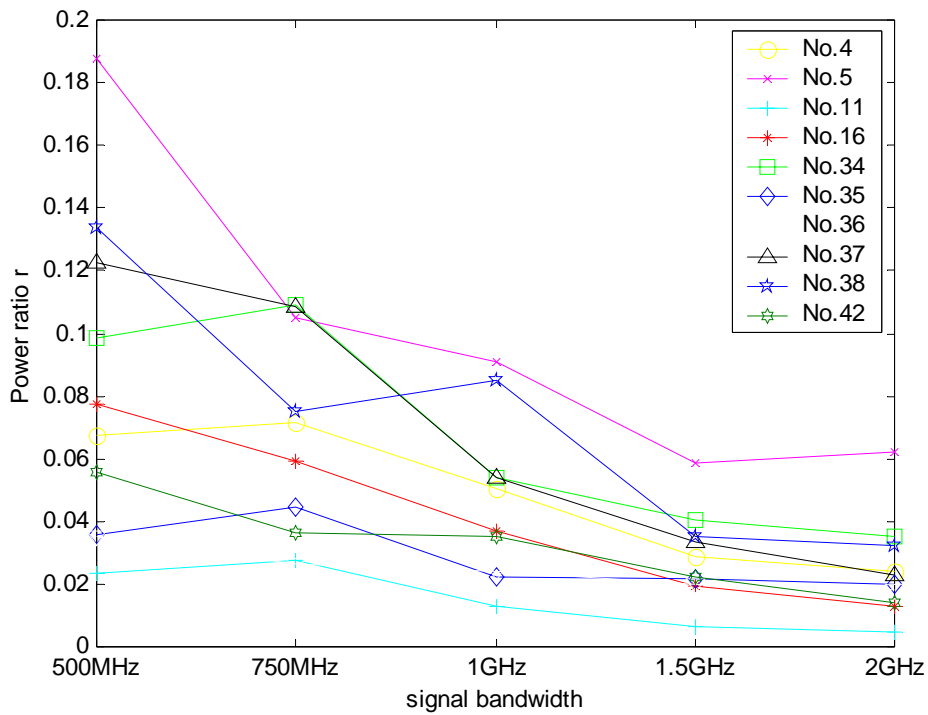


Figure 4-25. Power ratio r versus signal bandwidth at different measurement points for the LOS 0-4m situation.

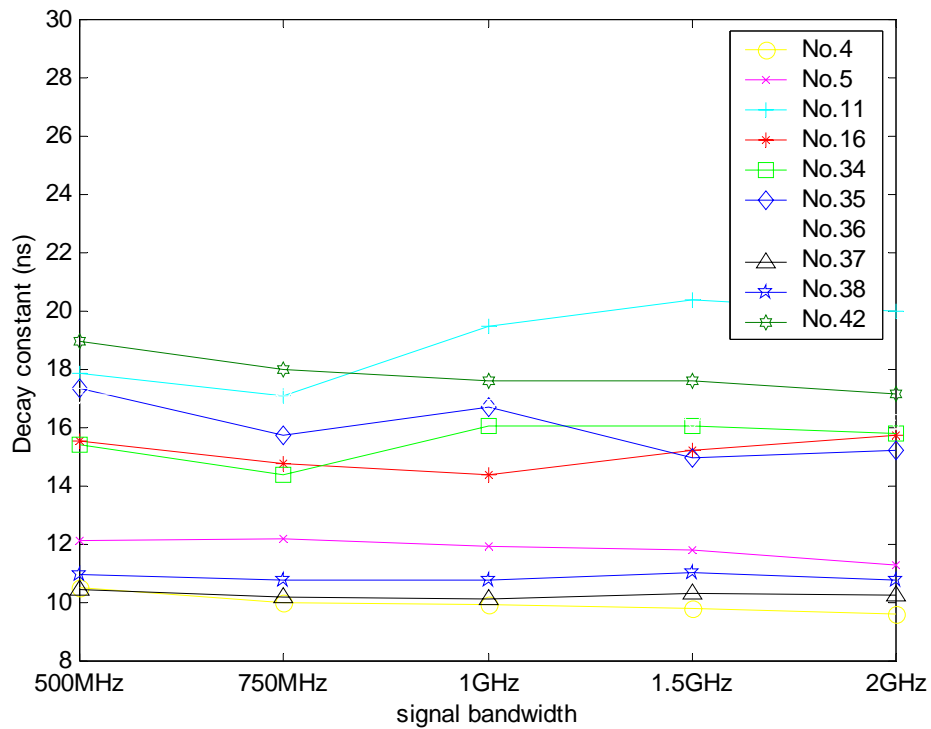


Figure 4-26. Decay constant ϵ versus signal bandwidth at different measurement points for the LOS 0-4m situation.

4.3 Effect of Signal Bandwidth on Amplitude fading

For multipath propagation of narrowband signal, there is a large number of MPCs in each delay bin and the complex received amplitude has a complex Gaussian distribution, which results in a Rayleigh or Rician distribution of the amplitudes. Therefore, it is usually assumed that the envelope of the first received bin, which may have direct path, follows a Rician or Nakagami distribution and the envelope of the later bins are assumed to have Rayleigh statistics [6]. However, in UWB propagation each resolved MPC is due to smaller number of scatter wave, and the amplitude distribution in later delay bin may differ markedly from the Rayleigh distribution. This phenomenon has been observed in figure 4-27(a) and (b) where the Nakagami distribution can fit better for the amplitude pdf of the 38th bin's and the 65th bin's, respectively. Here, the amplitude statistics of the first arrived bin for each measured point has been fitted by using a Rician distribution. Some examples are shown in Figures 4-28(a), (b), (c) and (d) for measured point nos. 2, 16, 21, and 41, respectively. It is found that the Rician distribution yields good fitting result.

In figure 4-29, the Rician factor versus signal bandwidth is shown. It is observed that the Rician factor is decreased as the signal bandwidth increases. It is true for the LOS condition such as the measured point nos. 4, 5, 16, 34, 35, 36, 37, 38 and 42. Similar result is observed for situations of LOS 4-10 m.

However, for the NLOS condition, the Rician factor is increased as the signal bandwidth increases such as the measured point nos. 21, 28, 29, 30, 31 and 32, which is shown in figure 4-30. It is because that in the NLOS 0-4m condition, the numbers of scattered multipath received at the first bin is decreased as the signal bandwidth increases, i.e., the timewidth of the bin decreased. Similar results are observed in the NLOS 4-20 m situation.

In figure 4-33, the Rician factor of each measured point is plotted as a function of Tx-Rx distance both LOS and NLOS conditions. With the existence of direct path, the Rician factor in LOS condition is larger than that of the NLOS condition. It seems that the Rician factor in the both conditions is independent of the Tx-Rx distance.



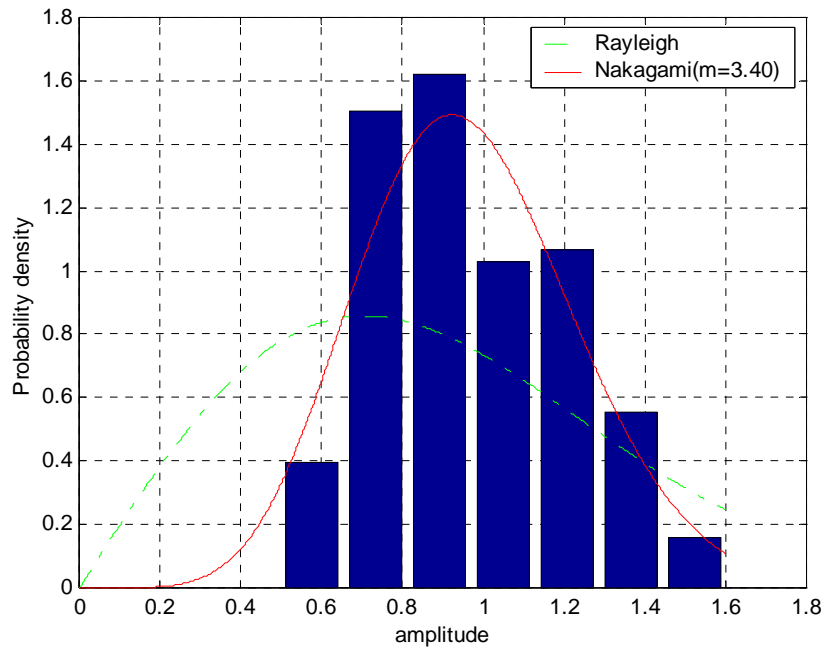


Figure 4-27(a) PDF of measured and fitted signal amplitudes of the 38th bin in Room 303 for NLOS environment. The bandwidth is 2GHz.

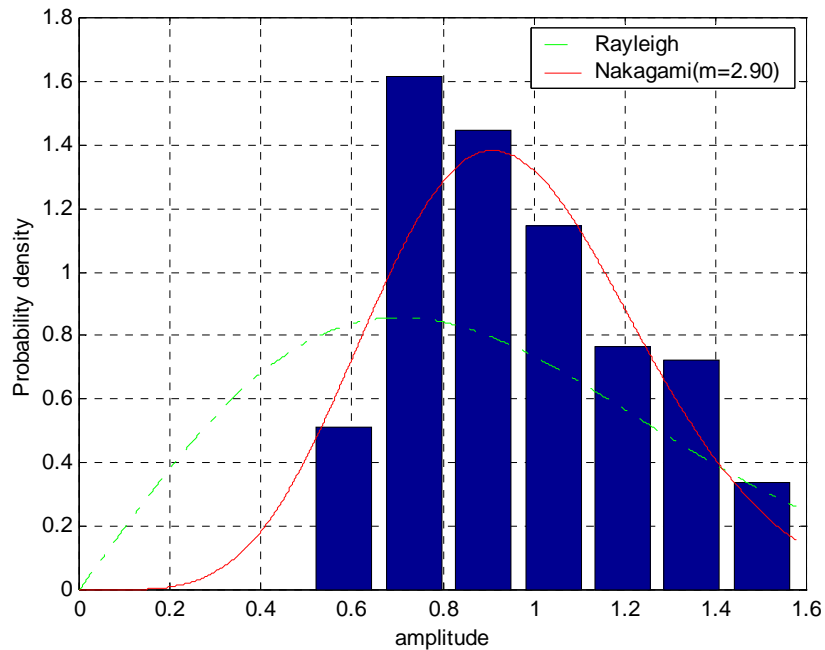


Figure 4-27(b) PDF of measured and fitted signal amplitudes of the 65th bin in Room 303 for NLOS environment. The bandwidth is 2GHz.

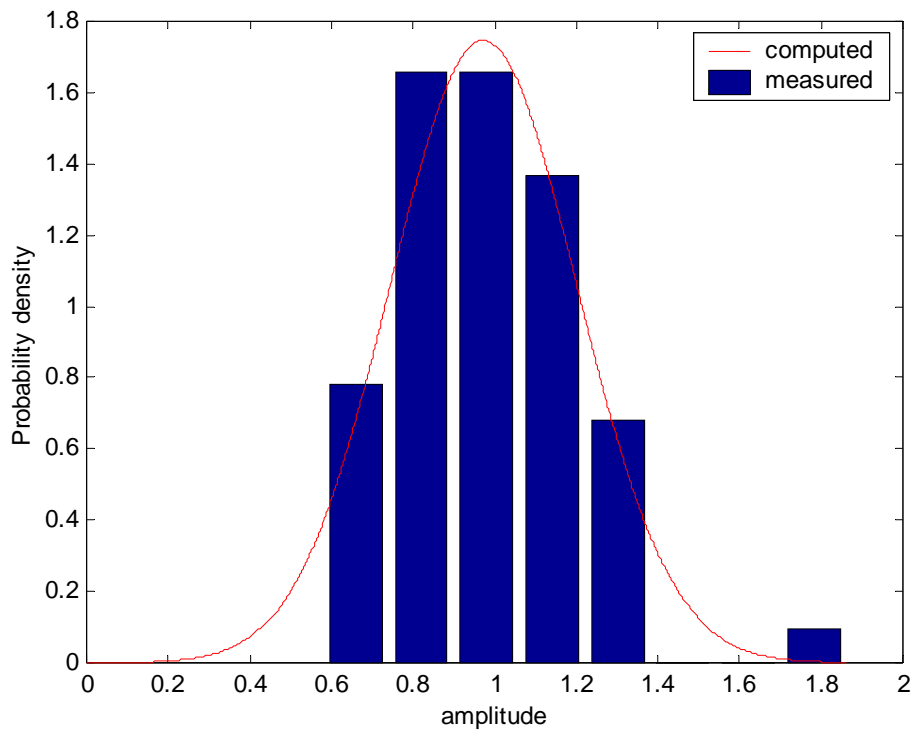


Figure 4-28(a) PDF of measured and computed signal amplitudes of the first bin at point no.2 follows a Rician distribution with $K=8.7$.

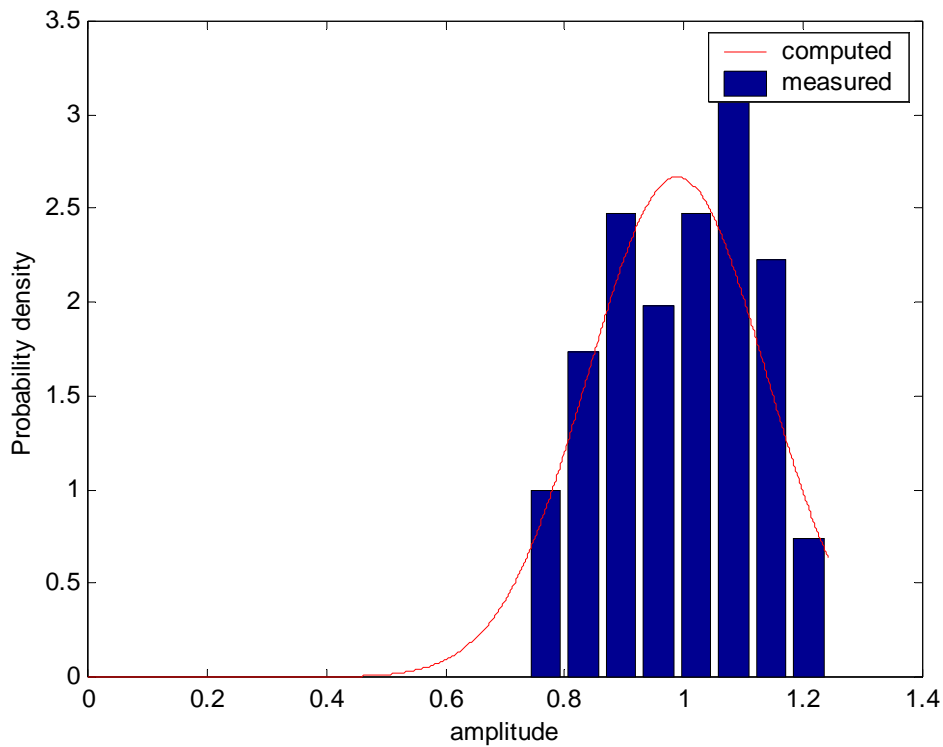


Figure 4-28(b) PDF of measured and calculated signal amplitudes of the first bin at point no.16 follows a Rician distribution with $K=26.4$.

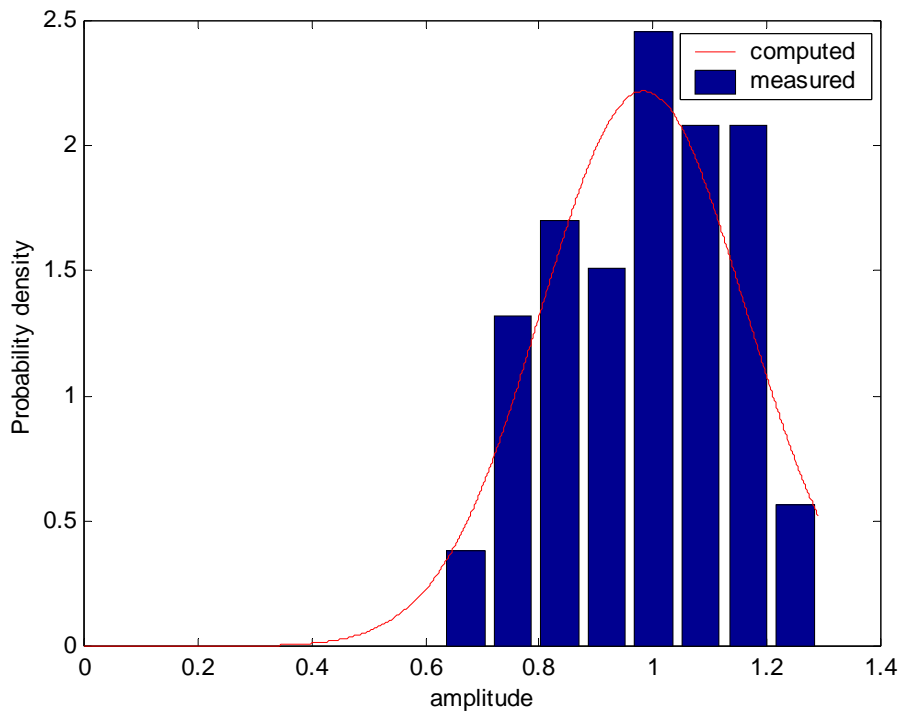


Figure 4-28(c) PDF of measured and computed signal amplitudes of the first bin at point no.21 follows a Rician distribution with $K=16.4$.

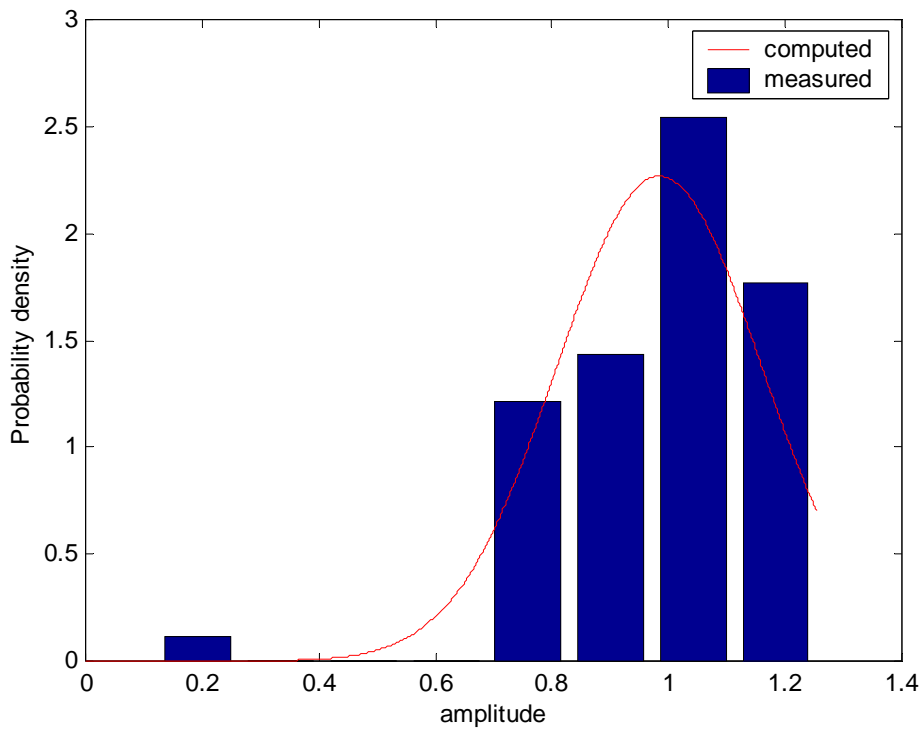


Figure 4-28(d) PDF of measured and computed signal amplitudes of the first bin at point no.41 follows a Rician distribution with $K=17.2$.

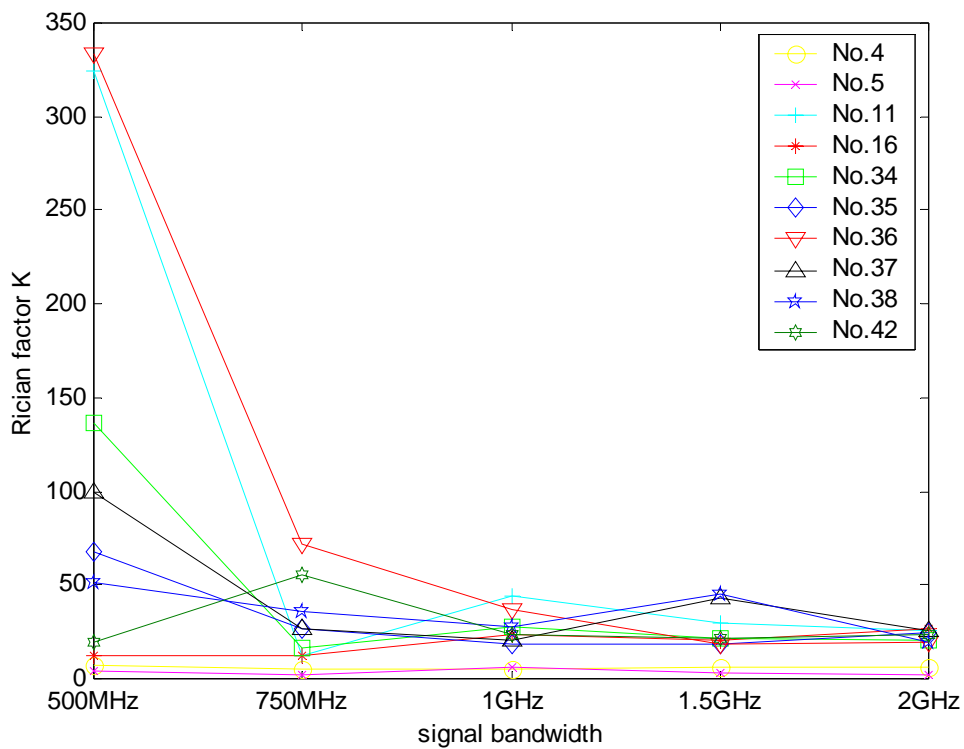


Figure 4-29 Rician factor K versus signal bandwidth at different measurement points of the LOS 0-4m situation.

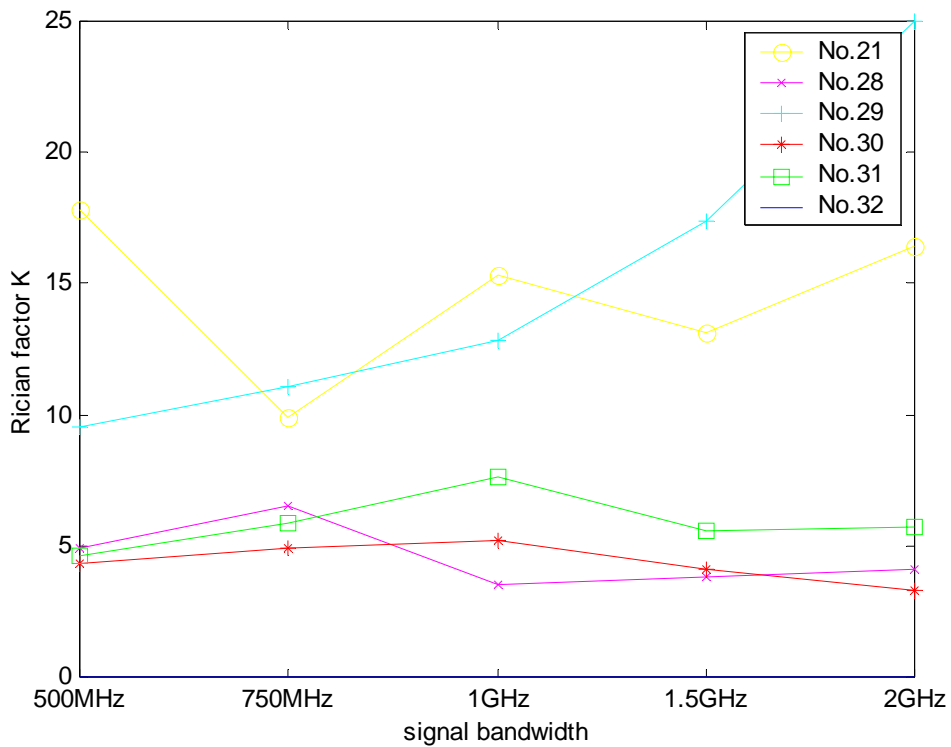


Figure 4-30 Rician factor K versus signal bandwidth at different measurement points of the NLOS 0-4m situation.

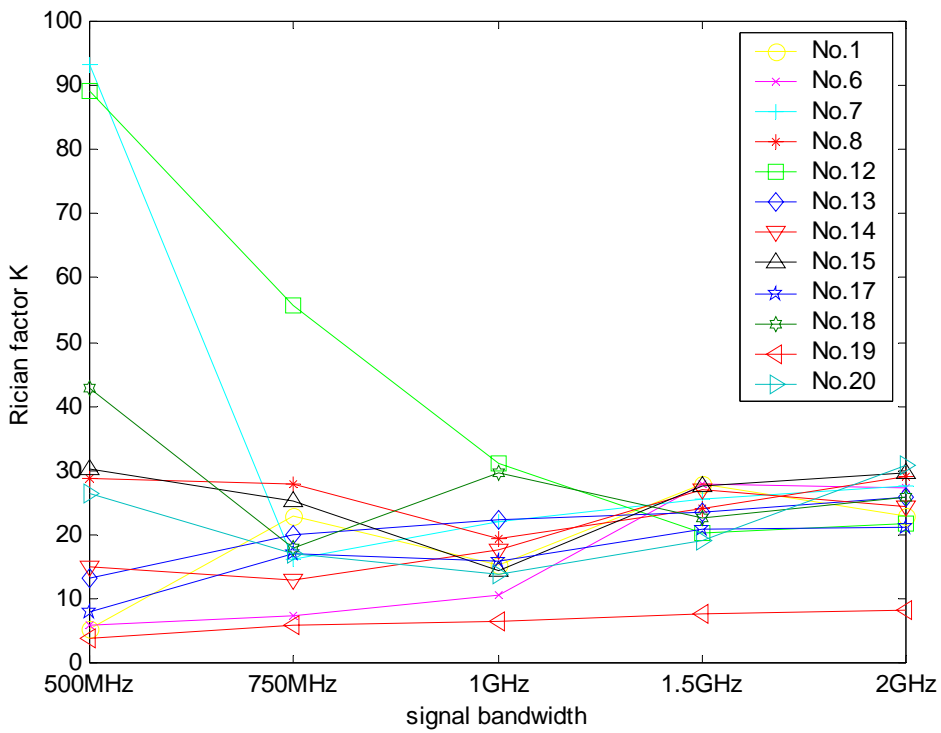


Figure 4-31 Rician factor K versus signal bandwidth at different measurement points of the LOS 4-10m situation.

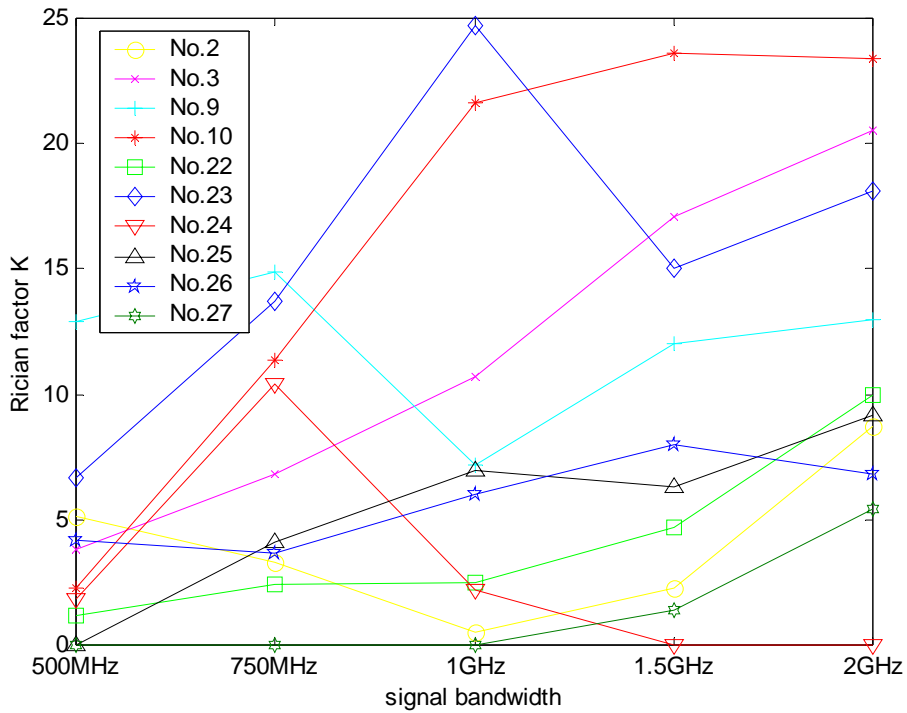


Figure 4-32 Rician factor K versus signal bandwidth at different measurement points of the NLOS 4-20m situation.

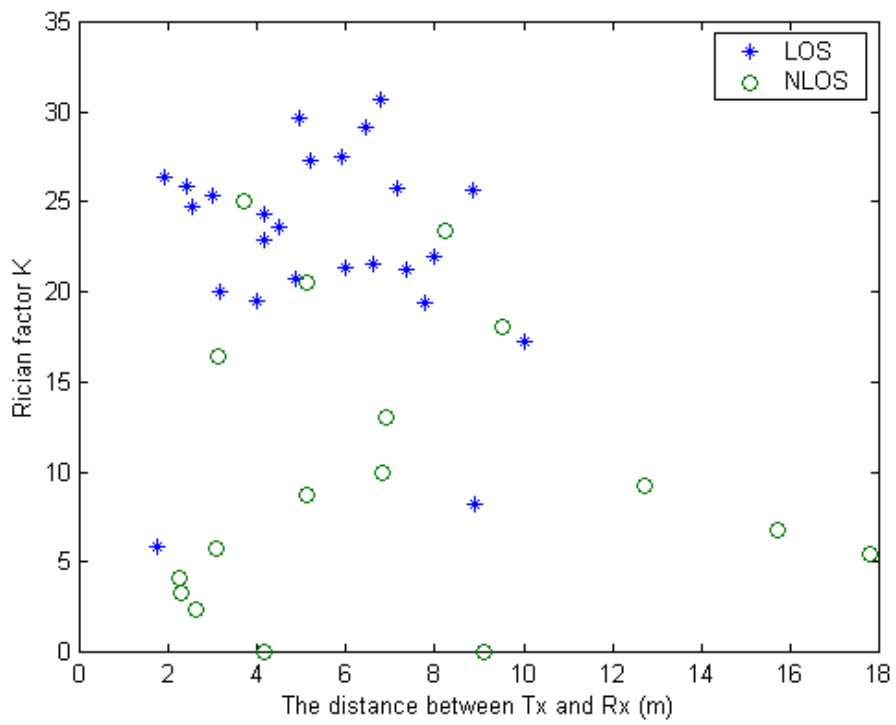


Figure 4-33 The Rician factor versus the distance between Tx and Rx.



Chapter 5

Conclusion

In this article, the effect of signal bandwidth on multipath channel has been studied. The measurement was performed by using Agilent 8719 ET vector network analyzer in the 4th Engineering Building of NCTU. For UWB application, the swept frequency band is from 3GHz to 5GHz (2GHz of frequency span). A method based on STDL model is proposed and validated by measurement results. From the analysis of the measurement results, it is found that the decay constant ε and power ratio r of the PDP and amplitude distribution of small-scale fading are dependent on propagation environment and signal bandwidth.

The power ratio is increased and the decay constant is decreased as the local scatterers move closer to receiver. This is due to the number of scattered multipath is increased of the second bin when the scatterer is closed to receiver.

The power ratio r is increased as the bandwidth decreases. This is due to the proportion of power of the second received bin is increased when bandwidth is decreased. The power of each bin is dependent only on delay time. The decay constant is independent on the bandwidth. It is found that the decay constant and the power delay profile can be well described by a lognormal distribution.

The Rician factor is increased when bandwidth is increased of NLOS condition. Because the numbers of scattered multipath arrived at the first received bin is decreased as the bandwidth increases.

As results, those parameters, including the power ratio r , decay constant ε and Rician factor K are not only dependent on the propagation environment but dependent on the signal bandwidth.

Reference

- [1] D. Greenwood and L. Hanzo, “Characterization of mobile radio channels”, Mobile Radio Communications, R. Steele, Ed., London, U.K., Pentech, pp, 163-185,1992
- [2] IEEE 802.15 WPANs, “SG3a Application Summary”, Document 02149r0P802-15_SG3a, Mar 2002.
- [3] FCC “Revision of Part 15 of the Commission’s Rules Regarding Ultra-Wideband Transmission Systems,” First Report and Order, ET Docket 98-153, FCC 02-48, Apr. 2002.
- [4] A. Saleh and R. Valenzuela, “A Statistical Model for Indoor Multipath Propagation,” IEEE JSAC, vol. SAC-5, no. 2, Feb. 1987, pp. 128–37.
- [5] H. Hashemi, “Impulse Response Modeling of Indoor Radio Propagation Channels,” *IEEE JSAC*, vol. 11, no. 7, Sept. 1993, pp. 967–78.
- [6] Cassioli, M. Z. Win and A. F. Molisch, “The Ultra-Wide Bandwidth Indoor Channel: From Statistical Model to Simulations,” in the *IEEE Journal of Selected Areas in Commun.*, vol. 20, Issue: 6 , Aug. 2002, pp. 1247 –1257.
- [7] Molisch, A.F.; Foerster, J.R.; Pendergrass, M. “Channel models for ultrawideband personal area networks”, IEEE Wireless Communications, Volume: 10 , Issue: 6 , pp.14 – 21, Dec. 2003
- [8] S. Ghassemzadeh, R. Jana, C. Rice, W. Turin, and V. Tarokh, “A Statistical Path Loss Model for In-Home UWB Channels,” IEEE Conference on UWBST pp. 59-64, May 2002.
- [9] T. S. Rappaport, “Wireless Communications Principles and Practice,” Prentice Hall, 1996.
- [10] H. Suzuki, “A Statistical Model for Urban Radio Propagation,” IEEE Transactions on Communications, pp. 673-680, July 1977.

- [11] A. Glazunov, H. Asplund and J. E. Berg, "Statistical analysis of measured short term impulse response functions of 1.88GHz radio channel in Stockholm with corresponding channel model," in IEEE Vehic. Technol. Conference, 1999.
- [12] M. Nakagami, "The m distribution; a general formula of intensity distribution of rapid fading," Statistical Methods in Radio Wave Propagation, W.G. Hoffman, ed., pp.3-36,1960
- [13] U. Charash, "Reception through Nakagami fading multipath channels with random delays," IEEE Trans. Commun., Vol. 27, pp. 657-670, April 1979.
- [14] J. Foerster and Q. Li, "UWB Channel Modeling Contribution from Intel," IEEE P802.15-02/279-SG3a.
- [15] J-M Cramer, R. Scholtz, M. Win, "Evaluation of an Indoor Ultra-Wideband Propagation Channel," IEEE P802.15-02/286-SG3a and IEEE P802.15-02/325-SG3a.

